Engineering a Microporous Hydrogel Scaffold to Improve Human Ovarian Tissue Transplantation Outcomes

by

Despina Ifigenia Pavlidis

A dissertation submitted in partial fulfillment
of the requirements for the degree of
Doctor of Philosophy
(Biomedical Engineering)
in the University of Michigan
2026

Doctoral Committee:

Professor Ariella Shikanov, Chair
Associate Professor Brendon M. Baker
Assistant Professor Sasha Cai Lesher-Pérez
Professor Vasantha Padmanabhan
Professor Lonnie D. Shea

Despina I. Pavlidis

dpavlidi@umich.edu

ORCID iD: 0000-0002-2156-3561

© Despina I. Pavlidis 2026

Dedication

To my parents, Vasso and Dimitris Pavlidis, my first mentors and forever supporters.

Acknowledgements

This dissertation would not have been possible without the guidance and support of countless individuals. I would like to start by thanking my advisor, Dr. Ariella Shikanov, for the privilege of conducting research at the forefront of reproductive tissue engineering. You encouraged me to push the boundaries of our field and gave me the opportunity to grow as a mentor to the next generation of scientists. I would also like to thank my committee members, Dr. Brendon Baker, Dr. Sasha Cai Lesher-Pérez, Dr. Vasantha Padmanabhan, and Dr. Lonnie Shea, whose expertise and insight shaped the trajectory of my research and strengthened the work presented here.

To my Shikanov Lab friends, past and present, I am so grateful for the laughter and support you brought into every season of my PhD. There is no one I'd rather do an ovary harvest with in the wee hours of the night. You showed up for the long days and still found the energy to dance the night away when the work was done. Thank you for also being the willing recipients of my constant stress baking! I am selfishly grateful that you indulged me as unofficial taste-testers; you gave me the perfect excuse to keep up a hobby I love and a sweet way to celebrate all of you.

I'd also like to acknowledge the Shikanov Lab as a whole. I started my PhD in Fall 2020, and some of my earliest lab memories include the nighttime shift, learning lab skills from six feet away, and using Zoom screenshots as our lab photos. Even in those "unprecedented times," you welcomed me into your little bubble with open arms: social hour in the parking lot, Songbird

coffee from the backs of open car trunks, and small moments of connection that made the first year feel a little lighter.

I was fortunate to work with two extremely talented and hardworking undergraduate researchers, Chloe and Maria. Your curiosity and dedication were invaluable to this dissertation and your fun, positive energy made the lab a brighter place.

To the friends who have been in my life long before I embarked on this PhD, thank you for your steady support and encouragement. You kept me grounded and cheered me on through every milestone, big or small.

To my immediate and extended family, thank you for the love, encouragement, and support that sustained me throughout this journey. I am especially grateful to my parents for shaping who I am and for believing in me through it all. Μπαμπά, thank you for your lived wisdom, steady perspective, and for always reminding me of what matters when the details felt all-consuming. Μαμά, thank you for being unwaveringly on my side, for matching my energy in every moment, and for instilling in me the fierce confidence that made this work possible. To my brothers, Spyros and Georges, thank you for your camaraderie and for always making me feel understood, supported, and a little less alone. And to Stef (the older sister I always wished I had), thank you for understanding both my science and my feelings, and for reassuring me through both. I also hold close the family members who are no longer here to celebrate this milestone in person, but whose love, example, and memory remain woven into this accomplishment.

To my partner, John, thank you for supporting me so steadfastly through every high and low, for keeping me fed from near and far, and for always making sure I ended each day with a smile on my face. And to our feline voids, Ares and Lupin, thank you for being the very best companions I could ask for throughout my PhD.

Table of Contents

Dedication ii

Acknowledgements iii

List of Tables vii

List of Figures ix

List of Appendices xiv

Abstract xv

Chapter 1 Introduction 1

1.1 Reproductive and Endocrine Consequences of Cancer Treatment 1

1.2 Ovarian Tissue Cryopreservation and Transplantation (OTCT) 2

1.3 Central Limitation of OTCT: Avascular Transplantation 3

1.4 Biomaterials for OTCT 5

1.5 Microporous Annealed Particle (MAP) Hydrogels 6

1.6 Gaps in Characterization of Human Ovarian Tissue 7

1.7 Dissertation Overview 8

Chapter 2 Three-Dimensional Characterization of Follicular and Vascular Architecture in Human Ovarian Tissue 10

2.1 Introduction 10

2.2 Materials and Methods 12

2.3 Results 21

2.4 Discussion 31

Chapter 3 Engineering the Host-Graft Interface Stabilizes Vascular Integration and Improves Endocrine Function of Transplanted Human Ovarian Tissue 35

3.1 Introduction 35
3.2 Materials and Methods 37
3.3 Results 56
3.4 Discussion 72
Chapter 4 Conclusions and Future Directions 77
4.1 Summary of Findings: Three-Dimensional Characterization of Human Ovarian Tissue. 78
4.2 Summary of Findings: Engineering the Host-Graft Interface 79
4.3 Future Directions 80
4.4 Toward Improving OTCT Outcomes 87
Appendices 89
Bibliography 123

List of Tables

Table 2.1 Donor Information 13

Table 2.2 CUBIC Clearing and Staining Timelines 17

Table 2.3 Linear Expansion Imaging Timeline 18

Table 2.4 Acquisition Parameters and Dataset Characteristics for Cleared Medulla 30

Table 3.1 Parameters for Hydrogel Mesh Size Calculations 42

Table 3.2 Molecules Used for Hydrogel Diffusion Assay 44

Table 3.3 CUBIC Clearing and Staining Protocol Timeline 52

Table 3.4 Q-VAT Input Parameters 54

Appendix Table A.1 Donor Tissue-Specific Follicle Density. 90

Appendix Table C.1 Gelation Studies Modulating HEPES Buffer pH for both PEG and YKNS Suspensions 100

Appendix Table C.2 Gelation Studying Modulating HEPES Buffer pH for PEG Suspension and TCEP Concentration for YKNS Suspension 101

Appendix Table C.3 Gelation Studies Modulating RGD Functionalization Concentration 102

Appendix Table C.4 Gelation Studies for In Vivo Bulk Hydrogel Control 103

Appendix Table C.5 Swelling Ratios of PEG-VS Hydrogels as a Function of HEPES Buffer pH 105

Appendix Table C.6 Swelling Ratios of PEG-VS Hydrogels as a Function of HEPES Buffer pH and TCEP Concentration 105

Appendix Table C.7 Swelling Ratios of PEG-MAL Hydrogels as a Function of HEPS Buffer pH 106

Appendix Table C.8 Swelling Ratios of PEG-MAL Hydrogels as a Function of RGD Functionalization Concentration 106

Appendix Table C.9 Ultraviolet (UV)-Mediated Annealing Strategies 107

Appendix Table C.10 Peptide-Mediated Annealing Strategies 109

Appendix Table C.11 Thrombin-. Fibrinogen-. and Factor XIII-Mediated Annealing Strategies 110

List of Figures

Figure 2.1 Adapted CUBIC Protocol Characterization for Human Ovarian Tissue. (A) Overview of the three major CUBIC protocol phases. **(B)** Cortex and medulla processed with the adapted CUBIC protocol become optically transparent, enabling visualizing of the millimeter paper grid below. **(C)** Cleared cortex and medulla undergo similar expansion due to CUBIC clearing. Each data point represents the terminal linear expansion for a tissue piece (n = 4 tissue pieces per condition), error bars are mean ± standard deviation. Data analyzed by Mann-Whitney test, $p < 0.05$, ns = not significant. **(D)** Representative confocal images depicting an X-Y plane and Z imaging depth for control and cleared cortex and medulla. **(E)** CUBIC clearing increases imaging depth for both cortex and medulla across different tissue sources. Each data point represents the imaging depth for one tissue piece within the respective donor (n = 3 tissue pieces per donor), error bars are mean ± standard deviation. Data analyzed by two-way ANOVA with Šidák's multiple comparisons test, $p < 0.05$, significant difference indicated as *$p \leq 0.05$, **$p \leq 0.01$, ***$p \leq 0.001$, ****$p \leq 0.0001$..... 23

Figure 2.2 Follicle Detection and Quantification in Cleared Human Ovarian Cortex. (A) Representative confocal z-slices of follicles in cryopreserved cleared tissue depicting ZP3 and DAPI channels, and the merged images. **(B)** Representative histological H&E images of follicles from fresh donor-matched tissue. **(C)** Comparison of follicle densities computed from CUBIC-cleared tissue and histological H&E images for each donor. Each data point represents the follicle density from a confocal z-stack substack (CUBIC) or a histological section (H&E), error bars are mean ± standard deviation. Data analyzed by Mann-Whitney test, $p < 0.05$, ns = not significant..... 25

Figure 2.3 Vasculature Mapping in Cleared Human Ovarian Cortex. (A) Representative three-dimensional rendering of cortex vasculature from CUBIC-cleared and light sheet-imaged tissue with **(i)** showing vasculature tracing overlayed with the UEA-1 signal within an ROI and **(ii)** depicting the color-coded mean vessel diameters of the traced vasculature within the ROI. **(B)** Histograms of mean vessel diameter measurements for each donor. Within each histogram, data from three individual tissue pieces are shown and color-coded by tissue piece. For each tissue piece, blood vessels were automatically detected and segmented, and a mean diameter was calculated for every traced vessel. **(C)** Donor-level summary of mean vessel diameter. Each bar represents one donor and each data point corresponds to the mean of the per-vessel mean diameters for respective tissue pieces. Error bars are donor-level mean ± standard deviation. **(D)** Density of total vessel branch points detected within the analyzed ROI tissue volumes. **(E)** Density of total vessel length detected within the analyzed ROI tissue volumes. **(F)** Total vessel volume per tissue volume within analyzed ROI tissue volumes. Each data point represents the measurement for one tissue piece within the respective donor, error bars are mean ± standard deviation. Data analyzed by Kruskal-Wallis test with Dunn's multiple comparisons test, $p < 0.05$, ns = not significant..... 27

Figure 2.4 Location of Vasculature in Relation to Follicles. (A) Two-dimensional (2D) image of vasculature (white arrow) wrapping around a multilayer follicle. Vasculature traces from the previous vasculature analysis were overlaid with the follicle surface to better visualize the three-dimensional (3D) follicle-vessel spatial relationship. **(B)** Regions of cleared cortex with increasing proximity **(i–iv)** of vasculature (white arrows) to follicles. 29

Figure 2.5 Comparison of Confocal and Light Sheet Imaging Modalities. (A) Sequential portions of a confocal z-stack depicting imaging depth capability in reference to an antral follicle structure. **(B)** Sequential portions of a light sheet z-stack of the same tissue piece depicting imaging depth capability in reference to the antral follicle structure. **(C)** Confocal z-slices depicting small follicles and surrounding stroma cells captured in the large medulla piece image. Light sheet z-slice depicting a small follicle and surrounding stroma cells adjacent to the follicle antrum. 31

Figure 3.1 Revascularization of Non-Encapsulated Human Ovarian Tissue Grafts. (A) Human ovarian donor tissue processing into cortex squares prior to cryopreservation. Upon thawing, ovarian cortex squares were cut into strips and implanted into the parametrial fat pads of immune deficient, ovariectomized mice. Arrows mark the human ovarian tissue. **(B)** Representative maximum intensity projection images show post-implantation mouse (CD31, green) and human (UEA-1, red) vasculature dynamics in human ovarian tissue strips over the course of 6 weeks. Dashed white lines delineate the border of the implanted human tissue within the surrounding mouse fat pad. Asterisks indicate chimeric ($UEA\text{-}1^{+}/CD31^{+}$) vasculature. **(C)** Percent area of implanted human ovarian tissue strip that stained positively for mouse vasculature. **(D)** Mouse total vessel length per tissue strip area. **(E)** Mouse mean branch length within tissue strip. **(F)** Percent area of implanted human ovarian tissue strip that stained positively for human vasculature. Data points represent individual grafts from distinct mouse hosts (n = 3 per time point). Data analyzed by one-way ANOVA with Tukey's multiple comparisons test, $p < 0.05$, different letters indicate statistical significance. 58

Figure 3.2 MAP Hydrogel Fabrication and Characterization. (A) Microfluidic fabrication of PEG microgels and diameter distribution of crosslinked microgels. **(B)** Microgels were annealed through photopolymerization of remaining maleimide groups, producing an assembled MAP hydrogel shown in the representative 3D rendering. **(C)** MAP hydrogel pore area distribution was measured using confocal images of assembled MAP hydrogels (n = 5 MAP hydrogels). Pore diameter distribution was estimated by treating pore areas as corresponding to areas of circles. **(D)** In vitro cumulative diffusion of 4 kDa and 40 kDa FITC-DEX and 66 kDa Alexa Fluor 488-conjugated BSA through bulk (n = 3) and MAP (n = 3) hydrogels after 6 hours and 96 hours, demonstrating greater molecular transport through MAP hydrogels. Each data point represents one hydrogel. Data analyzed by two-way ANOVA with Šidák's multiple comparisons test, $p < 0.05$, significant difference indicated as ****$p \leq 0.0001$. **(E)** Encapsulation of human ovarian cortex cubes within MAP hydrogels and implantation of OvaMAP into the mouse parametrial fat pad. Arrows mark the ovarian tissue and OvaMAP. ... 61

Figure 3.3 Revascularization of MAP Hydrogel-Encapsulated Human Ovarian Tissue Grafts. (A) Representative maximum intensity projection images show post-implantation mouse (CD31, green) and human (UEA-1, red) vasculature dynamics in human ovarian tissue cubes encapsulated in MAP hydrogels (OvaMAPs) over the course of 6 weeks. Dashed white

lines delineate OvaMAP border within the surrounding mouse fat pad. Insets in the bottom left display the entire OvaMAP graft. **(B)** Percent area of OvaMAP human ovarian tissue cubes that stained positively for mouse vasculature. **(C)** Mouse total vessel length per OvaMAP total tissue cube area. **(D)** Mouse mean branch length within OvaMAP tissue cubes. **(E)** Percent area of OvaMAP human ovarian tissue cubes that stained positively for human vasculature. **(F)** Representative maximum intensity projection images show post-implantation mouse (CD31, green) and human (UEA-1, red) vasculature dynamics in human ovarian tissue cubes encapsulated in bulk hydrogels over the course of 6 weeks. Dashed white lines delineate the bulk hydrogel border. Note the lack of mouse $CD31^+$ staining and the lack of mouse fat pad integration, suggesting the bulk hydrogel did not support mouse vascular infiltration at any time point. Data points represent individual grafts from distinct mouse hosts (n = 3 per time point). Data analyzed by one-way ANOVA with Tukey's multiple comparisons test, $p < 0.05$, different letters indicate statistical significance. 63

Figure 3.4 MAP Hydrogel Sustains Long-Term Human Ovarian Graft Revascularization. **(A)** Representative z-slice images demonstrate progressive cellular infiltration into OvaMAPs at 3 days to 6 weeks post-transplantation. Early $DAPI^+$ cell migration into MAP hydrogel pores was observed by 3 days, followed by infiltration of mouse $CD31^+$ endothelial cells by 3–6 weeks which localized to the encapsulated ovarian tissue. Dashed white lines delineate OvaMAP border within the surrounding mouse fat pad. **(B)** Representative z-slice images of non-encapsulated tissue strips depicting mouse vasculature infiltration into tissue grafts over the course of 6 weeks. Dashed white lines delineate the border of the implanted human tissue within the surrounding mouse fat pad. Asterisks indicate chimeric ($UEA\text{-}1^+/CD31^+$) vasculature. **(C)** Comparison of percent area of implanted human ovarian tissue that stained positively for mouse vasculature. **(D)** Comparison of mouse total vessel length per tissue strip area or per total tissue cube area (OvaMAPs). **(E)** Comparison of mouse mean branch length within tissue strip or tissue cubes (OvaMAPs). Data points represent individual grafts from distinct mouse hosts (n = 3 per time point, per condition). Data analyzed by two-way ANOVA with Šidák's multiple comparisons test, $p < 0.05$, significant difference indicated as $*p \leq 0.05$, $**p \leq 0.01$, $***p \leq 0.001$. 66

Figure 3.5 Perfused, Functional Host Revascularization of OvaMAPs. (A) Infiltrating mouse host vasculature (CD31, green) in OvaMAPs 3 and 6 weeks post-transplantation contains mouse red blood cells (TER-119, orange), confirming functional perfusion. **(B)** Perfused vasculature was evident both within MAP hydrogel pores **(a)** and within the encapsulated tissue cubes **(b)** at 3 and 6 weeks post-transplantation. Dashed white lines delineate OvaMAP border within the surrounding mouse fat pad. Magenta dashed lines delineate regions containing perfused vasculature within hydrogel pores while green dashed lines delineate regions containing perfused vasculature within encapsulated ovarian tissue cubes. 68

Figure 3.6 Long-term Graft Revascularization and Endocrine Function Restoration. (A) Representative maximum intensity projection images show post-implantation mouse (CD31, green) and human (UEA-1, red) vasculature dynamics within grafts 20 weeks post-transplantation. The non-encapsulated tissue strip image comprises 6 z-slices. The OvaMAP and bulk hydrogel graft comprise 101 z-slices. Dashed white lines delineate graft borders within the surrounding mouse fat pad. Asterisks denote human $UEA\text{-}1^+$ vasculature in the

adjacent host mouse tissue. At 20 weeks, serum estradiol **(B)**, follicle-stimulating hormone (FSH) **(C)**, and progesterone **(D)** levels were quantified in host mice (n = 4 per condition) implanted with non-encapsulated tissue strips, OvaMAPs, or bulk hydrogel-encapsulated tissue cubes. The dashed line marks mean progesterone levels in ovariectomized NSG mice from a previously published study[83]. Each data point represents one host mouse. Data analyzed by Kruskal-Wallis test with Dunn's multiple comparisons test, $p < 0.05$, significant differences indicated as *p≤0.05, **p≤0.01, ***p≤0.001. 71

Appendix Figure A.1 Intra-Donor Follicle Density Heterogeneity. Follicle densities across each of the three analyzed tissue pieces for Donors A–D. Each data point represents the follicle density within one z-stack substack (9-10 substacks per tissue piece), error bars are mean ± standard deviation per tissue piece. Data analyzed by Kruskal-Wallis test with Dunn's multiple comparisons test, $p < 0.05$, significant differences indicated as *p≤0.05, **p≤0.01, ***p≤0.001. 90

Appendix Figure B.1 Characterization of MAP Hydrogel Porosity, Mesh Size, and Diffusion. (A) Workflow illustrating porosity quantification from confocal images using FIJI (ImageJ). **(B)** Nanoporous bulk hydrogel mesh sizes for MAP hydrogel and bulk hydrogel formulations (n = 6 per condition) were estimated from swelling ratios. **(C)** Illustration of experimental methods used to determine the diffusion of molecules through bulk and MAP hydrogels. Short- and long-term diffusion of 4 kDa FITC-DEX (**D)**, 40 kDa FITC-DEX **(E)**, and 66 kDa Alexa Fluor 488-BSA **(F)** through MAP (pink) and bulk (purple hydrogels) (n = 3 per hydrogel type). Short-term measurements were conducted hourly for 6 hours while long-term measurements were conducted every 24 hours over 96 hours. 91

Appendix Figure B.2 Hydrogel Storage Moduli. Storage modulus of PEG-VS bulk hydrogel, PEG-MAL MAP hydrogel, and bulk hydrogel fabricated using the PEG-MAL microgel formulation. A minimum of n = 6 hydrogels were tested per condition, error bars are mean ± standard deviation per group. Data analyzed by one-way ANOVA with Tukey's multiple comparisons test, $p < 0.05$, significant differences indicated as ****p ≤ 0.0001. 92

Appendix Figure B.3 Human Donor Ovarian Cortex Characterization. (A) Representative hematoxylin and eosin (H&E) staining of fresh fixed ovarian cortex from donors A and B, with corresponding estimated follicle densities **(B)**. Error bars are mean ± standard deviation per group. 93

Appendix Figure B.4 Human Vasculature Regression within Bulk Hydrogel-Encapsulated Tissue. Percent area of implanted, bulk hydrogel-encapsulated human ovarian tissue cubes that stained positively for human vasculature. Data represent individual grafts from distinct mouse hosts (n = 3 per time point), error bars are mean ± standard deviation per group. Data analyzed by one-way ANOVA with Tukey's multiple comparisons test, $p < 0.05$, different letters indicate statistical significance. 94

Appendix Figure C.1. Visible disulfide bond formation (white arrow) within syringe containing YKNS solution being delivered to microfluidic device. 96

Appendix Figure D.1. Mixing **(A)** and droplet generation **(B)** microfluidic devices. Scale bars = 200 µm. 111

Appendix Figure D.2. Integrated mixing and droplet generation microfluidic device. 112

Appendix Figure E.1 Brightfield images of human ovarian tissue encapsulated in fibrin-only gels or microgel-fibrin composites and cultured under static **(A)** or rocking **(B)** conditions for 3 and 7 days. Cellular outgrowth from tissue fragments is visible as early as Day 3 (white arrows) in both scaffold conditions. Fibrin degradation (asterisks) is more apparent in rocking cultures. Scale bars = 500 µm for all images except Day 3 microgel-fibrin rocking condition (200 µm). OT: ovarian tissue. 118

Appendix Figure E.2. Confocal images of human ovarian tissue encapsulated in fibrin-only gels and cultured under static or rocking conditions for 3 and 7 days. Samples were stained for F-actin and CD31 to assess overall and endothelial cell outgrowth. Due to limitations in staining consistency during these pilot studies, the low magnification images display F-actin and DAPI only. CD31 staining is shown for the inset in the Day 7 static condition. Dashed white lines delineate the edge of the ovarian tissue. Scale bars = 100 µm. 119

Appendix Figure E.3. Confocal images of human ovarian tissue encapsulated in microgel-fibrin composites and cultured under static or rocking conditions for 3 and 7 days. Samples were stained for F-actin and CD31. $CD31^+$ outgrowth wrapping around a microgel (arrow) was observed in the Day 3 static condition. Dashed white lines delineate the edge of the ovarian tissue. Scale bars = 100 µm 120

Appendix Figure E.4. Brightfield images of human ovarian tissue encapsulated heparin-functionalized microgel-fibrin composites and cultured under static or rocking conditions for 3 and 7 days. Cellular outgrowth from tissue fragments is visible at day 3 (white arrows) in both static and rocking conditions. Scale bars = 500 um. OT: ovarian tissue. 121

Appendix Figure E.5. Confocal images of human ovarian tissue encapsulated in heparin-functionalized microgel-fibrin composites and cultured under static or rocking conditions for 3 and 7 days. Samples were stained for F-actin and CD31. Static cultures demonstrate more consistent $CD31^+$ outgrowth compared to rocking conditions. High-magnification images for the Day 3 and Day 7 static conditions include the transmitted light channel (light gray) to better visualize microgel structure and $CD31^+$ staining (white arrows). Dashed white lines delineate the edge of the ovarian tissue. Scale bars = 100 µm 122

List of Appendices

Appendix A: Chapter 2 Supplemental Materials 90

Appendix B: Chapter 3 Supplemental Materials 91

Appendix C: MAP Hydrogel Formulation Development 95

C.1 Delaying Hydrogel Gelation 96

C.2 Development of Annealing Strategies for PEG-VS 97

C.3 Transition to PEG-MAL 98

C.4 Crosslinking Requirements for In Vivo Bulk Controls 98

Appendix D: Microfluidic Device Screening 111

D.1 Mixing and Droplet Generation Microfluidic Devices 111

D.2 Integrated Mixing and Droplet Generation Microfluidic Device 112

D.3 Step Emulsification Microfluidic Device 113

Appendix E: Pilot Human Ovarian Tissue Cultures 114

E.1 Methods and Materials Summary 114

E.2 Fibrin and Microgel-Fibrin Culture: Brightfield Observations 115

E.3 Fibrin Culture: Confocal Observations 115

E.4 Microgel-Fibrin Culture: Confocal Observations 115

E.5 Heparin-Functionalized Microgels: Brightfield Observations 116

E.6 Heparin-Functionalized Microgels: Confocal Observations 116

E.7 Overall Interpretation and Limitations 116

Abstract

Primary ovarian insufficiency (POI) is a prevalent consequence of gonadotoxic cancer treatments which results in premature infertility and loss of ovarian endocrine function. Currently, ovarian tissue cryopreservation and transplantation (OTCT) is the only clinical strategy capable of restoring both fertility and physiological ovarian endocrine function in cancer survivors with POI. Although most recipients regain endocrine activity, graft function ranging from months to years and low live birth rates reveal the variable and unpredictable nature of OTCT outcomes. Two factors contribute to this variability: (1) the innate heterogeneity of human ovarian tissue and (2) the avascular nature of the transplantation procedure which subjects grafts to ischemia and induces significant tissue injury and follicle loss. This dissertation addresses both factors by establishing quantitative methods to characterize human ovarian tissue microarchitecture and engineering the host-graft interface to support revascularization following avascular transplantation.

Human ovarian tissue is structurally heterogeneous, with follicles and vasculature organized three-dimensionally across spatial scales not captured by thin histological sections. To enable volumetric assessment of this architecture, a tissue clearing protocol was adapted and validated for human ovarian tissue cryopreserved according to clinical fertility preservation protocols. Follicle density measurements from cleared tissue were comparable to two-dimensional histological measurements, validating the quantitative accuracy of the clearing protocol while enabling three-dimensional assessment of follicle location across intact tissue

volumes. Light sheet imaging facilitated quantitative mapping of vascular morphometrics across cleared tissue, including vessel diameter, branch point density, and length density. By preserving spatial relationships within intact tissue, this workflow permits assessment of baseline tissue microarchitecture and quantification of vascular remodeling after transplantation. Structural tissue heterogeneity therefore becomes a measurable parameter rather than an uncharacterized source of variability, establishing an analytical foundation for interpreting graft performance in OTCT.

Next, a poly(ethylene glycol) microporous annealed particle (MAP) hydrogel was developed as a transplantation scaffold for human ovarian tissue to modulate the host-graft interface following avascular transplantation. Human ovarian tissue encapsulated in MAP hydrogels (OvaMAPs) was transplanted into an immunodeficient mouse model of POI and analyzed at early (3 days, 1 week) and late (3, 6, 20 weeks) time points. Using the developed tissue clearing protocol, we found that non-encapsulated grafts exhibited a transient surge in host vascular infiltration at 1 week that regressed by 3-6 weeks, resulting in sparse and disorganized vessels largely confined to the graft periphery. In contrast, OvaMAPs demonstrated progressive host vessel ingrowth between 1-3 weeks that remained stable through 20 weeks, with perfused vessels extending through the microporous scaffold network and into the encapsulated ovarian tissue. While both groups restored circulating estradiol, progesterone, and suppression of follicle-stimulating hormone by 20 weeks, OvaMAP recipients showed reduced variability in estradiol levels compared to non-encapsulated graft recipients. These findings were achieved without exogenous growth factor or support cell delivery, indicating that controlled architectural modulation of the host-graft interface alone can support graft vascular integration and lead to more consistent graft performance.

Overall, this dissertation presents a framework in which advanced volumetric imaging and intentional control of transplantation microenvironment architecture are leveraged to interrogate and improve OTCT outcomes. By combining three-dimensional tissue characterization tools with a synthetic MAP hydrogel – applied here for the first time to whole tissue transplantation – this work establishes structural control of the host-graft interface as a strategy for improving the reliability of OTCT.

Chapter 1 Introduction

1.1 Reproductive and Endocrine Consequences of Cancer Treatment

Advancements in cancer screening and treatment have dramatically improved patient survival rates over the past fifty years[1]. This success, however, has been paired with a growing need to address the long-term, off-target effects of cancer treatments that persist long after remission and impact survivors' quality of life[2]. Many standard cancer treatments, including radiotherapy and chemotherapy, are highly gonadotoxic. For patients with ovaries, these treatments severely damage ovarian follicles, the source of fertility and ovarian endocrine function, leading to premature depletion of the finite and non-renewable ovarian reserve[3,4]. As a result, approximately 68% of patients with ovaries treated with gonadotoxic cancer treatments develop primary ovarian insufficiency (POI), a condition defined as the loss of ovarian activity before the age of 40[5,6]. The consequences of POI include not only premature infertility but also the early onset of menopause due to loss of ovarian endocrine function[4,6]. Consequently, POI is associated with increased risks of cardiovascular disease, osteoporosis, cognitive dysfunction, mood disorders, and in young patients, arrested puberty.

Clinical management of POI focuses on two distinct needs: (1) establishing adequate gonadal hormone levels through hormone replacement therapy (HRT), and (2) preserving fertility through assistive reproductive technologies (ART) such as oocyte or embryo cryopreservation. HRT, however, fails to replicate the dynamic, cyclical hormone levels generated from native feedback networks between organs and tissues of the endocrine system[7].

Furthermore, oocyte and embryo cryopreservation require hormone stimulation and time, rendering them unsuitable for pre- and peripubertal patients and patients who cannot delay cancer treatment[8,9]. For these patient populations, ovarian tissue cryopreservation and transplantation (OTCT) is the only option that offers the possibility of restoring both fertility and physiological ovarian endocrine function[10].

1.2 Ovarian Tissue Cryopreservation and Transplantation (OTCT)

OTCT involves the cryopreservation of ovarian tissue prior to cancer treatment and subsequent transplantation of the tissue following patient remission. Typically, only the ovarian cortex is cryopreserved as it houses the primordial follicles (PFs) that constitute the ovarian reserve. Unlike oocyte or embryo cryopreservation, ovarian tissue cryopreservation does not require hormonal stimulation or reproductive maturity and can therefore be promptly performed without delaying cancer treatments[8]. Since the first report of OTCT in 2000[11], this procedure has demonstrated promising outcomes with at least 189 live births noted[12] and approximately 89% of patients having experienced restored ovarian endocrine function as soon as 4–5 months after transplantation[13]. Despite these successes, OTCT outcomes remain limited and variable. The live birth rate stands at a mere 28% (95% confidence interval: 24%–34%) and graft function longevity varies between 0.7–5 years[12]. It should be noted that these metrics likely overestimate clinical success as many studies do not account for the number of transplantations performed per patient, use inconsistent definitions of continued ovarian function, and lack systematic follow-up with patients[12,14].

Several factors contribute to the variability in OTCT outcomes. First, follicle distribution within human ovarian tissue is highly heterogeneous, varying between patients and even within the same ovary. Reliable, non-destructive methods to evaluate the number and spatial

distribution of follicles in the tissue at the time of OTCT are not available, restricting the ability to predict graft lifespan or reproductive potential[15]. Second, significant ovarian tissue damage and follicle loss occur shortly after transplantation due to ischemic and reperfusion injuries[8]. The combination of these two factors results in shortened and variable graft function which poses a considerable clinical challenge, especially for patients with minimal amounts of cryopreserved tissue.

1.3 Central Limitation of OTCT: Avascular Transplantation

The long-term success of OTCT depends, in part, on the number of PFs present at the time of cryopreservation and the number of PFs that survive the transplantation procedure[13]. Studies using sheep and human ovarian tissue transplanted into immunodeficient mice have found that 50%–90% of PFs are lost shortly after transplantation[16,17]. Importantly, it is thought that this follicle loss arises primarily due to the transplantation process, rather than from cryopreservation and thawing, and occurs before restoration of blood flow to the graft[16].

Unlike whole-organ transplants, ovarian cortical tissue lacks large blood vessels amenable to surgical vascular anastomosis[8]. Consequently, restoration of blood flow depends solely on graft revascularization through angiogenesis and anastomosis with the host vasculature. Studies involving xenotransplantation of human ovarian tissue into immunodeficient mice have shown that grafts remain hypoxic for 3–5 days post-transplantation, with revascularization occurring over a 10-day window[18,19]. In this time, insufficient blood flow leads to ischemia and hypoxia within the graft, activating hypoxia response elements to produce inflammatory mediators. These subsequently trigger the migration of neutrophils and macrophages into the tissue which causes tissue damage and fibrosis[20].

Tissue injury arising from avascular transplantation disrupts the stromal and vascular microenvironments which support follicle survival[21]. Within the native ovarian cortex, PFs are naturally avascular and receive nutrients and oxygen via passive diffusion from nearby blood vessels[22]. Although PFs may be more resistant to ischemic injury compared to endothelial and other stromal cell populations[20], transplantation-associated ischemia likely contributes to the substantial follicle loss observed upon grafting[21]. Additionally, damage to the stromal microenvironment may alter signaling pathways involved in maintaining follicle quiescence [21], potentially contributing to abnormal follicle activation and growth that cannot be sustained in injured tissue. Thus, disruption of the ovarian tissue microenvironment likely contributes to follicle apoptosis and abnormal follicle activation observed post-transplantation, though the specific factors and mechanisms eliciting these responses remain under investigation.

Paradoxically, restoration of blood flow can further exacerbate tissue injury through ischemia-reperfusion mechanisms[23]. Following ischemia, reoxygenation of the graft leads to overproduction of reactive oxygen species (ROS), resulting in oxidative stress, inflammation, and additional cellular damage. Studies have found that ROS levels peak in ovarian grafts around the time revascularization occurs and follicle loss continues during this reperfusion phase[19]. Approximately 60% of follicles are lost within the first 10 days post-transplantation – prior to the ROS peak – followed by an additional 20% follicle loss. Together, ischemic and reperfusion injuries arise as consequences of avascular transplantation and contribute to reduced graft functional longevity in OTCT. These consequences have motivated the development of biomaterial-based strategies aimed at modulating the graft microenvironment and vascular integration following ovarian tissue transplantation.

1.4 Biomaterials for OTCT

Various strategies have been explored to improve OTCT outcomes, including delivery of growth factors, vitamins, anti-apoptotic agents, antioxidants, and hormones[21,24,25]. Within this landscape, biomaterial scaffolds have emerged as a promising approach for modulating graft vascular integration following avascular transplantation. Reported biomaterials include human recombinant type I collagen[26], porcine small intestinal submucosa[26], fibrin[27], and gelatin hydrogels[28]. Studies employing these materials in human ovarian tissue xenograft models have demonstrated improvements in graft revascularization, stromal integrity, and follicle survival compared to non-encapsulated controls. In some cases, these scaffold-based approaches have been combined with systemic or localized delivery of agents such as simvastatin[27] or basic fibroblast growth factor[28], respectively, further supporting vascular ingrowth and tissue integrity.

Beyond serving as scaffolds for ovarian tissue alone, biomaterials have also been leveraged as delivery vehicles for support cells, including mesenchymal stem cells (MSCs)[29,30], adipose tissue-derived stem cells (ASCs)[31–34], and exogenous endothelial cells (ExECs)[35]. In human ovarian tissue xenograft models, co-delivery of ovarian tissue with such support cells has been shown to increase graft revascularization and improve follicle survival. These results have been attributed to the support cells' secretion of pro-angiogenic factors, differentiation into endothelial cell lineages, and anastomosis with host vasculature.

Together, these studies demonstrate that biomaterials can modulate revascularization dynamics and tissue outcomes following ovarian tissue transplantation. Importantly, translational feasibility of this approach is supported by clinical use of AlloDerm – a commercially available decellularized human extracellular tissue matrix (ECTM) – which has been associated with increased graft longevity in patients undergoing OTCT[36]. Although the small sample size makes

it difficult to attribute increased graft longevity solely to the ECTM scaffold, this finding provides encouraging evidence that biomaterial-based strategies can improve OTCT outcomes.

Nonetheless, the biomaterials investigated to date for human ovarian tissue transplantation have relied on naturally derived materials. While these biomaterials offer high biocompatibility and inherent bioactivity, they are limited by batch-to-batch variability and lack of orthogonal control over mechanical and biological properties which can hinder clinical translation. These design trade-offs motivate the exploration of synthetic, modular biomaterials that enable precise tuning of scaffold architecture and functionality to address the challenges associated with avascular transplantation in OTCT.

1.5 Microporous Annealed Particle (MAP) Hydrogels

Synthetic biomaterials enable control over scaffold parameters that influence graft integration. Among these, scaffold porosity plays an important role in modulating cellular infiltration and vascular remodeling. Granular hydrogels – a class of "open pore" scaffolds made of micron-scale hydrogels ("microgels") – have attracted interest for their ability to facilitate endogenous tissue repair and vascular integration[37]. Microporous annealed particle (MAP) hydrogels represent a specific subclass distinguished by secondary crosslinks between the microgel subunits which produce a uniform, interconnected cell-scale porous network[38]. In contrast to conventional bulk hydrogels, which form nanoporous networks that restrict host cell infiltration until material degradation occurs, MAP hydrogels are intrinsically microporous at the time of delivery. This architecture permits immediate cellular infiltration and facilitates vascular ingrowth without the need for material degradation.

Prior MAP hydrogel studies indicate that scaffold architecture is an important determinant of vascular integration. The first report of a synthetic MAP hydrogel in a mouse skin

wound-healing model found increased vascular ingrowth accompanied by endothelial cell and pericyte recruitment within one week post-implantation, achieved without exogenous growth factor delivery[38]. Since then, subsequent studies have shown that vascular responses within MAP hydrogels can also be modulated through microgel porosity[39] and size[40]. In parallel, MAP hydrogels have been functionalized to sequester endogenous growth factors, thereby supporting vessel formation and maturation[41,42]. Collectively, these studies establish MAP hydrogels as a modular biomaterial platform in which structural and biochemical properties can be independently tuned to modulate vascular integration.

1.6 Gaps in Characterization of Human Ovarian Tissue

While substantial effort has been directed toward engineering strategies that improve graft integration following ovarian tissue transplantation, progress in OTCT is also shaped by incomplete quantitative understanding of human ovarian tissue itself. Human ovarian tissue is highly heterogeneous, exhibiting variability in follicle number, follicle spatial distribution, and vascular organization both between patients and within individual ovaries. This inherent heterogeneity likely influences tissue response to cryopreservation and transplantation yet remains incompletely defined.

Assessment of ovarian tissue structure currently relies on two-dimensional histological analysis of thin tissue sections[43]. Although histology can provide high-resolution cellular information, it samples only a small fraction of the total tissue volume and is therefore susceptible to sampling bias. This limitation is significant given that key ovarian features implicated in OTCT outcomes, including follicles, stromal compartments, and vasculature, are organized three-dimensionally across length scales that are not well-captured by sparse two-dimensional sections.

Tissue clearing and three-dimensional imaging approaches address this limitation by enabling volumetric visualization of intact tissues at cellular resolution while preserving native spatial relationships. When applied to human ovarian tissue, clearing permits three-dimensional visualization and quantification of follicle populations, vascular networks, and tissue composition across whole tissue pieces. As such, these approaches provide a means to better characterize ovarian tissue heterogeneity and structure preservation after cryopreservation and transplantation, thereby generating quantitative metrics that may assist interpretation of tissue fate after transplantation.

1.7 Dissertation Overview

This dissertation employs quantitative tissue characterization methods and biomaterial scaffolds to examine strategies for supporting transplanted human ovarian tissue within the context of OTCT. In Chapter 2, we develop and apply tissue clearing and three-dimensional imaging methods to cryopreserved human ovarian tissue. This chapter establishes a framework for volumetric characterization of intact ovarian tissue, enabling quantitative assessment of follicle density and vascular organization within their native tissue architecture. In Chapter 3, we investigate a MAP hydrogel as a synthetic, modular biomaterial platform for human ovarian tissue transplantation using a xenograft mouse model of POI. Tissue clearing and three-dimensional imaging methods developed in Chapter 2 are applied to transplanted grafts to assess host and graft vasculature over time. Accordingly, this chapter evaluates the influence of scaffold architecture on graft vascular dynamics and endocrine function following transplantation. Chapter 4 summarizes our findings within the broader landscape of fertility preservation and discusses future directions for ovarian tissue characterization and biomaterial platforms for ovarian tissue transplantation. Overall, this dissertation establishes tissue clearing as an

analytical tool for human ovarian tissue and demonstrates, for the first time, that a MAP hydrogel scaffold can support revascularization and functional integration of human ovarian grafts.

Chapter 2 Three-Dimensional Characterization of Follicular and Vascular Architecture in Human Ovarian Tissue

2.1 Introduction

The human ovary is a spatially heterogeneous organ composed of the finite ovarian follicle reserve and a complex stroma that, together, underlie reproductive lifespan and long-term endocrine health. The ovarian cortex is a dense stromal region enriched in clusters of primordial and early growing follicles. In contrast, the ovarian medulla is less dense and more highly vascularized, containing larger follicles that remodel their surrounding microenvironment as they approach pre-ovulatory stages. Across both regions, follicles are supported by vasculature, nerves, immune cells, diverse stromal cell populations, and extracellular matrix[44]. Although these components are well described in two-dimensional histological sections, their three-dimensional organization within intact human ovarian tissue remains incompletely characterized.

This gap is driven largely by reliance on section-based methodologies. Histology has long served as the primary method for studying ovarian tissue structure, function and composition; however, histology reduces complex three-dimensional structures to two-dimensional snapshots, limiting reconstruction of spatial relationships across large tissue volumes. Emerging spatial transcriptomic approaches have expanded our understanding of ovarian cellular composition and function based on cell location[45–47], yet these methods are likewise constrained to thin histological sections and, as a result, do not capture the heterogeneous three-dimensional context of the human ovary. Consequently, reproducible

methods that preserve and resolve three-dimensional human ovarian microarchitecture are needed.

Tissue clearing offers a strategy to meet this need by rendering tissue optically transparent via reduction of light scattering, thereby enabling three-dimensional fluorescence imaging of large tissue volumes and even whole organs. Clearing has been widely adopted to investigate ovarian biology in mice, including follicle dynamics and vascular organization[48–55]. Translation to human ovarian tissue, however, requires validation as differences in stromal density, follicle distribution, and tissue scale[56] can alter clearing efficiency, antibody penetration, and achievable imaging depth. While a limited number of studies have applied tissue clearing to human ovarian tissue[57–59], standardized workflows for clearing and three-dimensional imaging of intact human ovarian tissue remain scarce.

Three-dimensional characterization of human ovarian tissue is particularly relevant for fertility preservation strategies such as ovarian tissue cryopreservation and transplantation (OTCT), where preservation of the follicle reserve and timely vascular integration influence graft viability and endocrine function restoration. However, OTCT outcomes remain variable, in part because ovarian tissue architecture and post-transplantation responses remain incompletely understood. Follicle depletion shortly after tissue grafting has been attributed to ischemia and reperfusion injuries, but the relative contributions of follicle apoptosis, dysregulated follicle activation, stromal disruption, and vascular remodeling remain unclear. Since these processes occur within a structurally complex and heterogeneous tissue environment, quantitative, three-dimensional mapping of follicles and surrounding vasculature and stromal compartments in intact ovarian tissue may inform both interpretation of OTCT outcomes and bioengineering

strategies aimed at improving OTCT outcomes. Imaging approaches that are reliable and compatible with human ovarian tissue are therefore needed to support these applications.

Here, we establish a reproducible tissue clearing and volumetric imaging workflow for human ovarian tissue and demonstrate its use for follicle and vasculature readouts. Immunolabeling is implemented for follicle detection in cleared cortex, enabling quantification of follicle density and comparison to conventional histological measurements. Light sheet microscopy is subsequently applied to visualize cortical vasculature architecture and quantify vascular morphometrics. Finally, imaging modalities are compared to define practical considerations for volumetric analysis of human ovarian tissue. Collectively, this work provides a validated framework for three-dimensional characterization of microarchitecture in clinically relevant cryopreserved human ovarian tissue, addressing a key methodological gap in ovarian tissue analysis.

2.2 Materials and Methods

2.2.1 Ethical Approval for the Procurement of Human Ovaries

As previously described[56,60], whole human ovaries were obtained from deceased donors for non-clinical research through the International Institute for the Advancement of Medicine (IIAM) and associated Organ Procurement Organizations (OPOs). IIAM and the associated OPOs comply with state Uniform Anatomical Gift Acts (UAGA) and are certified and regulated by the Centers for Medicare and Medicaid Services (CMS). These OPOs are members of the Organ Procurement and Transplantation Network (OPTN) and the United Network for Organ Sharing (UNOS) and operate under standards established by the Association of Organ Procurement Organizations (AOPO) and UNOS. Informed, written consent was obtained from the deceased donors' families prior to tissue procurement for the tissue used in this study. A

biomaterial transfer agreement is in place between IIAM and the University of Michigan that restricts the use of the tissue to pre-clinical research not involving the fertilization of gametes. The use of deceased donor ovarian tissue in this research is categorized as "not regulated" per 45 CFR 46.102 and the "Common Rule" as it does not involve human subjects and therefore complies with the University of Michigan Institutional Review Board (IRB) requirements.

2.2.2 Collection of Human Ovarian Tissue

Human ovarian tissue was procured from four deceased donors (**Table 2.1**) who were of reproductive age and did not have a medical history indicative of conditions that would affect ovarian function. Upon arrival in the laboratory, donor ovaries were transferred to pre-cooled holding media composed of Quinn's Advantage Medium with HEPES (QAMH, ART-1024, CooperSurgical, USA) supplemented with 10% Quinn's Advantage Serum Protein Substitute (SPS, ART-3010, CooperSurgical, USA). The outer cortex layer was collected from the ovaries using a custom cutting guide (Reprolife, Japan) which produced tissue squares measuring approximately 1 mm in thickness and 10 mm in both length and width. Cortical squares were then cryopreserved using a previously published slow freezing protocol[56,60,61]. The remaining ovarian tissue, including the ovarian medulla, was fixed in 4% paraformaldehyde (PFA, J61899AK, Thermo Scientific Chemicals, USA) for 24 hours at 4ºC. PFA-fixed tissue was then washed in Dulbecco's phosphate-buffered saline (DPBS, 14190250, Gibco, USA) for 1 hour and stored in 70% ethanol (EtOH) at 4ºC.

Table 2.1 Donor Information

Donor	Age (years)	BMI (kg/m^2)	CIT (hours)
A	31	37.7	27.7
B	28	22.7	20.4
C	31	24.2	29.9
D	34	24.4	10.5

BMI: body mass index; CIT: cold ischemic time.

2.2.3 Preparation of Samples for Tissue Clearing

To prepare ovarian cortex for tissue clearing, cortex squares were thawed following a previously described protocol[60,61]. Briefly, cryovials containing cortex were removed from liquid nitrogen and left at room temperature for 30 seconds before being immersed in a 37ºC water bath. Once the cryoprotectant medium had thawed (after approximately 1.5 minutes), the tissue was removed from the vial and placed into the first thawing solution (QAMH with 10% SPS, 0.5 M dimethyl sulfoxide (DMSO, D2650, Sigma-Aldrich, USA), 0.5 M Ethylene Glycol (102466, Sigma-Aldrich, USA), 0.1 M Sucrose (S1888, Sigma-Aldrich, USA)) for ten minutes. The tissue was then sequentially incubated in the second thawing solution (QAMH with 10% SPS, 0.25 M DMSO, 0.25 M Ethylene Glycol, 0.1 M Sucrose), the third thawing solution (QAMH with 10% SPS, 0.1 M Sucrose), and the fourth thawing solution (QAMH with 10% SPS) for ten minutes each. The fourth thawing solution served as a maintenance solution. All four solutions were equilibrated to room temperature for the thawing procedure. Thawed cortex squares were then manually cut into strips measuring approximately 5 mm in length and 1 mm in width. Cortex strips were subsequently fixed in 4% PFA for 24 hours at 4ºC and then washed three times in DPBS for 1 hour each prior to being moved into 70% EtOH at 4ºC for long-term storage. Medullary tissue was dissected from the fixed ovary remains and then manually cut into smaller pieces prior to undergoing the tissue clearing process.

2.2.4 Clearing of Tissues with Modified CUBIC Clearing Protocol

The CUBIC tissue clearing protocol described by Matsumoto et al. was adapted to clear human ovarian cortex and medulla samples[62]. The protocol can broadly be separated into three phases: (1) delipidation, (2) staining, and (3) refractive index (RI) matching (**Table 2.2**). The delipidation phase began by immersing the prepared fixed tissue samples in an equivalent

volume mixture of dH_2O and CUBIC-L (10% (wt/wt) N-butyldiethanolamine (B0725, TCI America, USA), 10% (wt/wt) Triton X-100 (X100, Sigma-Aldrich, USA), 80% (wt/wt) dH_2O) with shaking at 37°C overnight. The next day, this mixture was replaced with fresh CUBIC-L. CUBIC-L was refreshed every 48 hours for a total CUBIC-L incubation duration of 10 days. At the end of 10 days, to stop the delipidation process, samples were washed with 1X phosphate buffered saline (PBS) with shaking at room temperature for at least 2 hours. This washing step was repeated more than three times.

Samples used for evaluation of imaging depth were stained with propidium iodide (PI, P3566, Molecular Probes, USA). To achieve this, the samples were immersed in staining buffer (1.5M NaCl in 1X PBS) with shaking at room temperature twice for at least 2 hours each time. Then, the samples were moved to a staining buffer solution containing 30 μg/mL PI and were incubated for 3 days at 37°C with shaking. After the dye incubation step, the samples were washed with 1X PBS with shaking at room temperature overnight. To initiate the RI-matching phase of the CUBIC clearing protocol, the samples were then immersed in an equivalent volume mixture of dH_2O and CUBIC-R+(M) (45% (wt/wt) antipyrine (D1876, TCI America, USA), 30% (wt/wt) N-methyl-nicotinamide (M0374, TCI America, USA), 0.5% (vol/vol) N-butyldiethanolamine, 24.5% (wt/wt) dH_2O) with shaking at room temperature overnight. Next, this mixture was replaced with fresh CUBIC-R+(M) and the samples were incubated with shaking at room temperature overnight. The next day, CUBIC-R+(M) was refreshed and the samples were incubated for an additional day. After this final CUBIC-R+(M) incubation step, the samples were ready for imaging. The non-cleared samples did not undergo CUBIC-L delipidation or CUBIC-R RI-matching but were subjected to PI staining.

Samples used for evaluation of follicle density were stained using immunofluorescence labeling. After the delipidation phase, the samples were immersed in blocking solution (5% normal goat serum (ab138478, Abcam, USA) in 1X PBS) with shaking at 37ºC overnight. The samples were then incubated in a solution consisting of primary antibody (ZP3, 1:250, sc-398359, Santa Cruz Biotechnology, USA) diluted in blocking solution with shaking at 37ºC for 3 days. Following this step, the samples were washed in blocking solution three times with shaking at room temperature for 1 hour each. Next, the samples were incubated in a solution containing secondary antibody (Goat anti-Mouse, Alexa Fluor Plus 647, 1:1000, A32728, Invitrogen, USA) and nuclear counterstain (DAPI, 1:1000, D1306, Invitrogen, USA) diluted in blocking solution with shaking at 37ºC for 3 days. Finally, the samples were washed in 1X PBS three times with shaking at room temperature for 1 hour each before proceeding to the RI-matching phase described above.

Samples used for evaluation of vasculature were prepared using a modified version of the immunofluorescence labeling protocol described above. After the delipidation phase, the samples were immersed in blocking solution (5% normal goat serum in 1X PBS) with shaking at 37ºC overnight. The samples were then incubated in a solution consisting of Ulex Europaeus Agglutinin I (UEA I, DyLight 649, 1:250, DL-1068-1, Vector Laboratories, USA) and nuclear counterstain (DAPI, 1:1000, D1306, Invitrogen, USA) diluted in blocking solution with shaking at 37ºC for 3 days. The samples were then washed in 1X PBS three times with shaking at room temperature for 1 hr each. Next, samples were mounted in 1 mL syringes in agarose (2% (wt/wt), Agarose for ≧1kbp fragment, 01163-76, Nacalai USA, USA). Finally, the mounted samples were subjected to the RI-matching protocol described above.

Table 2.2 CUBIC Clearing and Staining Timelines

Day	PI Staining	ZP3 Staining	UEA Staining
1	1/2 CUBIC-L	1/2 CUBIC-L	1/2 CUBIC-L
2	CUBIC-L	CUBIC-L	CUBIC-L
3			
4	Refresh CUBIC-L	Refresh CUBIC-L	Refresh CUBIC-L
5			
6	Refresh CUBIC-L	Refresh CUBIC-L	Refresh CUBIC-L
7			
8	Refresh CUBIC-L	Refresh CUBIC-L	Refresh CUBIC-L
9			
10	Refresh CUBIC-L	Refresh CUBIC-L	Refresh CUBIC-L
11			
12	Wash	Wash + Block	Wash + Block
13	PI	ZP3	UEA and DAPI
14			
15			
16	Wash	Wash + Secondary/DAPI	Wash + 1/2 CUBIC-R+
17	1/2 CUBIC-R+		CUBIC-R+
18	CUBIC-R+		Refresh CUBIC-R+
19	Refresh CUBIC-R+	Wash + 1/2 CUBIC-R+	
20		CUBIC-R+	Image
21	Image	Refresh CUBIC-R+	
22			
23		Image	

2.2.5 Linear Expansion of Tissue

To assess tissue linear expansion as a result of clearing, the two-dimensional size of tissue samples was measured throughout the clearing protocol. Tissue pieces were placed on a glass dish with a ruler and imaged using a stereo microscope. Initial images of the tissue pieces were taken prior to starting the clearing protocol. Then, additional images were collected throughout the clearing protocol at the time points designated in **Table 2.3**. To quantify the images, tissue area was measured by thresholding images in FIJI (ImageJ)[63]. Linear expansion was calculated by normalizing the area of the cleared tissue with the area of the same tissue prior to starting the clearing protocol. Then the square root of this area size change was calculated.

Table 2.3 Linear Expansion Imaging Timeline

Protocol Day	Protocol Step	Imaging Notes
0		Initial image
1	1/2 CUBIC-L	
2	CUBIC-L	Image before moving to CUBIC-L
3		
4	Refresh CUBIC-L	Image
5		
6	Refresh CUBIC-L	Image
7		
8	Refresh CUBIC-L	Image
9		
10	Refresh CUBIC-L	Image
11		
12	Wash + Block	Image before and after washes
13	UEA and DAPI	Image before incubation
14		
15		
16	Wash + 1/2 CUBIC-R+	Image before and after washes
17	CUBIC-R+	Image before moving to CUBIC-R
18	Refresh CUBIC-R+	Image
19		
20	Image	Image

2.2.6 Imaging Depth

To assess imaging depth before and after clearing, cleared and non-cleared tissue pieces were stained with PI. One z-stack of 500 µm with a z-step of 2.409 µm was acquired for each tissue piece on a Leica SP8 laser scanning confocal microscope. The laser power and gain were maintained across all tissue pieces. Imaging depth was calculated from contrast decay. Image contrast can be described by Equation 1 where I corresponds to the grayscale value (or intensity) for each pixel, I_{mean} is the average intensity of the image, and n is the total pixel count in the image. Accordingly, image contrast was acquired by measuring the standard deviation of the gray values for each image slice throughout the z-stack in FIJI (ImageJ) (Equation 2). Contrast values for each image were then normalized to the maximum contrast value in the image z-stack. Imaging depth was defined as the depth where contrast drops to ½ of the maximum contrast in

the z-stack (i.e. the depth at which normalized contrast was equal to 0.5 given that the maximum normalized contrast was equal to 1).

$$contrast = \sqrt{\frac{\Sigma(I - I_{mean})^2}{n - 1}} \quad (1)$$

$$Standard\ deviation\ as\ calculated\ by\ ImageJ/FIJI = \sqrt{\frac{\Sigma(x_i - \bar{x})^2}{n - 1}} \quad (2)$$

2.2.7 Evaluation of Follicle Density using Tissue Clearing

Follicle density was measured by staining cleared cortex tissue with ZP3 as described above. Tile scans (z-stack depth: 500 μm; z-step size: 2.5 μm) encompassing the full detectable tissue area were acquired using a Leica SP8 laser scanning confocal microscope. Follicles throughout the z-stacks were manually counted in the DAPI channel in FIJI (ImageJ), ensuring not to double-count follicles that spanned across multiple z-slices. Follicles were marked on a z-slice once the oocyte was fully visible. Follicle counts were then validated using the ZP3 channel. To calculate follicle density, tissue area was measured using FIJI (ImageJ). Specifically, starting from the top of the z-stack, tissue area was measured every 50 μm which corresponds to every 20th z-slice. The volumes of these tissue sub-stacks were calculated by multiplying the tissue area with its respective height of 50 μm. Follicle density was then calculated for each tissue sub-stack as the total number of follicles in the sub-stack divided by the sub-stack tissue volume.

2.2.8 Evaluation of Follicle Density using Histology

Follicle density was assessed throughout a subset of fresh ovarian cortex samples which were fixed in Bouin's fixative (Ricca Chemical, USA) at the time of tissue collection rather than cryopreserved. Samples were fixed at 4ºC overnight and then washed in dH_2O for 1 hour, 50%

EtOH for 1 hour, 70% EtOH for 1 hour, and finally stored in 70% EtOH at 4ºC. The fixed tissue samples were then embedded in paraffin at the University of Michigan Dental School Histology Core and serially sectioned at a thickness of 5 μm, producing four sections per slide for up to 50 slides per tissue sample. Every other slide was stained with hematoxylin and eosin (H&E) and imaged using a digital slide scanner (Leica Aperio AT2, Leica Biosystems, Germany) at 20x magnification at the University of Michigan Unit for Laboratory Animal Medicine Pathology Core.

Whole slide scans were imported into QuPath analysis software (v0.2.2) for manual follicle counting, as previously described[64]. Briefly, every 8th tissue section was analyzed for follicles with 20 sections analyzed for donors A and B, 24 sections analyzed for donor C, and 25 sections analyzed for donor D. Analysis of every 8th tissue section corresponded to a sampling spacing of 40 μm which prevented duplicate counts of a singular primordial follicle as they are approximately 40 μm in diameter[65]. As such, all primordial follicles were counted for each analyzed tissue section. Larger follicles were counted after comparing the preceding and subsequent tissue sections to prevent duplicate counts. To calculate tissue volume, tissue section area was multiplied by a tissue thickness of 20 μm rather than 40 μm to account for smaller primordial follicles that could have been omitted in between every 8th tissue section that was analyzed. Follicle density for each analyzed tissue section was then calculated as the total number of follicles in the tissue section divided by the tissue section volume.

2.2.9 Evaluation of Cortex Vasculature

Vasculature in human ovarian cortex samples was visualized by staining cleared tissue with UEA-1 as described above. Light sheet images (z-step size: 2.917 μm) were acquired using

a Zeiss Lightsheet 7 at the University of Michigan BRCF Microscopy Core. Tile alignment was performed using Zeiss arivis Pro.

For quantitative analysis, image datasets were imported into Imaris. A region of interest (ROI) corresponding to ovarian cortex was defined based on tissue morphology, vascular features, and follicle stage composition. Within this ROI, vasculature was segmented by generating a surface with the Machine Learning Segmentation module. The resulting surface was analyzed with the Filament Tracer module to quantify total branch points, total filament length, total filament volume, and segment diameters. Total filament length and segment diameters were corrected for tissue linear expansion. Vessel length density and branch point density were calculated by using the expansion-adjusted ROI volume.

2.2.10 Statistical Analysis

All statistical analysis was performed in GraphPad Prism 10. Unless otherwise noted, data is expressed as mean ± standard deviation (mean ± SD). Error bars throughout figures are mean ± standard deviation per group.

2.3 Results

2.3.1 Adapting and Characterizing a Clearing Protocol for Human Ovarian Tissue

Among existing tissue clearing approaches, we selected CUBIC (clear, unobstructed brain imaging cocktails and computational analysis)[62,66] for its versatility and proven performance across tissue types, including mouse ovaries[55]. To accommodate the larger size and denser stromal architecture of human ovarian tissue, the CUBIC protocol was adapted by extending the duration of its three major phases (**Figure 2.1, A**): (1) delipidation in CUBIC-L (~10 days), (2) sample labeling (~4–7 days depending on labeling method), and (3) refractive

index (RI) matching in CUBIC-R (~4 days). Implementation of this adapted protocol resulted in optically transparent ovarian cortex and medulla tissue (**Figure 2.1, B**).

Because aqueous-based clearing protocols such as CUBIC can induce tissue expansion through hyper-hydration, changes in sample size over the course of clearing were quantified. By the end of the clearing protocol, both cortex and medulla exhibited a mean linear expansion factor of 1.2 relative to baseline starting size (**Figure 2.1, C**), providing quantitative characterization of CUBIC-associated expansion of human ovarian tissue.

To validate clearing performance, we compared imaging depth in control and cleared cortex and medulla samples from four donors using confocal microscopy (**Figure 2.1, D**). Imaging depth was determined by contrast decay across z-stacks for each tissue piece (**Figure 2.1, E**). Cleared cortex showed an approximately 6.5- to 11-fold increase in imaging depth relative to non-cleared controls and cleared medulla exhibited an approximately 6- to 8-fold increase, confirming significantly improved light penetration and increased imaging depth capability in both tissue regions.

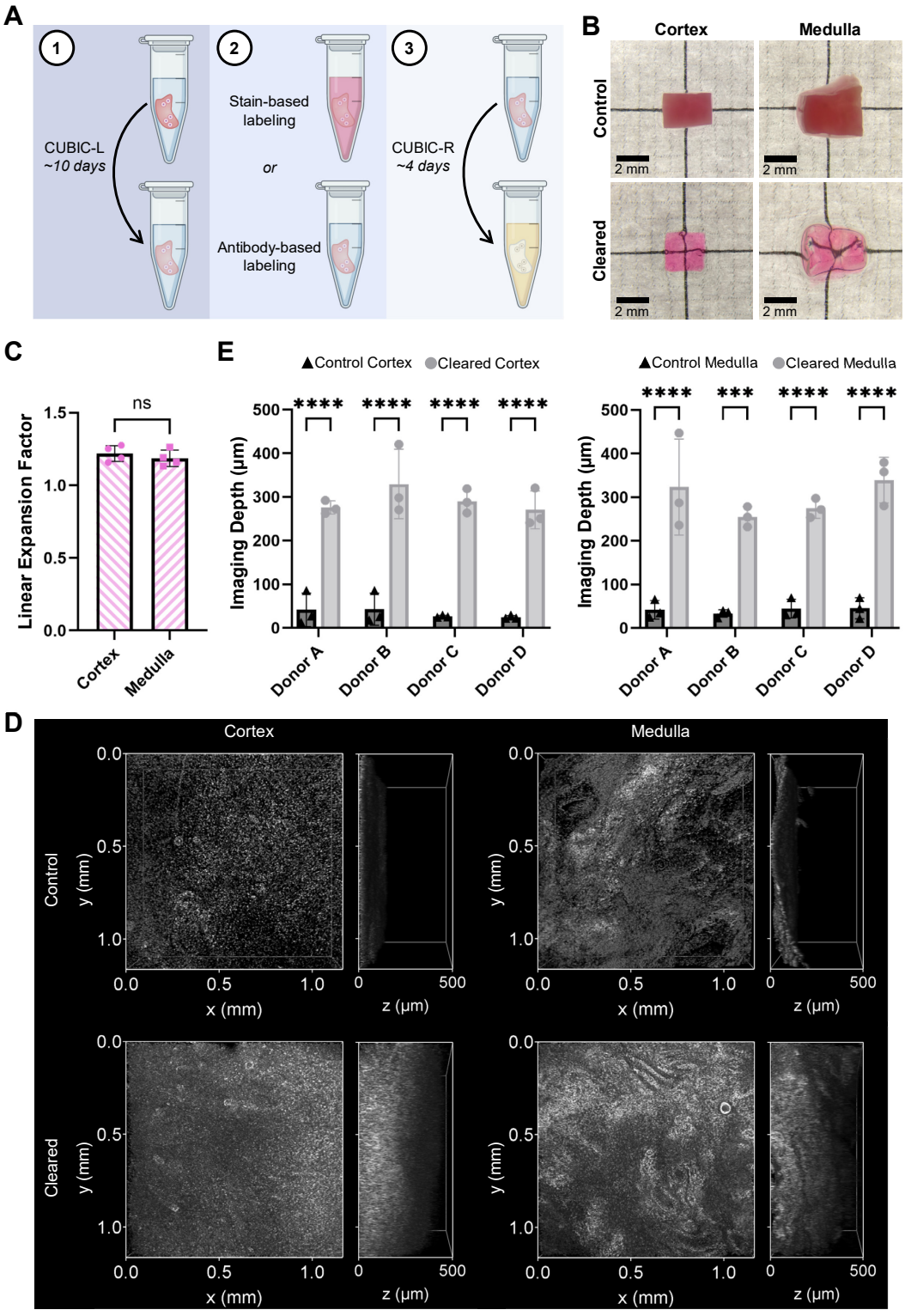


Figure 2.1 Adapted CUBIC Protocol Characterization for Human Ovarian Tissue. (A) Overview of the three major CUBIC protocol phases. **(B)** Cortex and medulla processed with the adapted CUBIC protocol become optically transparent, enabling visualizing of the millimeter paper grid below. **(C)** Cleared cortex and medulla undergo similar expansion due to CUBIC clearing. Each data point represents the terminal linear expansion for a tissue piece (n = 4 tissue pieces per condition), error bars are mean ± standard deviation. Data analyzed by Mann-

Whitney test, $p < 0.05$, ns = not significant. **(D)** Representative confocal images depicting an X-Y plane and Z imaging depth for control and cleared cortex and medulla. **(E)** CUBIC clearing increases imaging depth for both cortex and medulla across different tissue sources. Each data point represents the imaging depth for one tissue piece within the respective donor (n = 3 tissue pieces per donor), error bars are mean ± standard deviation. Data analyzed by two-way ANOVA with Šidák's multiple comparisons test, $p < 0.05$, significant difference indicated as *$p \leq 0.05$, **$p \leq 0.01$, ***$p \leq 0.001$, ****$p \leq 0.0001$.

2.3.2 Follicle Detection in Cleared Human Ovarian Cortex

Next, we evaluated whether cleared cortex was suitable for analyzing biologically and clinically relevant measurements, such as follicle density, which is typically derived from two-dimensional histologic sections. To achieve this, cortical tissue was labeled for zona pellucida protein 3 (ZP3), which localizes to the extracellular matrix surrounding the oocyte. Cleared tissue was then imaged by confocal microscopy and follicles were identified morphologically in the DAPI channel with ZP3 labeling used for confirmation (**Figure 2.2, A**).

Follicle density was subsequently calculated within defined z-stack substacks for each tissue piece, enabling evaluation of follicle distribution throughout the imaged volume (**Appendix Table A.1, Appendix Figure A.1**). This analysis revealed heterogeneity both within and between donors. Donor A, for instance, showed notable variability across the analyzed tissue pieces with densities of 9 ± 9, 115 ± 58, and 35 ± 26 follicles/mm^3. Across Donors B, C, and D, mean follicle densities ranged from 7–22, 1–7, and 1–16 follicles/mm^3, respectively, further demonstrating the known intra- and inter-donor follicle distribution variability characteristic of human ovarian cortex.

Comparison of follicle densities from cleared tissue to follicle densities obtained by conventional histology (**Figure 2.2, B–C**) revealed no statistically significant difference for all the analyzed donors, indicating that follicle density quantification in cleared tissue was comparable to standard histology while still preserving three-dimensional context.

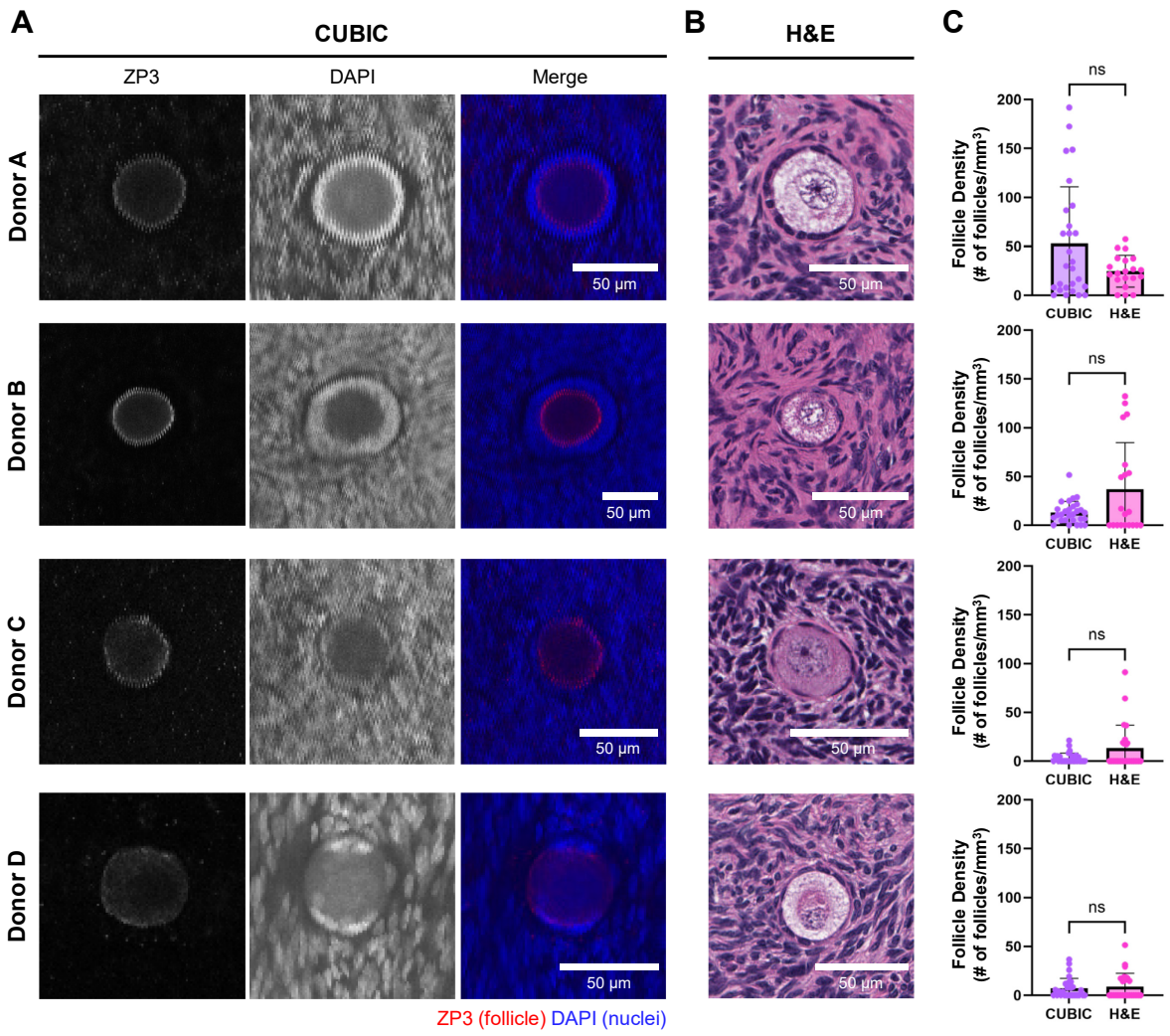


Figure 2.2 Follicle Detection and Quantification in Cleared Human Ovarian Cortex. (A) Representative confocal z-slices of follicles in cryopreserved cleared tissue depicting ZP3 and DAPI channels, and the merged images. **(B)** Representative histological H&E images of follicles from fresh donor-matched tissue. **(C)** Comparison of follicle densities computed from CUBIC-cleared tissue and histological H&E images for each donor. Each data point represents the follicle density from a confocal z-stack substack (CUBIC) or a histological section (H&E), error bars are mean ± standard deviation. Data analyzed by Mann-Whitney test, $p < 0.05$, ns = not significant.

2.3.3 Quantitative Mapping of Human Ovarian Cortical Vasculature

Given that follicle health and development is tied to stromal vascular support, especially in the context of ovarian tissue cryopreservation and transplantation, we next examined native vasculature architecture within cleared human ovarian cortex. Tissue samples were labeled with UEA-1 lectin and imaged using light sheet microscopy, generating whole-tissue datasets that

enabled visualization of vascular networks across intact tissue pieces (**Figure 2.3**, **A**). For quantitative analysis, segmentation of vessel networks was restricted to sub-volumes consistent with cortical morphology (identified by the presence of small follicles, when possible) in order to minimize the inclusion of medullary regions. Within these regions of interest, vasculature was identified, traced (**Figure 2.3, Ai**), and analyzed to extract morphometric parameters, including mean vessel diameter (**Figure 2.3, Aii**), branch point density, and length density.

Analysis of mean diameters of vessels revealed diameter distributions between 5 μm and 28 μm within individual tissue pieces for each donor (**Figure 2.3, B**). When summarized for each donor, however, mean vessel diameters showed no statistically significant difference between donors (**Figure 2.3, C**). Across donors, mean vessel diameter ranged from 12 μm to 14 μm (**Figure 2.3, C**), mean branch point density ranged from 632 points/mm^3 to 739 points/mm^3 (**Figure 2.3, D**), mean vessel length density ranged from 117 mm/mm^3 to 175 mm/mm^3 (**Figure 2.3, E**), and mean vessel volume fraction ranged from 1.9% to 2.3% (**Figure 2.3, F**). Together, these findings demonstrate that tissue clearing combined with light sheet imaging enables quantitative, volumetric assessment of human ovarian cortical vasculature across intact tissue samples, capturing both local vascular heterogeneity and donor-level metrics.

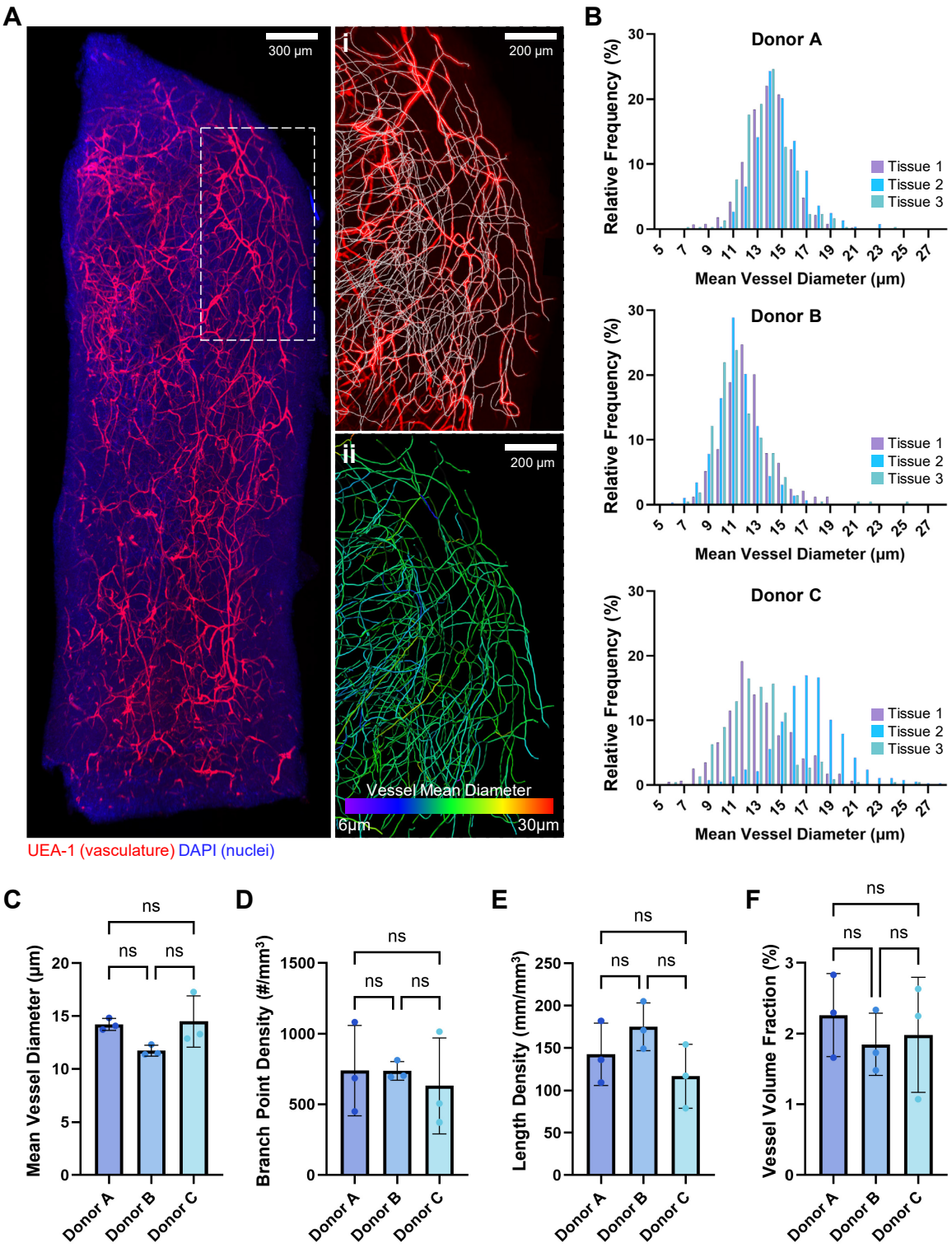


Figure 2.3 Vasculature Mapping in Cleared Human Ovarian Cortex. (A) Representative three-dimensional rendering of cortex vasculature from CUBIC-cleared and light sheet-imaged tissue with **(i)** showing vasculature tracing overlayed with the UEA-1 signal within an ROI and **(ii)** depicting the color-coded mean vessel diameters of the traced vasculature within the ROI. **(B)** Histograms of mean vessel diameter measurements for each donor. Within each histogram, data from three individual tissue pieces are shown and color-coded by tissue piece. For each

tissue piece, blood vessels were automatically detected and segmented, and a mean diameter was calculated for every traced vessel. **(C)** Donor-level summary of mean vessel diameter. Each bar represents one donor and each data point corresponds to the mean of the per-vessel mean diameters for respective tissue pieces. Error bars are donor-level mean ± standard deviation. **(D)** Density of total vessel branch points detected within the analyzed ROI tissue volumes. **(E)** Density of total vessel length detected within the analyzed ROI tissue volumes. **(F)** Total vessel volume per tissue volume within analyzed ROI tissue volumes. Each data point represents the measurement for one tissue piece within the respective donor, error bars are mean ± standard deviation. Data analyzed by Kruskal-Wallis test with Dunn's multiple comparisons test, $p < 0.05$, ns = not significant.

2.3.4 Qualitative Spatial Relationships Between Follicles and Vasculature in Cortex

Next, two-dimensional sections extracted from light sheet datasets were examined to illustrate spatial relationships between follicles and adjacent vasculature within the cleared human ovarian cortex. In one region, a multilayer follicle was located next to a large vessel while a smaller nearby vessel appeared to partially wrap around the follicle (**Figure 2.4, A**). Three-dimensional reconstruction of this region revealed the broader vascular network surrounding the follicle, demonstrating the extent and continuity of vessel segments rarely visualized in a single two-dimensional plane. Additional two-dimensional regions containing clusters of smaller follicles showed variable degrees of vascular proximity (**Figure 2.4, B**). In some regions, vessels were present within the surrounding stroma but remained separated from follicle boundaries, with the nearest vessel located approximately 100 μm (**Figure 2.4, Bi**) or 50 μm (**Figure 2.4, Bii**) from the closest follicle. In other regions, vascular structures approached more closely, located within 10 μm of the nearest follicle (**Figure 2.4, Biii**), and even appeared to extend through the stroma between neighboring follicles (**Figure 2.4, Biv**). These examples highlight the heterogeneous spatial organization of follicles and vasculature within human ovarian cortex and underscore the need for the additional spatial context provided by volumetric imaging of intact tissue.

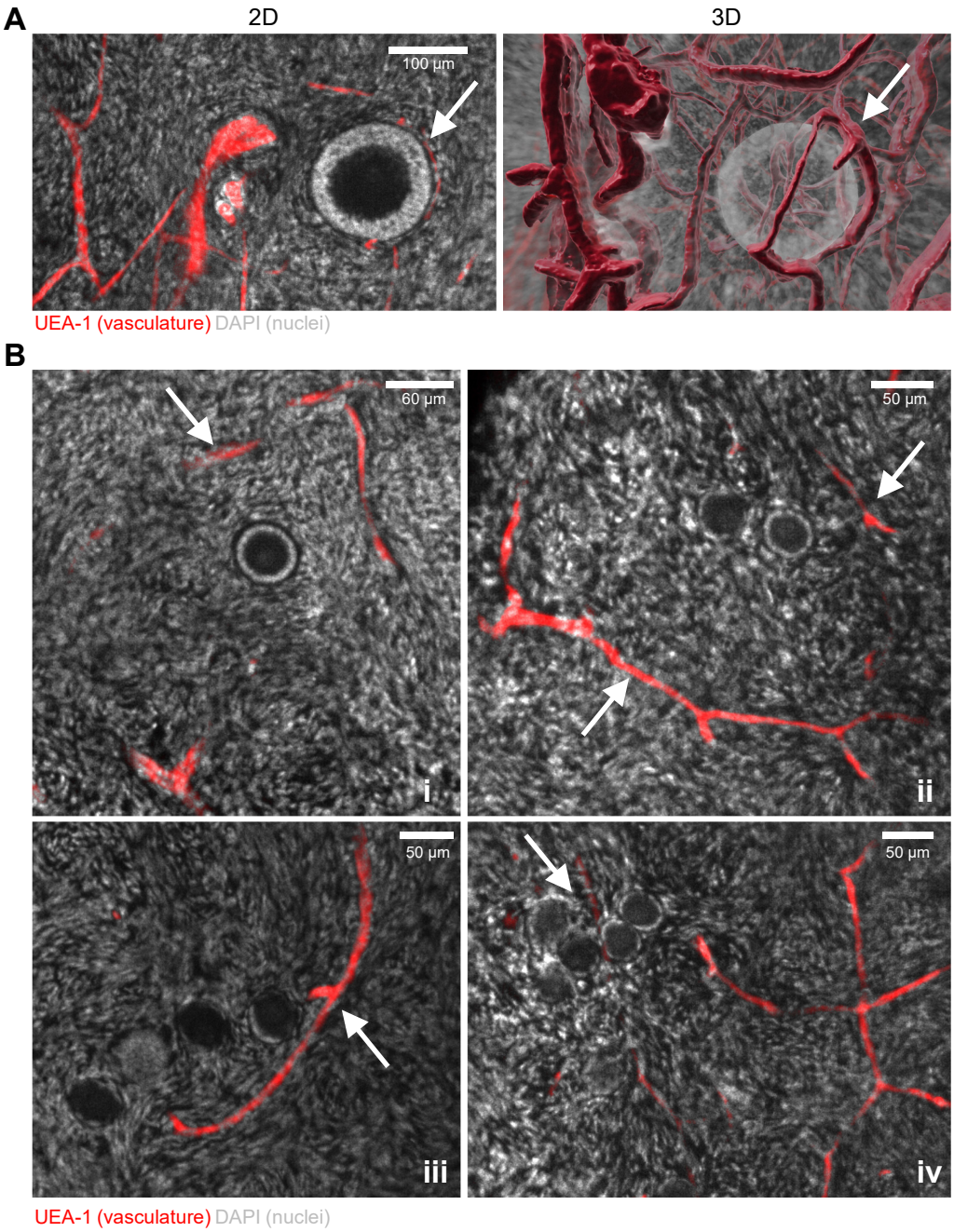


Figure 2.4 Location of Vasculature in Relation to Follicles. (A) Two-dimensional (2D) image of vasculature (white arrow) wrapping around a multilayer follicle. Vasculature traces from the previous vasculature analysis were overlaid with the follicle surface to better visualize the three-dimensional (3D) follicle-vessel spatial relationship. **(B)** Regions of cleared cortex with increasing proximity **(i–iv)** of vasculature (white arrows) to follicles.

2.3.5 Imaging Modality Considerations for Cleared Human Ovarian Tissue

To compare imaging approaches for cleared human ovarian tissue, the same cleared medulla sample was imaged using both confocal and light sheet microscopy. Light sheet microscopy achieved substantially greater imaging depth and covered greater surface area within shorter acquisition times relative to confocal microscopy (**Table 2.4**). These imaging platform differences translated into structural visualization differences. In the confocal dataset, representative sections separated by 180 µm and 160 µm (**Figure 2.5, A**) reconstructed only a limited portion of a large antral follicle. In contrast, light sheet sections separated by 485 µm and 367 µm (**Figure 2.5, B**) resolved a substantially larger fraction of the follicle's three-dimensional structure within the tissue. Despite these differences in volumetric coverage, both modalities captured smaller adjacent follicles as well as surrounding granulosa and stromal cell populations within the medullary region (**Figure 2.5, 5C**).

Table 2.4 Acquisition Parameters and Dataset Characteristics for Cleared Medulla

	Confocal	Light Sheet
Acquisition time	1h 49m	18m
File size (GB)	7.6	80.8
Z-stack size (µm)	499	3929
Z-step size (µm)	2.41	4.01
Z-slice quantity (# slices)	208	980
X dimension (µm)	6390	4930
X pixel size (µm)	1.14	0.92
Y dimension (µm)	6400	6520
Y pixel size (µm)	1.14	0.92
Total frames	7280	11760
Total tiles	35	12

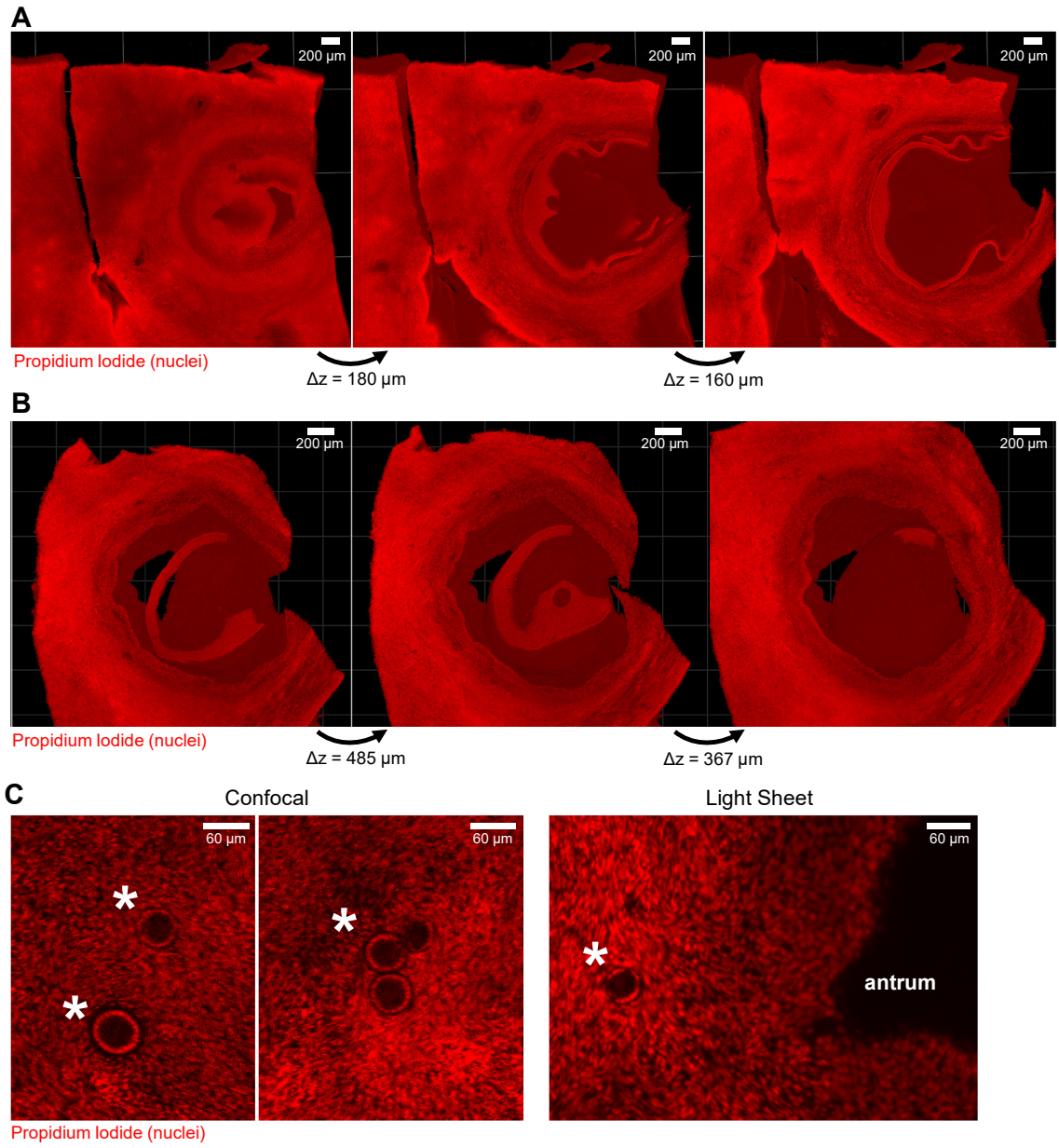


Figure 2.5 Comparison of Confocal and Light Sheet Imaging Modalities. (A) Sequential portions of a confocal z-stack depicting imaging depth capability in reference to an antral follicle structure. **(B)** Sequential portions of a light sheet z-stack of the same tissue piece depicting imaging depth capability in reference to the antral follicle structure. **(C)** Confocal z-slices depicting small follicles and surrounding stroma cells captured in the large medulla piece image. Light sheet z-slice depicting a small follicle and surrounding stroma cells adjacent to the follicle antrum.

2.4 Discussion

This study establishes and validates a tissue clearing and volumetric imaging workflow for human ovarian tissue. By adapting a CUBIC-based protocol to accommodate the structural

density and scale of human cortex and medulla, we achieved three-dimensional analysis of clinically relevant cryopreserved ovarian cortex tissue without physical sample sectioning. Using this workflow, we demonstrated that clearing can be leveraged to interrogate follicle density and vascular architecture within intact three-dimensional volumes.

A primary objective of this work was to determine whether cleared human ovarian tissue could yield biologically meaningful quantitative readouts. Follicle density measurements – key metrics in reproductive biology and fertility preservation – were comparable between tissue clearing and conventional histology. These findings, however, do not necessarily position tissue clearing as a replacement for histological follicle assessment. Histology remains well suited for routine follicle counting and staging, where high-resolution evaluation of follicle morphology is the primary objective. In contrast, clearing offers a complementary approach when the goal is to evaluate follicles together with other structural features within the same intact tissue piece. By enabling volumetric sampling and preservation of spatial context, clearing allows follicles to be visualized and quantified while simultaneously supporting analysis of surrounding stromal and vascular architecture.

Beyond follicle readouts, tissue clearing combined with light sheet imaging enabled volumetric, quantitative characterization of cortical vasculature architecture through assessment of vessel size distributions and network complexity. Additionally, the same cleared tissues allowed simultaneous visualization of follicles and surrounding vasculature. Together, these findings demonstrate that this workflow not only quantifies vascular structures but also preserves the spatial context needed to examine how microenvironmental organization may influence follicle survival and growth.

This preserved spatial context is especially relevant for ovarian tissue cryopreservation and transplantation, where outcomes remain variable and the basis of post-transplantation tissue behavior is incompletely understood. Follicle depletion following transplantation has been linked to ischemic and reperfusion injuries as well as abnormal follicle activation, but it remains unclear how these processes map back to the local organization of follicles, stroma, and vasculature within the graft. Tissue clearing is therefore useful not simply because it allows follicles to be visualized in three dimensions, but because it preserves overall ovarian microarchitecture in a three-dimensional form that may strengthen characterization of cryopreserved tissue and graft remodeling. In this sense, tissue clearing is best viewed as a mechanistic research tool which can be leveraged in studies aimed at improving OTCT outcomes.

Comparison of imaging modalities provides practical considerations for implementation of this workflow. Light sheet microscopy achieved greater imaging depth and volumetric coverage within shorter acquisition times compared to confocal microscopy, facilitating more complete three-dimensional reconstruction of large follicular structures. These advantages, however, were accompanied by substantially larger datasets that required dedicated computational infrastructure and analysis pipelines. Confocal imaging remains more widely accessible and typically generates datasets that are easier to store and process using standard software. As such, selection of imaging modality should be guided by the scale of analysis required and available infrastructure.

Several limitations should be considered. Donors represented a narrow age range, precluding assessment of age-associated changes in follicle density or vascular organization. Additionally, follicle and vascular metrics were quantified independently. Future studies expanding donor diversity and incorporating co-labeling of follicles and vasculature will enable

analysis of follicle-vascular relationship dynamics and strengthen the utility of this platform for mechanistic studies of ovarian tissue transplantation.

In summary, this work provides a validated framework for three-dimensional characterization of human ovarian microarchitecture. By enabling quantitative assessment of follicles and vasculature within intact volumes, this platform broadens methodological options for studying human ovarian tissue and supports future translational investigations aimed at improving fertility preservation and endocrine function restoration.

Chapter 3 Engineering the Host-Graft Interface Stabilizes Vascular Integration and Improves Endocrine Function of Transplanted Human Ovarian Tissue

3.1 Introduction

Ovarian tissue cryopreservation and transplantation (OTCT) is the only clinical strategy capable of restoring both fertility and physiological ovarian endocrine function in patients with primary ovarian insufficiency (POI) following gonadotoxic cancer treatment[14]. Despite encouraging clinical outcomes, graft function remains highly variable and limited in duration[12] due to both the inherent heterogeneity of human ovarian tissue[15] and the avascular nature of the transplantation procedure[8]. Follicle number and distribution vary widely between patients and even within a single ovary. This inter- and intra-patient heterogeneity, coupled with the lack of non-destructive methods for quantifying follicle content at the time of tissue cryopreservation and transplantation, results in a limited ability to predict ovarian graft lifespan and the likelihood of pregnancy. Furthermore, ovarian tissue lacks sufficiently large blood vessels for surgical vascular anastomosis which makes restoration of blood flow entirely dependent on post-transplantation angiogenesis[8]. Human ovarian xenograft studies have primarily characterized the early post-transplantation period, demonstrating that grafts remain hypoxic and that host-derived revascularization occurs over a 10-day window[18,19], leading to ischemic tissue injury and follicle loss. The combination of these factors leads to shortened, unpredictable graft function which poses a considerable clinical challenge given that each patient only has a finite amount of their own cryopreserved tissue available.

Accordingly, a major focus for improving ovarian graft function has been the development of strategies to support graft vascular integration following avascular tissue transplantation. Within the context of human ovarian xenograft studies, naturally derived biomaterials, including fibrin[27,31–35,67], Matrigel[29,30], and gelatin[28], have demonstrated revascularization benefits. More recently, however, granular hydrogels composed of micron-scale hydrogels ("microgels") have emerged as versatile scaffolds for improving endogenous tissue repair across a breadth of tissues[37]. Microporous annealed particle (MAP) hydrogels[38], a subclass of granular hydrogels, feature secondary crosslinks between their microgel subunits which produce a uniform, interconnected cell-scale porous network that facilitates infiltration of host cells and molecular diffusion essential to the function and survival of constituent cells[68]. The modularity of the microgel subunits enables precise control over scaffold porosity, composition, and functionality, which has proven effective in promoting vascular infiltration in vivo[39–42,69–72], making MAP hydrogels promising candidates for supporting vascular integration of transplanted ovarian tissue.

Here, we utilized a MAP hydrogel scaffold to encapsulate and transplant human ovarian tissue. Guided by clinical recommendations that emphasize high tissue surface-to-volume ratio for graft survival[73], we hypothesized that encapsulating multiple small pieces of ovarian tissue in a MAP hydrogel would support graft vascular integration and long-term function. To investigate this hypothesis, we transplanted human ovarian tissue pieces encapsulated in MAP hydrogels (OvaMAPs) into ovariectomized mice and analyzed graft revascularization, reperfusion, and restoration of ovarian endocrine function at early (3 days and 1 week) and late (3, 6, and 20 weeks) post-transplantation time points. Our findings demonstrate that MAP hydrogel encapsulation of ovarian tissue improved graft vascular integration, perfused blood vessel

formation, and hormone function compared to traditional avascular transplantation methods. To our knowledge, this study is the first to utilize MAP hydrogels as a tissue transplantation scaffold, leveraging the interconnected microporous architecture of MAP hydrogels to support functional revascularization of transplanted human ovarian tissue.

3.2 Materials and Methods

3.2.1 Microgel Formulation

Similar to the chemistry described by Dumont et al.[74], poly(ethylene glycol) (PEG) microgels were generated using a precursor solution composed of 8-arm PEG-maleimide (PEG-MAL) (40 kDa, >90% purity, JenKem Technology, USA) crosslinked with a trifunctional plasmin-sensitive crosslinking peptide (Ac-GCYK↓NSGCYK↓NSCG, MW 1525.69 g/mol, > 90% Purity, GenScript, USA, ↓ indicates the cleavage site of the peptide) (YKNS). PEG-MAL was pre-functionalized with 1 mM of integrin-binding peptide (Ac-GCGYGRGDSGP, MW 1067.10 g/mol, >85% Purity, GenScript, USA) (RGD). The final microgel precursor formulation consisted of 10 wt% PEG-MAL, 1 mM RGD, and 2.77 mM YKNS, resulting in a 16:7 stoichiometric ratio of -MAL to -SH groups between PEG and YKNS. PEG and RGD were suspended in isotonic 50 mM HEPES buffer (pH = 7.4 at 20°C) and then mixed and allowed to react for 15 minutes at 20°C. Next, hydrochloric acid (HCl, 1N, Sigma-Aldrich, USA) was thoroughly mixed into the PEG-RGD solution to lower the solution's pH to 1.5. YKNS was then dissolved in 5 mM tris-(2-carboxyethyl)phosphine (TCEP) (Pierce Premium Grade TCEP-HCl, Thermo Scientific, USA) and added to the mixture.

3.2.2 Microgel Generation

Microgels were generated using a step emulsification microfluidic device previously described by de Rutte et al[75]. A master mold (SU-8 silicon wafer with silanization) for step

emulsification microfluidic devices with wedge geometry and channel height of 11 μm was fabricated by FlowJEM (FlowJEM Inc., Canada).To prepare microfluidic devices, polydimethylsiloxane (PDMS) base was mixed with crosslinker from the PDMS Sylgard 184 kit (Dow Silicones Corporation, USA) at a 10:1 mass ratio. The mixture was then degassed, poured over the master mold, and degassed again before being left to cure overnight at 80°C. Next, the cured PDMS was peeled from the SU-8 silicon master mold, and microfluidic devices were cut from the PDMS replica cast. 1.5 mm holes were punched at the inlet and outlet ports of the PDMS microfluidic devices using a biopsy punch (Miltex Biopsy Punch, Electron Microscopy Sciences, USA). Devices and glass slides were then washed with isopropanol, followed by ethanol to remove dust. Finally, devices and glass slides were plasma etched for 1 minute and bonded.

Prior to using devices for microgel generation, devices were treated with Rain-X Glass Water Repellent (Illinois Tool Works, USA) for 1 minute and rinsed with Novec 7500 oil (3M, USA). The treated devices were then placed in an 80^{o}C oven for 1 hour. The PEG-MAL precursor solution was then injected into the microfluidic device at a flow rate of 1.2 mL/hr. The oil solution consisting of 1.5 wt% 008-FluoroSurfactant (RAN Biotechnologies, USA) in Novec 7500 oil was injected into the device at a flow rate of 2.4 mL/hr. The generated microgels were collected in a conical tube and left at room temperature overnight to complete crosslinking.

The following day, crosslinked microgels were washed to remove the oil and surfactant. First, excess oil was aspirated from the bottom of the conical tube with a syringe. Next, a solution consisting of 20 wt% 1H,1H,2H,2H-Perfluorooctanol (Thermo Scientific Chemicals, USA) in Novec 7500 oil was added to the remaining microgel solution. Then, isotonic 50 mM HEPES buffer (pH = 7.4 at 20°C) was added to the tube to swell and disperse the microgels,

while hexanes were added to lower the Novec 7500 oil density. The tube was centrifuged at 2000 × g for 5 minutes prior to removing the supernatant and the hexanes wash was repeated three more times. Next, HEPES washes were performed five times. Microgels were washed with 70% ethanol for 10 minutes. Finally, microgels were washed two more times with HEPES buffer.

3.2.3 Microgel Size Distribution

Prior to washing, crosslinked microgels in Novec 7500 oil solution were imaged with brightfield on a transmitted light microscope. After washing, microgels in HEPES buffer were imaged with the same microscope settings once a day for 6 consecutive days. The diameters of 300–400 microgels for each group were manually measured in FIJI (ImageJ) analysis software[63].

3.2.4 MAP Hydrogel Fabrication

Microgels were formulated such that unreacted maleimide groups remained available after microgel crosslinking. Annealing of microgels into a MAP hydrogel was performed on the same day as microgel washing to prevent the remaining maleimide groups from undergoing hydrolytic degradation. Washed microgels were centrifuged at 18,000 × g for 5 minutes. The supernatant was removed, and pelleted microgels were then mixed at 10% v/v with a photoinitiator solution containing 600 mg/mL of Irgacure 2959 (2-Hydroxy-4′-(2-hydroxyethoxy)-2-methylpropiophenone, Sigma-Aldrich, USA) in NVP (1-Vinyl-2-pyrrolidinone, Sigma-Aldrich, USA). Microgels were incubated for 5 minutes, followed by centrifugation at 18,000 × g for 5 minutes. The supernatant was removed, and pelleted microgels were pipetted into a cylindrical PDMS mold (4 mm diameter, 3.58 mm height) using a positive displacement pipette. Finally, microgels were exposed to ultraviolet light (λ = 365 nm, 1090 $\mu W/cm^2$) for 3 minutes to form the MAP hydrogel through photoinitiated radical polymerization of remaining maleimide functional groups.

3.2.5 MAP Hydrogel Porosity

To characterize the porosity of the MAP hydrogel, microgels were fluorescently labeled by tagging the YKNS crosslinker with a fluorophore (CF®488A Maleimide, Biotium) at a 1:600 stoichiometric ratio between -MAL in the dye and -SH in the crosslinker. Microgels and MAP hydrogels were then fabricated as described above. Multiple regions across 5 MAP hydrogels were subsequently imaged on a Leica SP8 laser scanning confocal microscope (85 μm z-stack height, 5 μm step size). Porosity, pore size, and number of pores were quantified with FIJI (ImageJ) as previously described[76,77]. Briefly, images were converted to 8-bit format, thresholded using the Otsu algorithm, and smoothed with the built-in smooth function **(Appendix Figure B.1, A**). Pores between the fluorescently labeled microgels were then analyzed with the Analyze Particles function. The analysis was limited to detect sizes ranging between 5 μm^2 and Infinity. For each z-slice, the analysis generated the total number of pores, the area of each pore, the total area occupied by pores, and the percent area occupied by pores. Only z-slices containing in-focus microgels and well-defined thresholding were included in the analysis. Raw pore areas as well as theoretical pore diameters are reported. Theoretical pore diameters were derived by treating the raw pore areas as circles. The diameters of these circles with areas corresponding to the raw pore areas were then calculated.

3.2.6 Bulk Hydrogel Fabrication

Bulk hydrogels were fabricated using a precursor solution composed of 8-arm PEG-vinyl sulfone (PEG-VS) (40 kDa, >90% purity, JenKem Technology, USA) crosslinked with YKNS. PEG-VS was pre-functionalized with 0.75 mM RGD. The final bulk hydrogel formulation consisted of 7% PEG-VS, 0.75 mM RGD, and 4.42 mM YKNS, resulting in a 1:1 stoichiometric ratio of -VS to -SH groups between PEG and YKNS. PEG and RGD were separately dissolved

in isotonic 50 mM HEPES buffer (pH=7.6 at 20°C) and then combined and left to react for 15 minutes at 20°C. YKNS was then dissolved in HEPES buffer and mixed with the PEG functionalized with RGD. The final hydrogel mixture was crosslinked for 5 minutes.

3.2.7 Hydrogel Mesh Size

The mesh size of MAP and bulk hydrogel formulations was theoretically estimated following a previously described method[78]. Briefly, two types of bulk hydrogels were prepared: (1) PEG-MAL bulk hydrogel matching the MAP hydrogel formulation and (2) PEG-VS bulk hydrogel. PEG-MAL bulk hydrogels (50 µL) were left to crosslink overnight at 20°C in a humidity chamber, while PEG-VS bulk hydrogels (50 µL) were left to crosslink for 5 minutes at 20°C. After crosslinking, hydrogels were submerged in Milli-Q water and allowed to swell overnight at 37°C. The weight of the swollen hydrogels was then recorded. Next, hydrogels were lyophilized, and dry weights were recorded. Both swollen and dry hydrogel weights were subsequently used to calculate the mass swelling ratio with the following equation:

$$Q_m = \frac{swollen\ weight}{dry\ weight}$$

where Q_m is the mass swelling ratio. Volumetric swelling ratio (Q_v) was then calculated using the following equation:

$$Q_v = 1 + \left(\frac{\rho_p}{\rho_s} \times (Q_m - 1)\right)$$

where ρ_p is the polymer density and ρ_s is the solvent density. Next, average molecular weight between crosslinks ($\bar{M}_c$) was calculated as described below:

$$\frac{1}{\bar{M}_c} = \frac{2}{\bar{M}_n} - \frac{\frac{\bar{v}}{V_1}(\ln(1 - v_2) + v_2 + \chi_1 v_2^2)}{v_2^{1/3} - \frac{v_2}{2}}$$

where $\bar{M}_n$ is the number average molecular weight of polymer chains in the absence of crosslinker, v is the specific volume of the polymer, V_1 is the molar volume of the solvent, v_2 is the volume fraction of the polymer in the swollen state which is equivalent to the reciprocal of Q_v, and χ_1 is the polymer-solvent interaction parameter. The values for defined parameters are shown in **Table 3.1**. $\bar{M}_c$ was then used to find the root mean square end-to-end distance of the polymer chain ($\sqrt{\bar{r}_0^2}$) which can be described by:

$$\sqrt{\bar{r}_0^2} = l\sqrt{C_n N}$$

where l is the average bond length between C-C and C-O bonds in the repeat unit of PEG ([-O-CH_2-CH_2-]), C_n is the Flory characteristic ratio for PEG, and N is the number of links between monomers in the polymer chain. N can be further defined with $\bar{M}_c$ using the following equation:

$$\mathrm{N} = 2\frac{\bar{M}_c}{M_r}$$

where M_r is the molecular mass of the PEG repeating unit. Finally, mesh size (ξ) was calculated as shown below.

$$\xi = Q_v^{1/3}\sqrt{\bar{r}_0^2}$$

Table 3.1 Parameters for Hydrogel Mesh Size Calculations

Parameter	Description	Value
ρ_p	Polymer density	1 g/cm^3
ρ_s	Solvent (water) density	1 g/cm^3
$\bar{M}_n$	Number average molecular weight of polymer chains in the absence of crosslinker	10,000 g/mol
$\bar{v}$	Specific volume of polymer	1 g/cm^3
V_1	Molar volume of solvent (water)	18 cm^3/mol
χ_1	Polymer-solvent interaction parameter	0.426 [79]
l	Average bond length between C-C and C-O bonds in the repeat unit of PEG	1.46 nm [80]
C_n	Flory characteristic ratio for PEG	4 [80]
M_r	Molecular mass of PEG repeating unit	44 g/mol [80]

3.2.8 Hydrogel Diffusion

The diffusion of fluorescently labeled molecules through MAP and bulk hydrogels was assessed by analyzing the amount of molecule passing through the hydrogels. This was achieved using a framework composed of a cell culture insert and a 3D-printed tube (**Appendix Figure B.1, C**). Preparation of hydrogel samples differed between the MAP and bulk hydrogel groups due to the malleable nature of MAP hydrogels. A MAP hydrogel sheet was prepared by annealing microgels in a square PDMS mold (10 × 10 mm in width and length, 2.7 mm in height). Next, a 3D-printed square tube (7.35 × 7.35 mm in width and height, 150 mm in height) was used to cut out the prepared MAP hydrogel in the shape of the tube and the MAP hydrogel-tube construct was transferred to a cell culture insert (cellQART 12-Well Cell Culture Insert, PET, 8.0 μm, Sterlitech, USA). In contrast, bulk hydrogel precursor solution was directly crosslinked inside the 3D-printed tube prior to being transferred to a cell culture insert. 3D-printed tubes were secured within cell culture inserts using a PDMS ring (12 mm outer diameter, 10 mm inner diameter) placed around each 3D-printed tube. The cell culture inserts were then placed in a 12-well plate containing 2 mL of DPBS per well and were left overnight at 37°C to allow hydrogels to swell and equilibrate.

The following day, the cell culture inserts were transferred to a fresh 12-well plate containing 1.6 mL of DPBS per well. Cell culture inserts containing empty 3D-printed tubes were used as controls. A solution containing a fluorescent molecule (2 μM) (**Table 3.2**) was then pipetted into the 3D-printed tubes (t_0). At specific time points, 100 μL of solution from the well beneath the cell culture insert was aspirated and collected in a 96-well black plate (Non-Treated Coverglass Surface, Thermo Scientific. USA) for analysis. Subsequently, the cell culture inserts

were transferred to a fresh well within the 12-well plate. The 12-well plates were maintained at 37°C when solution samples were not being collected.

Fluorescence intensities of all collected samples were measured after 6 and 96 hours using a plate reader (Synergy H1 Multi-Mode Microplate Reader, BioTek). The concentration of fluorescently labeled molecules in the collected samples was calculated using the measured fluorescence intensity and standard curves relating known concentrations to measured fluorescence intensities. Concentrations of fluorescent molecules in the collected samples were then converted to the amount of fluorescent molecules, which was subsequently used to calculate the cumulative diffusion of molecules over time. These values were then converted to percent molecule diffused over time using the amount of molecule contained in the original fluorescent molecule solution pipetted into the 3D-printed tubes at t_0. Finally, these percentage values for each fluorescent molecule were normalized to the terminal percent molecule diffused in the control condition.

Table 3.2 Molecules Used for Hydrogel Diffusion Assay

Molecule Type	Molecular Weight (kDa)	Conjugation	Product
Dextran	4	Fluorescein isothiocyanate	FD4, Sigma Aldrich, USA
Dextran	40	Fluorescein isothiocyanate	FD40S, Sigma Aldrich, USA
Bovine serum albumin	66	Alexa Fluor™ 488	A13100, Invitrogen, USA

3.2.9 Rheological Characterization

Rheological characterization of MAP and bulk hydrogels (**Appendix Figure B.2**) was performed using a TA Instruments HR30 Rheometer. Sandpaper was affixed to the bottom plate and hydrogel samples (8 mm discs) were subsequently loaded onto the instrument. An amplitude sweep was conducted at a constant angular frequency of 10 rad/s over a strain range of 0.01-

100% to determine the linear viscoelastic region (LVR). Based on the identified LVR, frequency sweeps were performed from 0.1 to 100 rad/s at a constant strain of 0.1% for MAP hydrogels and 1% for bulk hydrogels.

3.2.10 Ethical Approval for the Procurement of Human Ovaries

As previously described[56,60], whole human ovaries were obtained from deceased donors for non-clinical research through the International Institute for the Advancement of Medicine (IIAM) and associated Organ Procurement Organizations (OPOs). IIAM and the associated OPOs comply with state Uniform Anatomical Gift Acts (UAGA) and are certified and regulated by the Centers for Medicare and Medicaid Services (CMS). These OPOs are members of the Organ Procurement and Transplantation Network (OPTN) and the United Network for Organ Sharing (UNOS) and operate under standards established by the Association of Organ Procurement Organizations (AOPO) and UNOS. Informed, written consent was obtained from the deceased donors' families prior to tissue procurement for the tissue used in this study. A biomaterial transfer agreement is in place between IIAM and the University of Michigan that restricts the use of the tissue to pre-clinical research not involving the fertilization of gametes. The use of deceased donor ovarian tissue in this research is categorized as "not regulated" per 45 CFR 46.102 and the "Common Rule" as it does not involve human subjects and therefore complies with the University of Michigan Institutional Review Board (IRB) requirements.

3.2.11 Human Ovarian Tissue Collection

Upon arrival in the laboratory, donor ovaries were transferred to pre-cooled holding media composed of Quinn's Advantage Medium with HEPES (QAMH, ART-1024, CooperSurgical, USA) supplemented with 10% Quinn's Advantage Serum Protein Substitute (SPS, ART-3010, CooperSurgical, USA). The outer cortex layer was collected from the ovaries

using a custom cutting guide (Reprolife, Japan), which produced cortical tissue squares measuring approximately 1 mm in thickness and 10 mm in both length and width. At this stage, a subset of cortex samples was fixed in Bouin's fixative (Ricca Chemical, USA). The remaining fresh cortical squares were cryopreserved using a previously published slow freezing protocol[56,60,61]. Briefly, tissue squares were placed into cryovials containing pre-cooled cryoprotectant media composed of 10% SPS, 0.75 M dimethyl sulfoxide (DMSO, D2650, Sigma-Aldrich, USA), 0.75 M ethylene glycol (102466, Sigma-Aldrich, USA), and 0.1 M sucrose (S1888, Sigma-Aldrich, USA) in QAMH. Following equilibration at 4°C for 30 minutes, cryovials were slowly cooled from 4°C to -9°C at a rate of -2°C /min, manually seeded, held at -9°C for 4 minutes, and then slowly cooled to -40°C at a rate of -0.3°C/min. Finally, cryovials were submerged in liquid nitrogen and stored in a cryogenic storage dewar until further use.

3.2.12 Human Ovarian Tissue Characterization

The human ovarian tissue used in this study was obtained from two deceased donors (donors A and B). Both donors were of reproductive age (A: 29 years old; B: 20 years old) and did not have a medical history indicative of conditions that would affect ovarian function.

Donor follicle density was assessed throughout the ovarian cortex using the fresh tissue fixed in Bouin's fixative at the time of tissue collection. Samples were fixed at 4ºC overnight and then washed in dH_2O for 1 hour, 50% ethanol for 1 hour, 70% ethanol for 1 hour, and finally stored in 70% EtOH at 4ºC. Fixed samples were then embedded in paraffin at the University of Michigan Dental School Histology Core and serially sectioned at a thickness of 5 µm, producing four sections per slide for up to 50 slides per tissue sample. Every other slide was subsequently stained with hematoxylin and eosin (H&E) and imaged using a digital slide scanner (Leica Aperio AT2, Leica Biosystems, Germany) set to 20× magnification (**Appendix Figure B.3, A**)

at the University of Michigan Unit for Laboratory Animal Medicine Pathology Core. Whole slide scans were imported into QuPath analysis software (v0.2.2) for manual follicle counting as described by Machlin et al[64].

Briefly, every 8th tissue section was analyzed for follicles with a total of 24 sections analyzed for donor A and 10 sections analyzed for donor B. Analysis of every 8th tissue section corresponded to a sampling spacing of 40 μm which prevented duplicate counts of primordial, transitional primordial, or primary follicles. As such, every primordial, transitional primordial, and primary follicle was counted for each analyzed tissue section. Larger follicles were only counted where the nucleus was visible to prevent duplicate counts.

To calculate follicle density, tissue area was measured for all 24 and 10 sections for donors A and B, respectively, using FIJI (ImageJ). Tissue volume was then calculated by multiplying tissue section area by a tissue thickness of 20 μm rather than 40 μm to account for smaller primordial follicles that could have been omitted in between every 8th tissue section that was analyzed. Follicle density for each analyzed tissue section was subsequently calculated as the total number of follicles in the tissue section divided by the tissue section volume. The calculated follicle densities for donors A and B were 48.05 ± 73.07 follicles/mm^3 and 642.9 ± 95.28 follicles/mm^3, respectively (**Appendix Figure B.3, B**).

3.2.13 Human Ovarian Tissue Thawing

Cortex squares were thawed following a previously described protocol[60,61]. Briefly, cryovials containing cortex were removed from liquid nitrogen and left at room temperature for 30 seconds before being immersed in a 37°C water bath. Once the cryoprotectant medium had thawed (after approximately 1.5 minutes), the tissue was removed from the vial and placed into the first thawing solution (QAMH with 10% SPS, 0.5 M DMSO, 0.5 M ethylene glycol, 0.1 M

sucrose) for ten minutes. The tissue was then sequentially incubated in solutions with decreasing concentrations of cryoprotectants: the second thawing solution (QAMH with 10% SPS, 0.25 M DMSO, 0.25 M ethylene glycol, 0.1 M sucrose), the third thawing solution (QAMH with 10% SPS, 0.1 M sucrose), and the fourth thawing solution (QAMH with 10% SPS) for ten minutes each. The fourth thawing solution served as a maintenance solution. All four solutions were equilibrated to room temperature for the thawing procedure.

3.2.14 Human Ovarian Tissue Preparation for Implantation

To prepare non-encapsulated tissue for implantation, thawed cortex squares were manually cut into strips measuring approximately 1 mm in width and 5 mm in length. Similarly, to prepare tissue for encapsulation in bulk and MAP hydrogels, thawed cortex squares were manually cut into cubes measuring approximately 1 mm in length and width, thereby increasing the tissue surface-to-volume ratio by approximately 30%. All manual cutting was performed with tissues being maintained in the fourth thawing solution.

3.2.15 Human Ovarian Tissue Encapsulation in Hydrogels

MAP and bulk hydrogels were prepared with 4 tissue cubes per hydrogel. To encapsulate the tissue cubes in MAP hydrogels, 25 μL of the pelleted microgel/photoinitiator mixture was pipetted into a cylindrical PDMS mold (4 mm diameter, 3.58 mm height). The 4 tissue cubes were then placed on top of the pipetted microgels and covered with an additional 20 μL of microgels. Finally, the construct was exposed to ultraviolet light (λ = 365 nm, 1090 μW/cm^2) for 3 minutes to produce human ovarian tissue cubes encapsulated in a MAP hydrogel (OvaMAP). To encapsulate the tissue in bulk hydrogels, 4 tissue cubes were placed in the cylindrical PDMS mold. Then, 45 μL of bulk hydrogel precursor solution was pipetted into the mold and allowed to crosslink for 5 minutes.

3.2.16 Ovariectomy and Intraperitoneal Implantation

All animal procedures in this work were performed in accordance with the protocol approved by the Institutional Animal Care and Use Committee (IACUC) at the University of Michigan (PRO00011284). First, a bilateral ovariectomy was performed on 10–11-week-old NOD.Cg-*rkdc*^{scid} *Il2rg*^{tm1Wjl}/SzJ (NSG) female mice (RRID:IMSR_JAX:005557, The Jackson Laboratory) to model primary ovarian insufficiency. Mice were anesthetized with isoflurane (2–3%) via inhalation and were then administered preemptive analgesics (Carprofen, RIMADYL, Zoetis, USA, 5 mg/kg body weight) via subcutaneous injection. A longitudinal midline incision was then made in the abdominal wall using aseptic techniques and procedures. The intraperitoneal space was exposed, and the ovaries were removed by cauterizing the uterine horns directly below the ovary and cutting off the ovaries with microscissors. Next, the parametrial fat pads were exposed one at a time. One tissue strip or hydrogel (bulk or MAP with tissue cubes) was implanted in the fat pad by folding the fat around the tissue strip or hydrogel and sealing the fat pouch with absorbable 8-0 sutures. As such, each mouse was implanted with either two tissue strips or two hydrogels (bulk or MAP). The fat pads containing tissue strips or hydrogels were then returned to the intraperitoneal cavity and the incisions were closed in two layers (abdominal muscles and skin) using absorbable 5-0 sutures and aseptic techniques and procedures. Mice were placed in a clean cage to recover and were given analgesics 24 hours after the initial preemptive analgesic was administered. Mice were monitored postoperatively for 7–10 days and administered additional analgesics as needed.

3.2.17 Implant Removal

Implants were removed at the terminal time points of 3 days or 1, 3, 6, or 20 weeks. Mice were anesthetized as described above. A longitudinal midline incision was made in the

abdominal wall, and the fat pads containing the tissue strips or hydrogels were excised and placed in 4% paraformaldehyde. Implants were left to fix overnight at 4°C before washing three times in DPBS for 1 hour each and then storing in 70% ethanol at 4°C.

3.2.18 Human and Mouse Vasculature Visualization

We utilized tissue clearing techniques rather than conventional sectioning methods, which typically offer a limited view of samples and risk tearing hydrogel samples. Tissue clearing allowed us to analyze the implants and provided a comprehensive visualization of the interactions between the implants and the surrounding tissues of the host. However, due to variability in the amount of fat enveloping implants, implants were first sectioned to a consistent thickness of 800 μm using a vibratome (VF-310-0Z, Precisionary Instruments, USA). Next, a CUBIC tissue clearing protocol previously described by Matsumoto et al.[62] was adapted to clear the implant sections. The protocol consists of three distinct phases: (1) delipidation, (2) staining, and (3) refractive index (RI) matching **(Table 3.3)**. Briefly, delipidation of the implant sections was initiated by immersing the sections in an equivalent volume mixture of dH_2O and CUBIC-L (10% (wt/wt) N-butyldiethanolamine (B0725, TCI America, USA), 10% (wt/wt) Triton X-100 (X100, Sigma-Aldrich, USA), 80% (wt/wt) dH_2O) with shaking at 37°C overnight. The next day, this mixture was replaced with fresh CUBIC-L. CUBIC-L was refreshed every 48 hours for a total CUBIC-L incubation duration of 10 days. At the end of 10 days, to stop the delipidation process, sections were washed with 1X phosphate-buffered saline (PBS) with shaking at room temperature for at least 2 hours. This washing step was repeated more than three times.

Next, of the sections that were cleared, one section from the center of each implant was selected for immunofluorescence staining. To stain the implants, sections were blocked with 5% normal goat serum (ab138478, Abcam, USA) in 1X PBS with shaking at 37°C overnight.

Sections were then incubated in a solution consisting of a mouse-specific vasculature primary antibody (CD31, 1:150, #77699, Cell Signaling Technology, USA) diluted in blocking solution with shaking at 37°C for 3 days. Following this step, sections were washed in blocking solution three times with shaking at room temperature for 1 hour each. Next, sections were incubated in a solution containing a human-specific vasculature marker, Ulex europaeus agglutinin 1 (UEA-1, DyLight 649, 1:250, DL-1068-1, Vector Laboratories, USA), secondary antibody (Goat anti-Rabbit, Alexa Fluor 555, 1:1000, A21428, Invitrogen, USA) and nuclear counterstain (DAPI, 1:1000, D1306, Invitrogen, USA) diluted in blocking solution with shaking at 37°C for 3 days. Finally, the samples were washed in 1X PBS three times with shaking at room temperature for 1 hour each before proceeding to the RI matching phase.

To perform RI matching, sections were immersed in an equivalent volume mixture of dH_2O and CUBIC-R+(M) (45% (wt/wt) antipyrine (D1876, TCI America, USA), 30% (wt/wt) N-methyl-nicotinamide (M0374, TCI America, USA), 0.5% (vol/vol) N-butyldiethanolamine, 24.5% (wt/wt) dH_2O) with shaking at room temperature overnight. Next, this mixture was replaced with fresh CUBIC-R+(M) and sections were incubated with shaking at room temperature overnight. The next day, CUBIC-R+(M) was refreshed and sections were incubated for an additional day. After this final CUBIC-R+(M) incubation step, implant sections were ready for imaging.

Finally, sections were imaged on a Leica SP8 laser scanning confocal microscope. Tilescans composed of Z-stacks of 500 μm with a z-step of 2.5 μm were acquired for each implant section. Laser power and gain were maintained across all implant sections.

Table 3.3 CUBIC Clearing and Staining Protocol Timeline

Phase	Day	Step
Delipidation	1	1/2 CUBIC-L
	2	CUBIC-L
	3	
	4	Refresh CUBIC-L
	5	
	6	Refresh CUBIC-L
	7	
	8	Refresh CUBIC-L
	9	
	10	Refresh CUBIC-L
	11	
Staining	12	Wash + Block
	13	CD31
	14	
	15	
	16	Wash + UEA/Secondary/DAPI
	17	
	18	
RI matching	19	Wash + 1/2 CUBIC-R+
	20	CUBIC-R+
	21	Refresh CUBIC-R+
	22	
	23	Image or store are room temperature

3.2.19 Human and Mouse Vasculature Quantification

The percent area positive for human UEA-1 and mouse CD31 within human ovarian tissue was measured in 36 implants (12 non-encapsulated tissue strips, 12 OvaMAPs, 12 bulk hydrogels). For each implant, one 800 μm-thick vibratome section was imaged to produce a 500 μm-tall confocal image containing 200 z-slices. Ultimately, 20 z-slices were analyzed for each implant using FIJI (ImageJ) in order to quantify human and mouse vasculature within human ovarian tissue.

To obtain the percent area measurements, the unaltered confocal image for each of the 36 implants was first converted from Leica's LIF file format into BigTIFF file format using the FIJI Bio-Formats plugin. The BigTIFF image was then trimmed from a 200 z-slice image to a 100 z-slice image by generating a substack containing every other z-slice. This 100 z-slice substack was then divided into five substacks containing 20 z-slices each. From these five substacks, one

representative substack was selected for analysis. For the selected substack, regions of interest (ROIs) were then outlined on each z-slice around either the non-encapsulated tissue strip or the hydrogel-encapsulated tissue cubes.

The ensuing steps were performed for the human UEA-1 and mouse CD31 channels separately. To subtract background signal, mean gray value was measured in one 50 × 50 μm high background signal ROI for each z-slice within the substack. The mean value of these 20 measurements was then subtracted from each z-slice within the substack. Next, all 20 z-slices were smoothed with the built-in smooth function and thresholded using the Moments algorithm. The percent area positive for either human UEA-1 or mouse CD31 was then obtained for each z-slice using the Analyze Particle function. The analysis was constrained to the previously outlined ROIs. Additionally, the analysis was limited to detect sizes ranging between 19.635 μm^2 and Infinity. The lower limit of 19.635 μm^2 was applied assuming a minimum vessel diameter of 5 μm. For each z-slice, the Analyze Particles function output the percent area positive for human UEA-1 or mouse CD31. Finally, for each implant, the reported percent area positive for human UEA-1 or mouse CD31 corresponded to the mean value of the 20 analyzed z-slices.

The characterization of mouse CD31 vasculature through quantification of vessel length density and mean branch length was performed using the Quantitative Vascular Analysis Tool (Q-VAT) macro[81] for FIJI. Only non-encapsulated tissue strip and OvaMAP confocal images were subjected to this quantification since the previous percent area measurements revealed no infiltration of mouse CD31 vasculature within the bulk hydrogel implants. To perform the analysis, Q-VAT requires two-dimensional images. As such, the same substacks used for the previous percent area measurements were utilized to generate maximum intensity projections. However, because of graft geometry variations along the 20-slice depth, only the first 10 or last

10 z-slices were used to generate maximum intensity projections, ensuring that accurate ROIs delineating only human ovarian tissue could be generated. No background subtraction was performed on these z-slices. The maximum intensity projections were then processed using the Q-VAT masking and analysis tools using the parameter inputs listed in **Table 3.4**. ROIs were outlined around either the non-encapsulated tissue strip or the encapsulated tissue cubes to restrict the Q-VAT masking and analysis to the grafts rather than the surrounding mouse tissue.

Table 3.4 Q-VAT Input Parameters

Parameter	**Input**
Calibration (μm/pixel)	1.136
Radius of biggest object (μm)	40
Particle size lower range (μm^2)	10000
Radius for median filtering (μm)	2
Remove small particles (μm^2)	10
Thresholding method	Otsu
Vascular compartment separation threshold (μm)	10
Close labels radius (μm)	10
Prune ends threshold (μm)	5

3.2.20 Functional Mouse Vasculature Visualization

Visualization of functional mouse vasculature infiltrating OvaMAPs was achieved by staining for a mouse-specific red blood cell marker. OvaMAPs were sectioned at a thickness of 400 μm using a vibratome. Next, sections were incubated in a permeabilization solution composed of 0.2% Triton X-100 (Sigma-Aldrich, USA) in 1X PBS with shaking at 37°C overnight. The following day, sections were blocked with 5% normal goat serum in 1X PBS with shaking at 37°C overnight. Then, sections were incubated in a solution containing a mouse-specific red blood cell primary antibody (TER-119, 1:200, 14-5921-85, Invitrogen, USA) diluted in blocking solution with shaking at 37°C for 3 days. Following this step, sections were washed

in blocking solution three times with shaking at room temperature for 1 hour each. Next, sections were incubated in a solution containing secondary antibody (Goat anti-Rat, Alexa Fluor Plus 647, 1:1000, A48265, Invitrogen, USA) and nuclear counterstain (DAPI, 1:1000, D1306, Invitrogen, USA) diluted in blocking solution with shaking at 37°C for 3 days. Sections were then washed in 1X PBS three times with shaking at room temperature for 1 hour each. In order to mount the sections for imaging, the sections were then subjected to the RI matching steps used in the CUBIC clearing protocol. Finally, sections were imaged on a Leica SP8 laser scanning confocal microscope.

3.2.21 Serum Hormone Analysis

At the terminal time points of 3 days and 1, 3, 6, and 20 weeks, blood was collected via cardiac puncture. Following blood collection, blood samples were stored at 4°C overnight and then centrifuged at 2,000 × g for 15 minutes. Blood serum was collected and stored at -80°C until analysis. Serum samples were analyzed at the Ligand Assay and Analysis Core of the Center for Research in Reproduction at the University of Virginia. Estradiol and follicle-stimulating hormone were measured as complementary indicators of graft endocrine function, with estradiol reflecting ovarian tissue hormone production and follicle-stimulating hormone serving as a marker of hypothalamic-pituitary-ovarian feedback regulation. Estradiol was analyzed using ELISA (Estradiol – Mouse and Rat Serum, Plasma & Tissue Homogenates, American Laboratory Products Co., USA) with a lower detection limit of 5 pg/mL. Progesterone was analyzed using ELISA (Progesterone – Mouse and Rat Serum, Plasma & Tissue Homogenates, Immuno-Biological Laboratories, USA) with a lower detection limit of 0.15 ng/mL. Follicle-stimulating hormone was analyzed using an in-house ELISA protocol with a lower detection limit of 0.016 ng/mL.

3.2.22 Statistical Analysis

All statistical analysis was performed in GraphPad Prism 10. Unless otherwise noted, data is expressed as mean ± standard deviation (mean ± SD). Error bars throughout figures are mean ± standard deviation per group. Data in Figures 1 and 3 were analyzed by one-way ANOVA with Tukey's multiple comparisons test, $p < 0.05$, different letters indicate statistical significance. Data in Figures 2 and 4 were analyzed by two-way ANOVA with Šidák's multiple comparisons test, $p < 0.05$, significant difference indicated as $*p \leq 0.05$, $**p \leq 0.01$, $***p \leq 0.001$, $****p \leq 0.0001$. Data in Figure 6 was analyzed by Kruskal-Wallis test with Dunn's multiple comparisons test, $p < 0.05$, significant differences indicated as $*p \leq 0.05$, $**p \leq 0.01$, $***p \leq 0.001$.

3.3 Results

3.3.1 Non-encapsulated Ovarian Tissue Exhibits Transient Revascularization

To establish a baseline control reflecting the current clinical avascular transplantation practice, we first investigated revascularization of non-encapsulated human ovarian grafts transplanted into immunodeficient ovariectomized mouse hosts. Ovarian cortex from donated human ovaries was processed into 10 × 10 × 1 mm (length × width × height) squares and then cryopreserved using a slow freezing protocol (**Figure 3.1, A**). To prepare the tissue for transplantation, ovarian cortex squares were thawed, cut into approximately 20 strips (5 × 1 × 1 mm each), and then implanted into the parametrial fat pads of ovariectomized NOD.Cg-*rkdc*^{scid} *Il2rg*^{tm1Wjl}/SzJ (NSG) female mice.

Transplanted tissue strips were explanted at 3 days and 1, 3, and 6 weeks to investigate the temporal dynamics of non-encapsulated graft revascularization. The explants were first optically cleared to facilitate downstream imaging and then stained with species-specific

vascular markers. Mouse vasculature was labeled with a mouse-specific CD31 antibody, and human vasculature was labeled with Ulex europaeus agglutinin 1 (UEA-1) (**Figure 3.1, B**). Confocal imaging revealed mouse vasculature infiltration in the human ovarian grafts as early as 3 days post-transplantation, which increased 17-fold by 1 week (**Figure 3.1, C**). By 3 weeks, however, mouse $CD31^+$ area within the grafts decreased significantly, dropping to less than half of the percent area observed at 1 week. Subsequently, mouse vasculature within the grafts further declined by 6 weeks, returning to the baseline percent area observed at the initial 3-day time point. Total mouse vessel length per ovarian graft area demonstrated a similar temporal pattern, with a transient peak at 1 week followed by decreases at 3 and 6 weeks (**Figure 3.1, D**). In contrast, the mean branch length of mouse vessels within the ovarian grafts remained similar at all time points (**Figure 3.1, E**), suggesting that the observed changes in mouse vasculature area within the grafts over time were likely driven by variations in the number of infiltrating vessels rather than by the branch length of existing vessels.

Native human vasculature within the grafts remained stable during the first week but decreased significantly at 3 and 6 weeks (**Figure 3.1, F**). Positive UEA-1 staining and UEA-1^+/$CD31^+$ chimeric vessels in the mouse tissues surrounding the grafts after 3 and 6 weeks post-transplantation indicated outgrowth and infiltration of human endothelial cells (ECs) into the host mouse fat pads (**Figure 3.1**, **B, insets**). Collectively, these results suggested that the host-graft interface supported only transient mouse vascular infiltration and did not provide an environment conducive to stable, long-term host-derived graft revascularization.

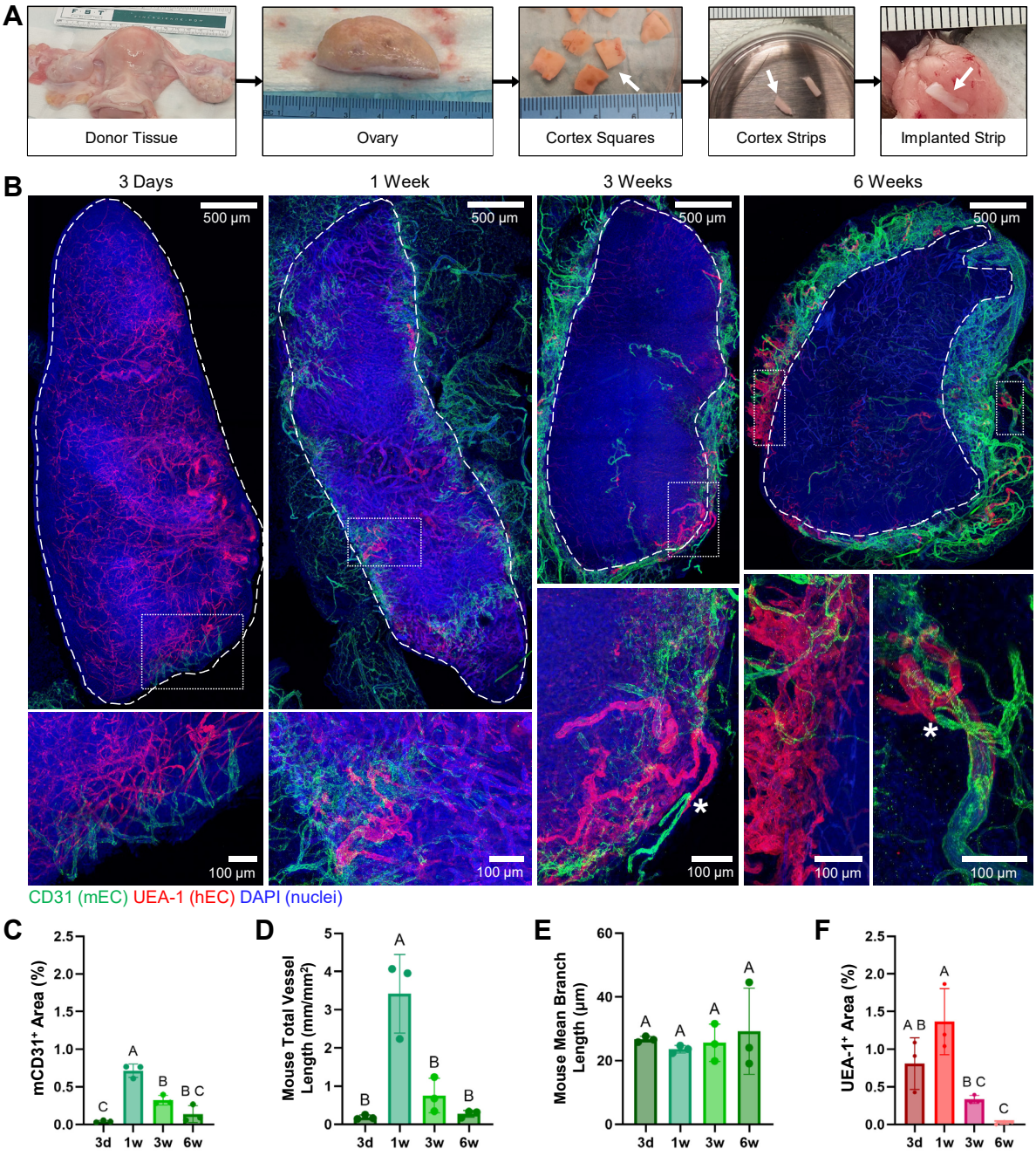


Figure 3.1 Revascularization of Non-Encapsulated Human Ovarian Tissue Grafts. (A) Human ovarian donor tissue processing into cortex squares prior to cryopreservation. Upon thawing, ovarian cortex squares were cut into strips and implanted into the parametrial fat pads of immune deficient, ovariectomized mice. Arrows mark the human ovarian tissue. **(B)** Representative maximum intensity projection images show post-implantation mouse (CD31, green) and human (UEA-1, red) vasculature dynamics in human ovarian tissue strips over the course of 6 weeks. Dashed white lines delineate the border of the implanted human tissue within the surrounding mouse fat pad. Asterisks indicate chimeric (UEA-1^{+}/CD31^{+}) vasculature. **(C)** Percent area of implanted human ovarian tissue strip that stained positively for mouse vasculature. **(D)** Mouse total vessel length per tissue strip area. **(E)** Mouse mean branch length within tissue strip. **(F)** Percent area of implanted human ovarian tissue strip that stained positively for human vasculature. Data points represent individual grafts from distinct mouse hosts (n = 3 per time point). Data

analyzed by one-way ANOVA with Tukey's multiple comparisons test, $p < 0.05$, different letters indicate statistical significance.

3.3.2 Development of a MAP Hydrogel for Ovarian Tissue Encapsulation and Transplantation

The transient revascularization observed in non-encapsulated grafts prompted the development of a materials-based strategy to modulate the host-graft interface. Specifically, we leveraged the microporous network of MAP hydrogels to generate a host-graft interface conducive to sustained graft revascularization. Poly(ethylene glycol) (PEG) MAP hydrogels were formed with a plasmin-cleavable peptide, YKNS, to tailor scaffold degradation to ovarian tissue – which undergoes remodeling primarily via the plasminogen/plasmin pathway throughout the cycles of follicle development[82] – and functionalized with the integrin-binding peptide RGD (**Figure 3.2, A**). This formulation was used to generate microgels in a step emulsification microfluidic device. Once swollen and equilibrated, microgels measured 90 ± 5 μm (mean ± SD) in diameter.

When formulating the microgels, a subset of MAL functional groups were intentionally left unreacted. These residual MAL groups enabled subsequent annealing of microgels into the MAP hydrogel via ultraviolet light photoinitiated radical polymerization (**Figure 3.2, B**) and rendered individual microgels as well as the assembled MAP hydrogel semi-degradable. To assess MAP hydrogel porosity, microgels were labeled with a fluorophore and imaged by confocal microscopy (**Figure 3.2, B**). Analysis of confocal images (**Appendix Figure B.1, A**) revealed a median pore area of 125 μm^2 (IQR: 52–530 μm^2) (**Figure 3.2, C**). By treating these pore areas as circles, the assembled MAP hydrogel was found to have a median pore diameter of 12 μm (IQR: 8–26 μm), confirming the formation of micron-scale void spaces suitable for

cellular infiltration. In contrast, bulk hydrogels formed using the same formulation had a mesh size of 131 ± 0.4 nm (mean ± SD), confirming nanoscale porosity (**Appendix Figure B.1, B**).

Next, mass transport through the MAP hydrogel's porous network was examined by utilizing fluorescently tagged molecules and in vitro diffusion assays (**Appendix Figure B.1, C**). Specifically, we selected Alexa Fluor 488-conjugated bovine serum albumin (BSA) as a representative globular protein as well as FITC-conjugated dextran (DEX) of various molecular weights. Transwell inserts were used to assess the diffusion of these molecules across MAP and bulk hydrogels. Over a period of 96 hours, all tested molecules (66 kDa BSA, 4 kDa DEX, 40 kDa DEX) exhibited significantly greater diffusion through the MAP hydrogel compared to the bulk hydrogel (**Appendix Figure B.1, D–F**). After 6 hours, close to half of the solutes had already diffused through the MAP hydrogel. The cumulative diffusion through MAP hydrogels was 193 times greater for 4 kDa DEX, 633 times greater for 40 kDa DEX, and 282 times greater for BSA compared to bulk hydrogels after 6 hours (**Figure 3.2, D**). Moreover, after 96 hours, most of the solutes had diffused through the MAP hydrogels. Accordingly, the cumulative diffusion through MAP hydrogels was 1.7 times greater for 4 kDa DEX, 25 times greater for 40 kDa DEX, and 21 times greater for BSA compared to bulk hydrogels after 96 hours.

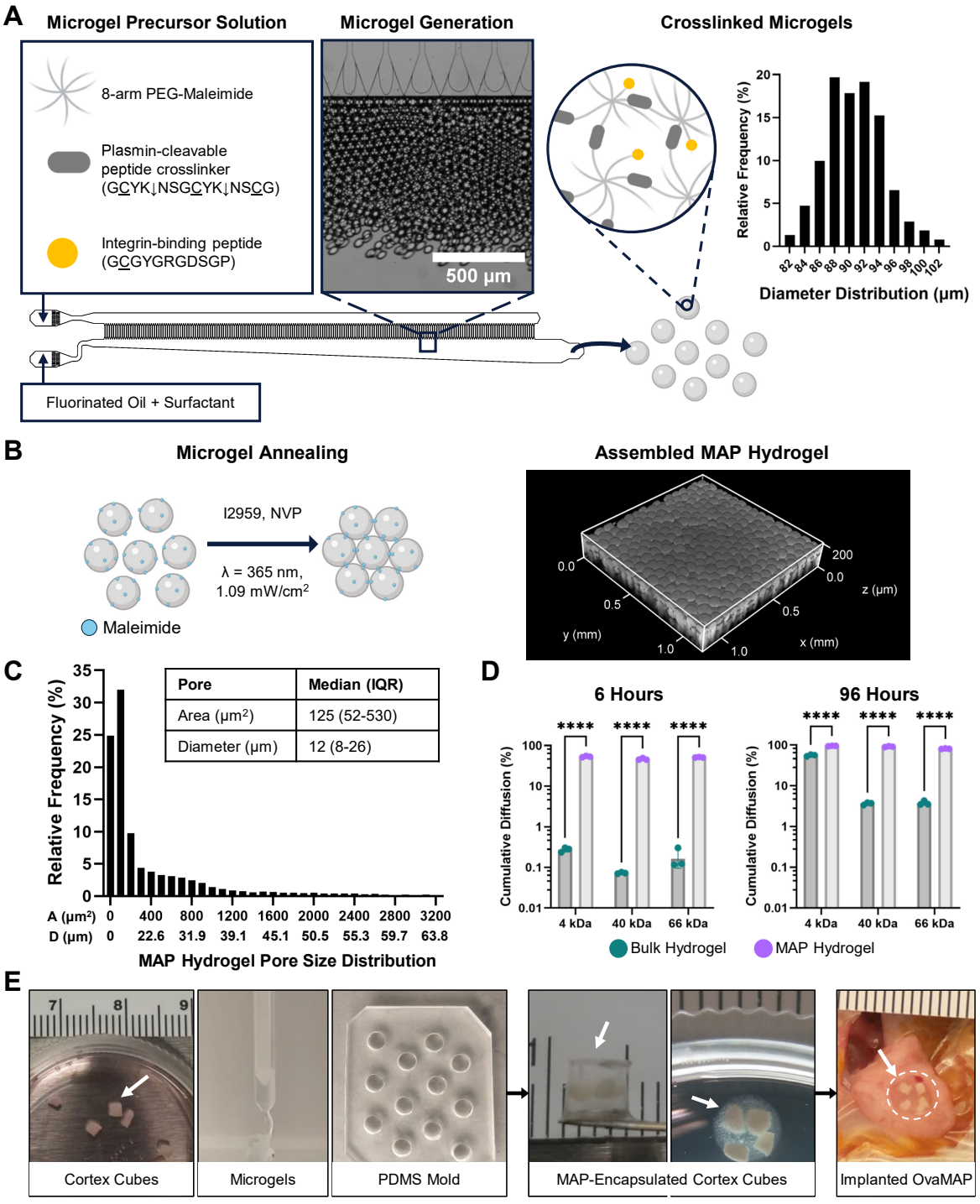


Figure 3.2 MAP Hydrogel Fabrication and Characterization. (A) Microfluidic fabrication of PEG microgels and diameter distribution of crosslinked microgels. **(B)** Microgels were annealed through photopolymerization of remaining maleimide groups, producing an assembled MAP hydrogel shown in the representative 3D rendering. **(C)** MAP hydrogel pore area distribution was measured using confocal images of assembled MAP hydrogels (n = 5 MAP hydrogels). Pore diameter distribution was estimated by treating pore areas as corresponding to areas of circles. **(D)** In vitro cumulative diffusion of 4 kDa and 40 kDa FITC-DEX and 66 kDa Alexa Fluor 488-conjugated BSA through bulk (n = 3) and MAP (n = 3) hydrogels after 6 hours and 96 hours, demonstrating greater molecular transport through MAP hydrogels. Each data point represents one hydrogel. Data analyzed by two-way ANOVA

with Šidák's multiple comparisons test, $p < 0.05$, significant difference indicated as ****$p \leq 0.0001$. **(E)** Encapsulation of human ovarian cortex cubes within MAP hydrogels and implantation of OvaMAP into the mouse parametrial fat pad. Arrows mark the ovarian tissue and OvaMAP.

3.3.3 MAP Hydrogels Stabilize Human Ovarian Graft Revascularization

Next, we encapsulated multiple small human ovarian tissue pieces within MAP hydrogels to investigate whether MAP hydrogels promote stable revascularization of grafted ovarian tissue (**Figure 3.2, E**). Cryopreserved human ovarian tissue squares were thawed and manually cut into cubes measuring ~1 mm in width and length to increase tissue surface-to-volume ratio by approximately 30%. Microgels were pipetted as two layers into a polydimethylsiloxane (PDMS) mold, with human ovarian tissue cubes embedded in between the microgel layers. This construct was then exposed to ultraviolet light to anneal the microgels, resulting in human ovarian tissue cubes fully encapsulated within a MAP hydrogel (OvaMAP). Following the same approach used for the non-encapsulated ovarian tissue strips, we then transplanted OvaMAPs into ovariectomized NSG female mice.

Confocal imaging of OvaMAPs (**Figure 3.3, A**) revealed that the onset of mouse vasculature infiltration occurred between 1 and 3 weeks post-transplantation. Quantitative analyses of mouse vasculature within ovarian tissue cubes demonstrated that mouse $CD31^+$ area (**Figure 3.3, B**), total vessel length (**Figure 3.3, C**), and mean branch length (**Figure 3.3, D**) increased significantly by 3 weeks and remained stable through 6 weeks, suggesting stable host revascularization of the human ovarian tissue cubes within OvaMAPs.

Similar to the non-encapsulated grafts, native human vasculature in the ovarian tissue cubes within OvaMAPs regressed over time. Initially, native human vasculature remained stable between 3 days and 1 week but decreased by 3 and 6 weeks (**Figure 3.3, E**). Nonetheless,

OvaMAPs retained approximately 10-fold greater native human vasculature compared to the non-encapsulated grafts.

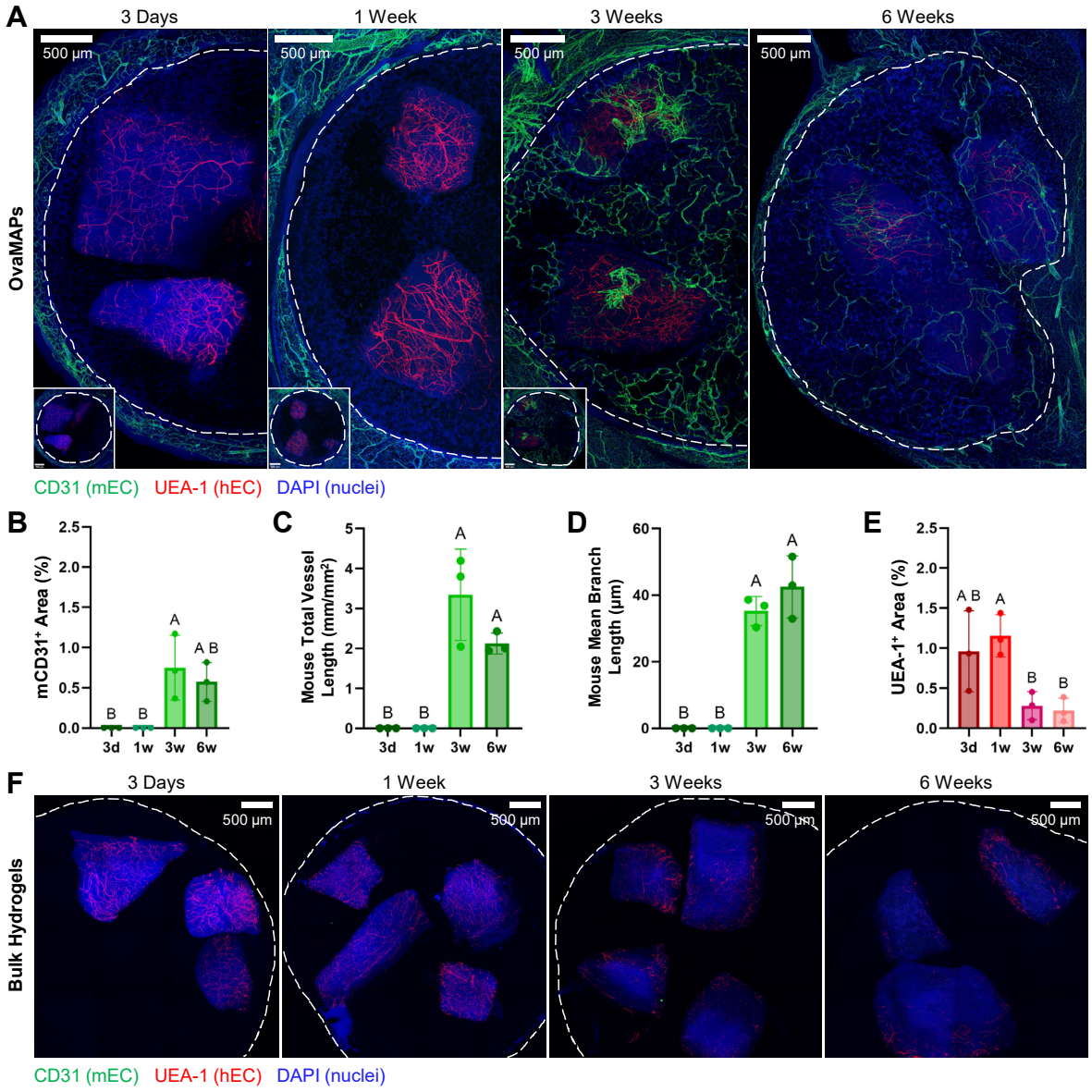


Figure 3.3 Revascularization of MAP Hydrogel-Encapsulated Human Ovarian Tissue Grafts. (A) Representative maximum intensity projection images show post-implantation mouse (CD31, green) and human (UEA-1, red) vasculature dynamics in human ovarian tissue cubes encapsulated in MAP hydrogels (OvaMAPs) over the course of 6 weeks. Dashed white lines delineate OvaMAP border within the surrounding mouse fat pad. Insets in the bottom left display the entire OvaMAP graft. **(B)** Percent area of OvaMAP human ovarian tissue cubes that stained positively for mouse vasculature. **(C)** Mouse total vessel length per OvaMAP total tissue cube area. **(D)** Mouse mean branch length within OvaMAP tissue cubes. **(E)** Percent area of OvaMAP human ovarian tissue cubes that stained positively for human vasculature. **(F)** Representative maximum intensity projection images show post-implantation mouse (CD31, green) and human (UEA-1, red) vasculature dynamics in human ovarian tissue cubes encapsulated in bulk hydrogels over the course of 6 weeks. Dashed white lines delineate the bulk hydrogel border. Note the lack of mouse CD31^{+} staining and the lack of mouse fat pad integration, suggesting the bulk hydrogel did

not support mouse vascular infiltration at any time point. Data points represent individual grafts from distinct mouse hosts (n = 3 per time point). Data analyzed by one-way ANOVA with Tukey's multiple comparisons test, $p < 0.05$, different letters indicate statistical significance.

As a non-microporous control for OvaMAPs, ovarian tissue cubes were encapsulated in bulk nanoporous PEG hydrogels and transplanted under identical conditions. Confocal imaging of these bulk hydrogel grafts showed similar regression of native human vasculature over time (**Appendix Figure B.4**). Importantly, bulk hydrogels showed no evidence of mouse vasculature infiltration up to 6 weeks post-transplantation (**Figure 3.3, F**).

3.3.4 MAP Hydrogel Interface Sustains Long-Term Graft Revascularization and Reperfusion

We next investigated the effect of host-biomaterial interface on graft revascularization by directly comparing OvaMAPs to non-encapsulated grafts. $DAPI^+$ cells were present within the MAP hydrogel pores at 3 days and 1 week (**Figure 3.4, A**). Non-encapsulated grafts showed early mouse vasculature infiltration that increased by 1 week but remained disorganized and primarily localized to the graft periphery (**Figure 3.4, B**). Accordingly, quantitative comparisons of mouse $CD31^+$ area (**Figure 3.4, C**) and mouse total vessel length (**Figure 3.4, D**) demonstrated no differences between OvaMAPs and non-encapsulated grafts at 3 days. At 1 week, non-encapsulated grafts exhibited greater mouse $CD31^+$ area and total vessel length compared to OvaMAPs.

By 3 weeks, magnified images of OvaMAPs revealed mouse vasculature within the surrounding fat pad, throughout the MAP hydrogel microporous network, and within the encapsulated human ovarian tissue cubes (**Figure 3.4, A**). In contrast, non-encapsulated grafts revealed a dramatic decrease in mouse vasculature infiltration (**Figure 3.4, B**). Quantitative comparisons demonstrated approximately 2-fold greater mouse $CD31^+$ area in OvaMAPs than in non-encapsulated grafts (**Figure 3.4, C**). Additionally, mouse total vessel length in OvaMAPs was approximately 4 times greater than in non-encapsulated grafts (**Figure 3.4, D**). By 6 weeks,

these differences were even more pronounced as OvaMAPs displayed an approximately 4-fold greater mouse $CD31^+$ area and 7-fold greater mouse total vessel length relative to non-encapsulated grafts (**Figure 3.4, C–D**). Moreover, analysis of mouse mean branch length (**Figure 3.4, E**) revealed that, although non-encapsulated grafts showed significantly longer mean branch lengths than OvaMAPs at 3 days and 1 week, this early advantage was not sustained and lost statistical significance by 3 and 6 weeks.

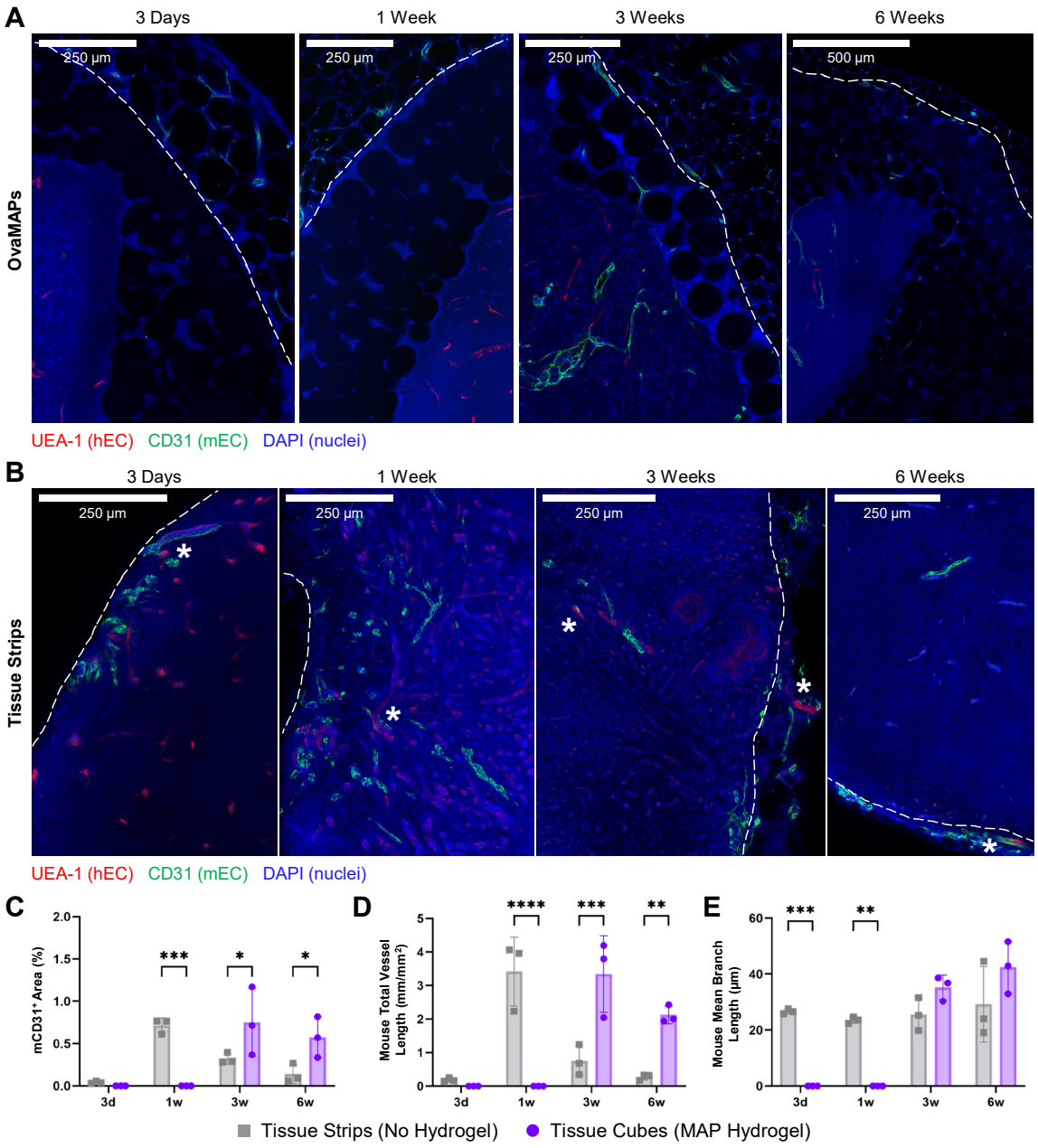


Figure 3.4 MAP Hydrogel Sustains Long-Term Human Ovarian Graft Revascularization. (A) Representative z-slice images demonstrate progressive cellular infiltration into OvaMAPs at 3 days to 6 weeks post-transplantation. Early DAPI$^+$ cell migration into MAP hydrogel pores was observed by 3 days, followed by infiltration of mouse CD31$^+$ endothelial cells by 3–6 weeks which localized to the encapsulated ovarian tissue. Dashed white lines delineate OvaMAP border within the surrounding mouse fat pad. **(B)** Representative z-slice images of non-encapsulated tissue strips depicting mouse vasculature infiltration into tissue grafts over the course of 6 weeks. Dashed white lines delineate the border of the implanted human tissue within the surrounding mouse fat pad. Asterisks indicate chimeric (UEA-1$^+$/CD31$^+$) vasculature. **(C)** Comparison of percent area of implanted human ovarian tissue that stained positively for mouse vasculature. **(D)** Comparison of mouse total vessel length per tissue strip area or per total tissue cube area (OvaMAPs). **(E)** Comparison of mouse mean branch length within tissue strip or tissue cubes (OvaMAPs). Data points represent individual grafts from distinct mouse hosts (n = 3 per time point, per condition). Data analyzed by two-way ANOVA with Šidák's multiple comparisons test, $p < 0.05$, significant difference indicated as *$p \leq 0.05$, **$p \leq 0.01$, ***$p \leq 0.001$.

To assess the functionality of infiltrating mouse vasculature, we stained 3- and 6-week time point OvaMAPs with a mouse red blood cell (RBC) marker (TER-119). At 3 and 6 weeks, numerous mouse vessels containing mouse RBCs were present throughout the MAP hydrogels' pores and within the encapsulated human ovarian tissue cubes (**Figure 3.5, A**). Higher magnification images revealed functional mouse vasculature infiltrating between the OvaMAP microgel subunits (**Figure 3.5, B, top row**), suggesting that the interstitial pore space guided the ingrowth of vascular structures. Functional mouse vessels were also identified within the encapsulated tissue cubes (**Figure 3.5, B, bottom row**), confirming that the human ovarian tissue received blood flow throughout the later time points.

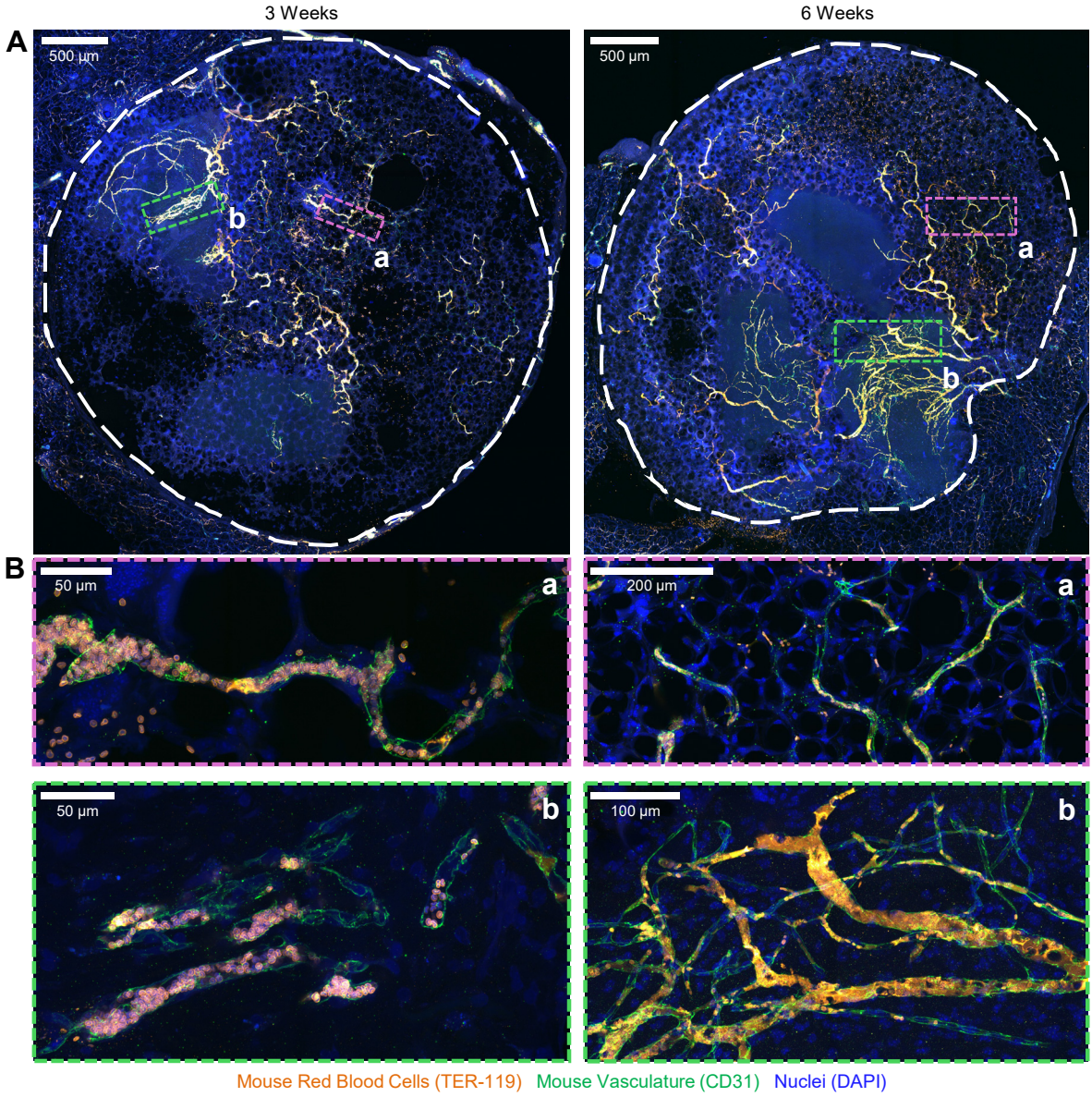


Figure 3.5 Perfused, Functional Host Revascularization of OvaMAPs. (A) Infiltrating mouse host vasculature (CD31, green) in OvaMAPs 3 and 6 weeks post-transplantation contains mouse red blood cells (TER-119, orange), confirming functional perfusion. **(B)** Perfused vasculature was evident both within MAP hydrogel pores **(a)** and within the encapsulated tissue cubes **(b)** at 3 and 6 weeks post-transplantation. Dashed white lines delineate OvaMAP border within the surrounding mouse fat pad. Magenta dashed lines delineate regions containing perfused vasculature within hydrogel pores while green dashed lines delineate regions containing perfused vasculature within encapsulated ovarian tissue cubes.

3.3.5 Hydrogel-Encapsulated Ovarian Tissue Restores Dynamic Ovarian Endocrine Function

Cryopreserved ovarian cortical tissue primarily contains immature follicles that require approximately 4 to 5 months to reach hormone-producing stages[13]. Accordingly, we investigated graft hormone production and integration with both the host hypothalamic-pituitary (HP) axis and host vasculature 20 weeks post-transplantation using ovariectomized NSG female mice engrafted with human ovarian tissue delivered either as non-encapsulated tissue strips or as cubes encapsulated in MAP or bulk hydrogels. Consistent with our previous analyses at 3 and 6 weeks, the 20-week non-encapsulated graft demonstrated minimal mouse vasculature infiltration while OvaMAP exhibited sustained mouse vasculature infiltration localized to the encapsulated human ovarian tissue cubes (**Figure 3.6, A**). Bulk hydrogels did not support mouse vasculature infiltration at any time point (**Figure 3.3, F; Figure 3.6, A**).

Measurements of circulating hormone levels in the host mice revealed that both non-encapsulated grafts and OvaMAPs produced significantly higher estradiol levels, 425.9 ± 270.5 pg/mL (mean ± SD) and 158.2 ± 37.91 pg/mL, respectively (**Figure 3.6, B**), compared to ovariectomized control female NSG mice (7.608 ± 4.745 pg/mL). Furthermore, all transplant conditions exhibited significantly lower follicle-stimulating hormone (FSH) levels compared to ovariectomized control female NSG mice (**Figure 3.6, C**). In ovariectomized control mice, FSH levels reached 95.16 ± 28.79 ng/mL due to the lack of sufficient concentrations of circulating estradiol. In contrast, FSH for non-encapsulated grafts, OvaMAPs, and bulk hydrogel grafts dropped to 18.21 ± 17.71 ng/mL, 32.61 ± 3.23 ng/mL, and 24.19 ± 6.27 ng/mL, respectively, suggesting integration of the grafts with the host HP axis and subsequent successful restoration of physiological negative feedback between estradiol and FSH.

Progesterone was also present and was not statistically different between the transplant conditions (non-encapsulated grafts: 21.36 ± 8.52 ng/mL; OvaMAPs: 19.31 ± 5.49 ng/mL; bulk hydrogel grafts: 18.87 ± 9.24 ng/mL), but was multifold higher than reported progesterone levels for ovariectomized and even intact NSG female mice[83], suggesting the presence of luteal cells in the grafts capable of responding to circulating gonadotropins (**Figure 3.6, D**). The presence of measurable progesterone levels further indicated that all three transplant conditions restored ovarian endocrine function by 20 weeks post-transplantation.

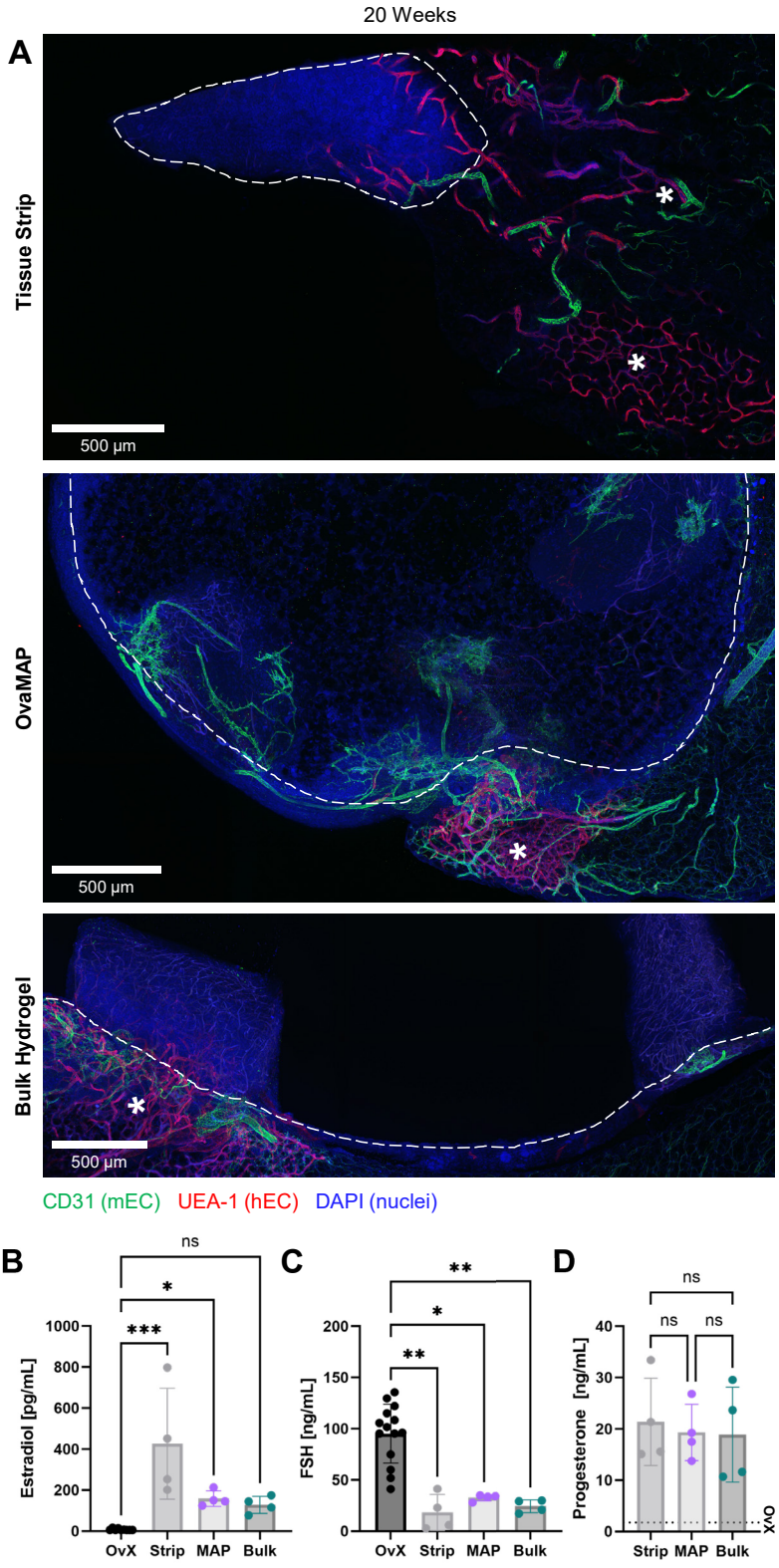


Figure 3.6 Long-term Graft Revascularization and Endocrine Function Restoration. (A) Representative maximum intensity projection images show post-implantation mouse (CD31, green) and human (UEA-1, red) vasculature dynamics within grafts 20 weeks post-transplantation. The non-encapsulated tissue strip image

comprises 6 z-slices. The OvaMAP and bulk hydrogel graft comprise 101 z-slices. Dashed white lines delineate graft borders within the surrounding mouse fat pad. Asterisks denote human UEA-1^+ vasculature in the adjacent host mouse tissue. At 20 weeks, serum estradiol **(B)**, follicle-stimulating hormone (FSH) **(C)**, and progesterone **(D)** levels were quantified in host mice (n = 4 per condition) implanted with non-encapsulated tissue strips, OvaMAPs, or bulk hydrogel-encapsulated tissue cubes. The dashed line marks mean progesterone levels in ovariectomized NSG mice from a previously published study[83]. Each data point represents one host mouse. Data analyzed by Kruskal-Wallis test with Dunn's multiple comparisons test, $p < 0.05$, significant differences indicated as *$p \leq 0.05$, **$p \leq 0.01$, ***$p \leq 0.001$.

3.4 Discussion

Restoration of durable ovarian graft function after OTCT remains limited by human ovarian tissue heterogeneity and ischemic tissue injury. In this study, engineering the host-graft interface using a MAP hydrogel fundamentally altered the trajectory of vascular integration of transplanted human ovarian tissue. Instead of the rapid but transient and disorganized vascular response observed with conventional transplantation, MAP delivery produced organized, perfused, and sustained revascularization that supported long-term endocrine function. These findings identify stabilization of vascular integration, rather than acceleration of early angiogenesis alone, as a critical determinant of graft performance, and introduce a fully synthetic, tunable platform for improving OTCT outcomes.

Current clinical practice involves the avascular transplantation of non-encapsulated ovarian tissue, with the assumption that early host vessel infiltration will revascularize the graft and enable its long-term function. The temporal analysis presented here, however, challenges this assumption. Non-encapsulated grafts exhibited a surge in host vascular infiltration at 1 week, consistent with previous studies[29,30,84], but this response subsequently diminished by 3 to 6 weeks and was accompanied by sparse and disorganized vessels largely confined to the graft periphery. Prior xenograft studies have focused primarily on early (days [30–33]) or late (months [34,35]) endpoints; by including intermediate time points, we reveal a previously underappreciated phase of vascular instability in OTCT. Our findings likely reflect the rapid formation of immature or

poorly integrated vessels at the non-encapsulated tissue interface that fail to remodel into a durable vascular network, providing a potential mechanistic explanation for the highly variable graft function noted clinically.

In contrast, MAP-encapsulated grafts exhibited progressive host vascular ingrowth that increased between 1 and 3 weeks and remained evident through later time points. Host vessels infiltrating OvaMAPs were perfused and extended through the interconnected pore network into the tissue core, resulting in substantially greater vessel area and length than in non-encapsulated grafts. Additionally, bulk nanoporous hydrogels failed to support vascular infiltration, indicating that microporosity was necessary for stable, functional revascularization. Importantly, the vascular patterns observed in OvaMAPs suggest progression toward a more mature vessel network. While host vessel density within the hydrogel interstitial spaces appeared reduced at later time points, host vessels persisted within and immediately around the encapsulated tissue cubes, consistent with remodeling of vessels towards a mature network. Together, these findings demonstrate that the physical structure of the host-graft interface can dictate the quality and persistence of vascular integration. In this study, the host-graft interface established by the OvaMAP platform supported the transition from vascular ingrowth to sustained integration rather than producing a short-lived burst of angiogenesis.

Several features of the MAP system likely contributed to the revascularization dynamics observed in the encapsulated ovarian tissue cubes. The interconnected cell-scale pore network supported molecular transport and host cell infiltration while plasmin-sensitive microgel crosslinks enabled proteolytic remodeling aligned with endogenous ovarian matrix remodeling[82] and angiogenesis[85]. In parallel, the non-degradable annealing chemistry within and between microgels preserved overall scaffold integrity, producing a semi-degradable structure that

allowed tissue remodeling without premature scaffold collapse. Additionally, encapsulation of small tissue fragments increased tissue surface-to-volume ratio and enabled controlled spatial positioning of tissue relative to host tissue – parameters that are known to influence graft survival and revascularization but difficult to achieve reproducibly with non-encapsulated ovarian tissue strips.

At 20 weeks, both non-encapsulated grafts and OvaMAPs restored circulating estradiol, progesterone, and physiologic suppression of FSH, indicating integration of the grafts with the host HP axis. This timing aligns with clinical observations that ovarian function resumes 4 to 5 months after transplantation, supporting the translational relevance of the ovariectomized mouse model. Estradiol levels in the non-encapsulated group were highly variable, reflecting the well-documented heterogeneity of human ovarian tissue and the unpredictable clinical duration of graft function which ranges from months to years. In contrast, OvaMAP recipients exhibited more consistent estradiol levels, suggesting that the controlled hydrogel microenvironment itself may reduce functional variability which is a key unmet need in OTCT. These findings should also be interpreted in light of the bulk hydrogel group, which likewise demonstrated more consistent estradiol levels, progesterone production, and suppression of FSH despite the lack of revascularization. This suggests that endocrine recovery at this time point is not governed by revascularization alone and may be supported, in part, by passive diffusion. These findings leave open the possibility that an optimized OvaMAP platform capable of achieving early and sustained vascular integration may ultimately improve both the consistency and long-term durability of graft function beyond 20 weeks.

Several limitations, however, should be acknowledged. The use of an immunodeficient xenograft model does not recapitulate the full spectrum of innate and adaptive immune responses

that influence angiogenesis, fibrosis, and long-term graft remodeling in patients. MAP hydrogels have been shown to modulate immune responses in other tissues[86–91] and such interactions may contribute to graft performance but were not captured here. Furthermore, the identity of early infiltrating $DAPI^{+}/CD31^{-}$ cells remains undefined and warrants further investigation, particularly given the possibility that they contributed to subsequent vascular remodeling. While $TER\text{-}119^{+}$ red blood cells were found within infiltrating host vessels, this immunolabeling represents a static indication of perfusion and does not provide dynamic information on blood flow quality. Real-time imaging approaches capable of assessing graft perfusion in vivo would therefore strengthen future studies[29,92–94]. Although this work focused on investigating improved graft vascular integration, additional optimization of hydrogel composition may further enhance follicle survival, support later stages of folliculogenesis, or accelerate revascularization. Donor availability also limited sample size and age diversity; future studies across a broader donor population will be necessary to assess reproducibility.

Beyond their relevance to ovarian tissue, these findings highlight the host-graft interface as an actionable therapeutic target for whole tissue transplantation. The modular architecture of MAP hydrogels provides a clinically adaptable platform that can be tuned to incorporate proangiogenic cues, retain endogenous angiogenic growth factors, or enable minimally invasive tissue delivery as an injectable biomaterial. As a fully synthetic and compositionally defined material, this system also offers advantages for manufacturing consistency and regulatory translation compared to naturally derived matrices.

In summary, engineering the transplantation microenvironment with a microporous synthetic scaffold enabled sustained, perfused revascularization of human ovarian tissue and supported long-term endocrine function restoration within a clinically relevant timeframe. By

promoting more stable vascular remodeling and providing a more controlled graft microenvironment, MAP hydrogel delivery addresses two central limitations of current OTCT practice: ischemic graft injury and unpredictable graft performance. These results establish a foundation for biomaterial-based strategies aimed at extending graft lifespan and improving the reliability of fertility and endocrine function restoration for patients at risk of POI.

Chapter 4 Conclusions and Future Directions

Ovarian tissue cryopreservation and transplantation (OTCT) is a clinically established procedure capable of restoring both ovarian endocrine function and fertility in cancer survivors. Nonetheless, graft performance remains difficult to predict as evidenced by low live birth rates and variable graft longevity which ranges from months to years across patients. This variability complicates clinical decision-making and patient counseling and highlights a central limitation of OTCT practice: although the procedure can be effective, the outcomes are often unpredictable.

This dissertation examines two factors contributing to the variability of graft performance. First, human ovarian tissue is intrinsically heterogeneous. Follicle number, follicle spatial distribution, stromal composition, and vascular organization vary both between patients and within a single ovary. This heterogeneity influences tissue response to cryopreservation and transplantation and, as a result, different pieces of ovarian tissue possess different functional outcomes with respect to fertility and restoration of ovarian endocrine function. Second, ovarian tissue is transplanted in an avascular manner and therefore endures a period of ischemia before host vessels revascularize the graft. It is hypothesized that ischemic and reperfusion injuries contribute to follicle loss and disruption of vascular networks and stromal integrity, thereby influencing long-term durability and consistency of graft function.

The work presented in this dissertation addresses both of these factors. It establishes and validates a workflow for volumetric characterization of human ovarian microarchitecture, enabling three-dimensional analysis of follicles and vasculature within their native tissue

architecture. Subsequently, it demonstrates that modulating the host-graft interface using microporous annealed particle (MAP) hydrogels promotes sustained vascular integration and reduces variability in hormone production following transplantation. Overall, this dissertation presents a framework in which advanced volumetric imaging and intentional control over graft-host interface and transplantation microenvironment are leveraged to interrogate and improve OTCT outcomes.

4.1 Summary of Findings: Three-Dimensional Characterization of Human Ovarian Tissue

Histology is indispensable for ovarian research and clinical tissue assessment, but it reduces complex three-dimensional structures to two-dimensional sections. In human ovarian cortex, where follicle distribution is heterogeneous and vascular networks are spatially complex, this dimensional reduction limits our understanding of follicle and vessel arrangement within intact volumes.

In this dissertation, a CUBIC (clear, unobstructed brain imaging cocktails and computational analysis) tissue clearing protocol was adapted and validated for human ovarian cortex and medulla. Clearing significantly improved tissue imaging depth relative to non-cleared controls and, importantly, was compatible with ovarian cortex cryopreserved following the clinical protocol for fertility preservation. Follicle density measurements derived from cleared tissue were comparable to those obtained through conventional histology, confirming that volumetric imaging preserved the quantitative accuracy of a key metric used in ovarian research. Additionally, clearing combined with light sheet imaging enabled quantitative mapping of cortical vascular morphometrics, including vessel diameter, length density, branch point density, and vessel volume fraction across intact tissue volumes, metrics that are rarely quantified in three dimensions in human ovarian tissue.

The value of the developed workflow lies not in replacing histology, but in enabling measurement of structural variability at the scale relevant to ovarian tissue transplantation. Histology remains appropriate for routine follicle counting and staging when follicle morphology is the principal endpoint. Comparatively, tissue clearing is especially useful when follicles must be interpreted together with surrounding stromal and vascular features within the same tissue piece. This distinction is important for OTCT, where graft outcomes are broadly attributed to ischemic and reperfusion injuries, follicle apoptosis, and abnormal follicle activation, but the structural basis of these processes remains incompletely understood. As such, tissue analysis approaches that preserve tissue-scale architecture may offer insight that is difficult to obtain from sparse two-dimensional sections alone. Tissue clearing therefore functions not simply as a three-dimensional counting tool, but as a mechanistic research tool that can help link follicle behavior, stromal structure, and vascular remodeling. Using this workflow, structural heterogeneity transitions from a biological constraint to a measurable parameter that can inform translational engineering technologies designed to improve ovarian graft performance.

4.2 Summary of Findings: Engineering the Host-Graft Interface

Rapid angiogenesis has long been considered the primary determinant of ovarian graft survival. The findings in this dissertation, however, demonstrate that early revascularization of ovarian grafts is a transient and spatially disorganized vascular response. These observations offer a potential explanation for the graft variability observed clinically in patients and indicate that both speed and stability of revascularization are important determinants of predictable, long-term ovarian graft performance.

To investigate whether architectural modulation of the host-graft interface could influence these vascular dynamics, a MAP hydrogel platform was developed to encapsulate and

transplant human ovarian tissue cubes (OvaMAP). The MAP scaffold consisted of annealed poly(ethylene glycol) (PEG) microgels which formed an interconnected pore network that facilitated host cell infiltration and vascular ingrowth. Compared to non-encapsulated tissue, OvaMAPs demonstrated a more gradual but sustained pattern of vascular integration with perfused host vessels present throughout both the microporous scaffold network and the encapsulated tissue at later time points. These findings indicate that microporous architecture promotes durable vascular remodeling rather than transient angiogenic spikes. Functionally, OvaMAPs restored ovarian endocrine function within a clinically relevant timeframe and exhibited reduced variability in circulating estradiol levels relative to non-encapsulated tissue. This reduction in variability suggests that structured microenvironmental conditions, including but not limited to stabilized vascular integration, may contribute to more consistent graft function.

Although graft outcomes are influenced by a multitude of factors, including follicle content and tissue surface-to-volume ratio, the findings presented in this dissertation establish that structural features of the transplantation microenvironment represent a controllable variable capable of influencing vascular organization and functional variability. By focusing initially on architectural modulation without introducing exogenous growth factors or complex biochemical modifications, this work provides a baseline transplant scaffold structure which can be combined with future modifications to further improve OTCT outcomes.

4.3 Future Directions

4.3.1 Expanding Structural Understanding

Future studies should extend three-dimensional volumetric characterization of human ovarian tissue to a broader demographic range as age-related changes in stromal density, vascular

organization, and follicle distribution influence graft longevity and endocrine function recovery following OTCT. Such datasets across diverse age groups and clinical backgrounds could clarify correlations between baseline tissue microarchitecture and expected graft performance.

Further characterization of additional tissue regions, including the ovarian medulla, is also warranted. The medulla is more highly vascularized and contains a less dense stromal matrix compared to the cortex, and prior work suggests that inclusion of medullary tissue may improve graft survival[95–98]. As such, comprehensive three-dimensional mapping of medullary tissue structure may inform strategies that leverage its vascular properties to improve transplantation outcomes.

Lastly, future application of tissue clearing to cryopreserved and transplanted ovarian tissues within a research setting may improve our understanding of several contributors to graft function. Simultaneous labeling of follicles and vasculature may reveal structural constraints on follicle survival and growth. Additionally, visualization of stromal cell populations, fibrosis, and extracellular matrix components in three dimensions may be valuable for investigating the interrelationship between follicle loss, activation, and tissue injury. Together, this increased understanding of graft biology could direct biomaterial scaffold design parameters to better support graft integration and function.

4.3.2 Optimizing the OvaMAP Platform

The work presented in this dissertation establishes that the host-graft interface is a controllable variable and therefore a practical starting point for improving OTCT. As a result, the OvaMAP platform can be refined first through scaffold architecture and microenvironment design rather than relying immediately on increasingly complex biologic additions. Such an

approach may provide a more clinically viable route toward improved OTCT outcomes while allowing the potential future layering of more sophisticated biochemical or cellular strategies.

4.3.2.1 Architectural Refinement

Architectural tuning of the MAP hydrogel represents the most immediate and translationally realistic direction for future work with the OvaMAP platform. Systematic variation in microgel size, pore size, microgel geometry, and incorporation of sacrificial porogens could generate hierarchical pore networks that influence oxygen diffusion, host cell infiltration kinetics, and long-term vessel stability. As such, identifying architectural parameters that balance rapid vascular access with long-term vessel stability will be essential for sustaining reliable graft function.

4.3.2.2 Biochemical Refinement

Biochemical refinements may also be layered upon this structural foundation, but they should be pursued with care. Following transplantation, ischemic injury triggers rapid upregulation of endogenous angiogenic cues such as vascular endothelial growth factor (VEGF), platelet-derived growth factor (PDGF), and basic fibroblast growth factor (bFGF)[99]. One potential biochemical refinement is therefore the leveraging of these endogenous signals rather than relying on supraphysiologic exogenous growth factor dosing. Inclusion of microgel subpopulations functionalized with heparin[42,100] could locally retain these endogenous cues, thereby amplifying physiologic angiogenic signaling in the graft microenvironment. Extracellular matrix (ECM)-binding peptides represent another functionalization option[101] for microgels to help localize host- or graft-produced ECM in order to support provisional matrix stabilization, local cell adhesion, or remodeling processes beneficial for vascular integration.

Other biochemical additions may also be useful as secondary modifications to the OvaMAP platform. Short-lived matrix cues, such as fibrin, could serve as temporary pro-angiogenic substrates within the MAP hydrogel pore space while preserving the relative simplicity of the overall platform[102,103]. Additional microgel modifications involving oxygen-generating chemistries[104], reactive oxygen species-scavenging strategies[105], or exogenous pro-angiogenic growth factors delivery[106,107] could transiently mitigate hypoxia, attenuate ischemia-reperfusion injury associated oxidative stress, and enhance early endothelial cell recruitment and subsequent vessel stabilization, respectively. While promising, these strategies introduce additional regulatory and biological complexity. For instance, pro-angiogenic cues such as VEGF may accelerate graft revascularization while also promoting premature follicle activation[21,22]. In response, cellular support strategies could be used to reduce premature follicle activation while improving graft integration. Specifically, prior work shows that endothelial cells engineered to secrete anti-Müllerian hormone (AMH) support graft revascularization and preserve the primordial follicle pool in ovarian grafts[35]. However, as with exogenous biologic additions, cell-based support introduces additional complexity related to cell sourcing, characterization, manufacturing, and regulatory translation. Consequently, future work may benefit from prioritizing scaffold architecture, endogenous growth factor and ECM sequestration, and transient matrix cues before moving toward more complex biochemical additions.

4.3.2.3 Medulla-Derived Support

Strategies involving the inclusion of cell populations derived from the medulla may offer an alternative to the support cell approach mentioned above as the ovarian medulla is more vascularized than the cortex and therefore contains components that may be relevant to angiogenesis and matrix remodeling post-transplantation. However, this approach would require

substantial characterization of cell populations remaining after medullary digestion and investigation of whether those populations meaningfully support vascularization and stromal repair. This approach is also limited by the fact that only ovarian cortex, rather than medulla, is typically cryopreserved in current fertility preservation protocols. Nonetheless, in some clinical workflows, advanced surgical preparation of the transplant site[108–111] could create an opportunity to obtain medullary tissue for processing.

4.3.2.4 Graft Preparation: Tissue Priming and Minimizing Follicle Activation

Another important area for future work is the tissue itself, including pre-transplant tissue priming and the downstream biological consequences of processing tissue for OTCT. Priming could refer to several different goals, including promotion of revascularization, reduction of tissue injury, reduction of follicle loss, or suppression of abnormal follicle activation[112]. Pilot studies described in Appendix E explored whether short-term pre-transplant culture could encourage endothelial cell outgrowth from ovarian tissue as a means of supporting post-transplantation vascular integration. However, these studies were not especially promising as endothelial outgrowth was difficult to obtain in a robust manner and isolated endothelial cell outgrowth would not necessarily be sufficient to rapidly produce stable vascular structures post-transplantation. These pilot studies also highlighted an important practical limitation: prolonged ex vivo tissue manipulation likely introduces additional tissue stress. If priming strategies are to be clinically useful, they will likely need to be brief, such as short-duration incubation of tissue, or delivered into the host[21].

Tissue processing also warrants greater attention. During OTCT, the loss of growing follicles due to cryopreservation may reduce AMH-mediated suppression of primordial follicle recruitment[113]. While cutting ovarian tissue into smaller cubes to increase surface-to-volume

ratio and diffusion access remains attractive for improving graft survival in the early post-transplantation period, this benefit may come at a biological cost as mechanical manipulation of the ovarian cortex disrupts signaling pathways that normally maintain primordial follicles in a quiescent state[113]. As such, tissue preparation in OTCT is a double-edged intervention as it can improve transport conditions but may also contribute to premature depletion of the follicle reserve. Future studies should therefore take into consideration methods for preserving physiologic follicle quiescence post-transplantation.

4.3.2.5 Clinical Translation

Clinical translation of the OvaMAP platform will depend on improved fabrication control and more physiologically relevant model systems. To adapt this platform for patient use, the most realistic path forward is unlikely to involve simply increasing graft or scaffold size, as larger constructs would reintroduce diffusion limitations. Instead, implantation of multiple smaller constructs will be necessary. Within this framework, reproducibility becomes a challenge as the current manual pipetting of microgels and manual placement of tissue pieces provide limited geometric control. Robotic handling, templated assembly, or bioprinting-based assembly may help standardize tissue spacing and scaffold architecture while preserving favorable diffusion properties. Transitioning toward clinically compatible annealing chemistries is likewise important, both to avoid tissue exposure to ultraviolet light and to ensure the OvaMAP scaffold remains compatible with the laparoscopic transplantation workflows currently used clinically.

Clinical translation may also benefit from greater attention to the transplantation site. Currently, some clinical centers perform tissue transplantation as a two-step procedure in order to induce angiogenesis and neovascularization at the transplant site[108–111]. An initial laparoscopy is performed to generate growth of granulation tissue followed by a second laparoscopy 3–7 days

later during which the cryopreserved ovarian tissue is implanted. This concept is especially attractive if advanced transplant site preparation also creates an opportunity to obtain medullary tissue for harvesting patient-derived support cell populations. Furthermore, xenograft studies involving advanced transplant site preparation with adipose tissue-derived stem cells (ASCs) embedded in fibrin have reported beneficial effects[31–34], suggesting that transplant site pre-conditioning may positively influence the local transplantation environment. As such, graft outcomes may depend not only on the transplanted tissue and scaffold architecture, but also on the state of the recipient. Future work could therefore investigate whether coordinated optimization of the graft microenvironment and the transplantation site improves the timing and stability of graft revascularization as well as long-term graft function.

Selection of physiologically relevant models is also necessary for translational evaluation of the OvaMAP platform. The highly immune-compromised NSG xenograft model used in this dissertation was appropriate for controlled study of human ovarian tissue, but it does not recapitulate the full immune environment that shapes graft remodeling in patients. This limitation is especially relevant when interpreting host responses to the biomaterial interface. Granular hydrogels are often associated with wound-healing and remodeling responses rather than dense fibrotic encapsulation due to their porosity and softness[114]. Regardless, implantation of foreign bodies involves protein adsorption, provisional matrix formation, innate immune cell recruitment, and interface remodeling. In this dissertation, the NSG mouse model is considered immune-compromised yet retains the presence of defective immune cells. As such, the OvaMAPs may have experienced some degree of innate immune cell interaction in the form of protein deposition without reproducing a complete foreign body reaction. This may be important for interpreting the difference in vascular integration timing between the exposed non-

encapsulated tissue strips and the encapsulated tissue cubes, particularly given the early $DAPI^{+}/CD31^{-}$ cells noted within the OvaMAP pore space and the possibility that the hydrogel altered where interface remodeling occurred relative to the tissue itself. Future studies in immune-competent models may therefore be useful for clarifying how OvaMAPs interact with innate and adaptive immune responses in the context of scaffold remodeling and ischemia-reperfusion injury. Humanized mouse models may provide a useful intermediate step for short-term immune questions due to their short lifespans whereas larger animal models, such as non-human primates, may be needed to assess long-term immune investigations, graft revascularization, and ultimately, graft function, which are essential for assessing the long-term translational potential of OvaMAPs.

4.4 Toward Improving OTCT Outcomes

The central contribution of this dissertation is its reframing of ovarian graft variability as a phenomenon that can be measured, interpreted, and, in part, engineered, instead of accepting it as an unavoidable clinical uncertainty. Variability in graft function and longevity reflects intrinsic tissue heterogeneity and instability of vascular remodeling following transplantation. By developing tools to characterize ovarian microarchitecture and strategies to stabilize post-transplantation host-graft integration, this work demonstrates that these structural determinants can be systematically studied and modulated.

Improving OTCT outcomes will depend on iterative feedback between structural analysis and graft design. Tissue clearing can be used to define baseline tissue heterogeneity, assess the effect of cryopreservation and transplantation on tissue organization, and eventually investigate the influence of scaffold-based interventions on follicle-stromal-vascular relationships. In parallel, biomaterial platforms such as OvaMAP can be tuned to improve the long-term function

and predictability of ovarian grafts. As such, tissue clearing and the OvaMAP platform address a different side of the same problem in OTCT: one improves the ability to measure and interpret structural variability, while the other provides a means to shape the transplantation microenvironment in which this heterogeneous tissue must survive and function.

Achieving control over the transplantation microenvironment requires material systems that permit independent and reproducible tuning of architectural parameters. In this dissertation, the use of a synthetic and compositionally defined PEG MAP hydrogel platform is significant. Unlike naturally derived scaffolds, synthetic scaffolds enable precise control of pore architecture, degradation kinetics, and mechanical properties without batch-to-batch variability. Such control is advantageous not only experimentally but also for translational considerations including manufacturing consistency and regulatory evaluation. Importantly, reproducible design is a prerequisite for achieving predictable graft performance in patients. More consistent graft performance may guide tissue allocation decisions, optimize timing of transplantation, and improve counseling regarding expected duration of endocrine function and reproductive potential, which all directly impact patient long-term health, reproductive autonomy, and quality of life.

Together, the studies presented in this dissertation establish complementary analytical and engineering strategies for studying and improving OTCT. Tissue clearing provides a framework for examining ovarian microarchitecture while MAP hydrogels provide a controllable platform for modulating host-graft integration. These contributions provide a framework for advancing OTCT toward greater reliability.

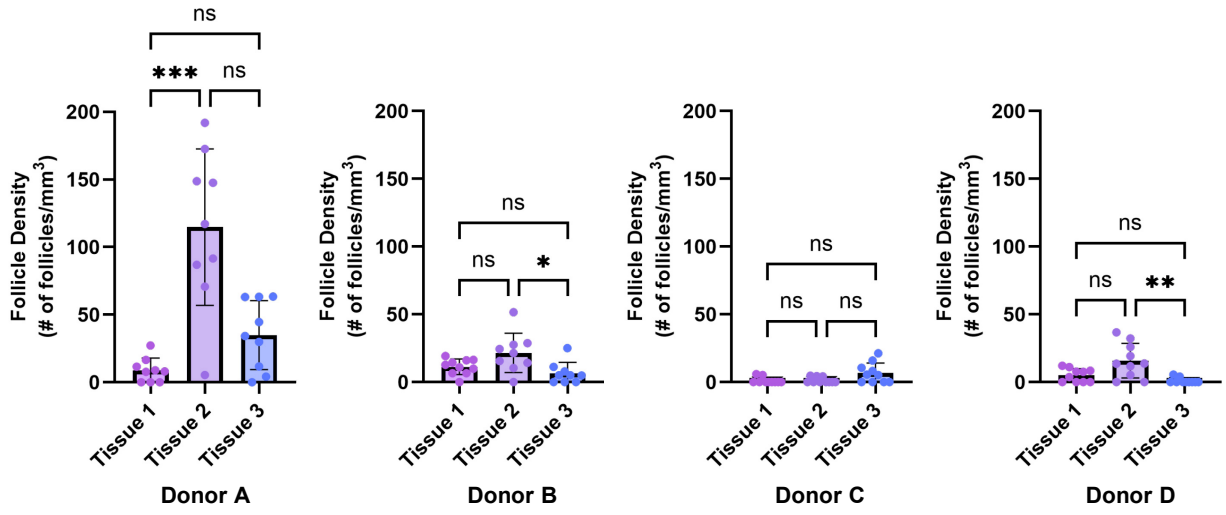
Appendices

Appendix A: Chapter 2 Supplemental Materials

Appendix Table A.1 Donor Tissue-Specific Follicle Density.

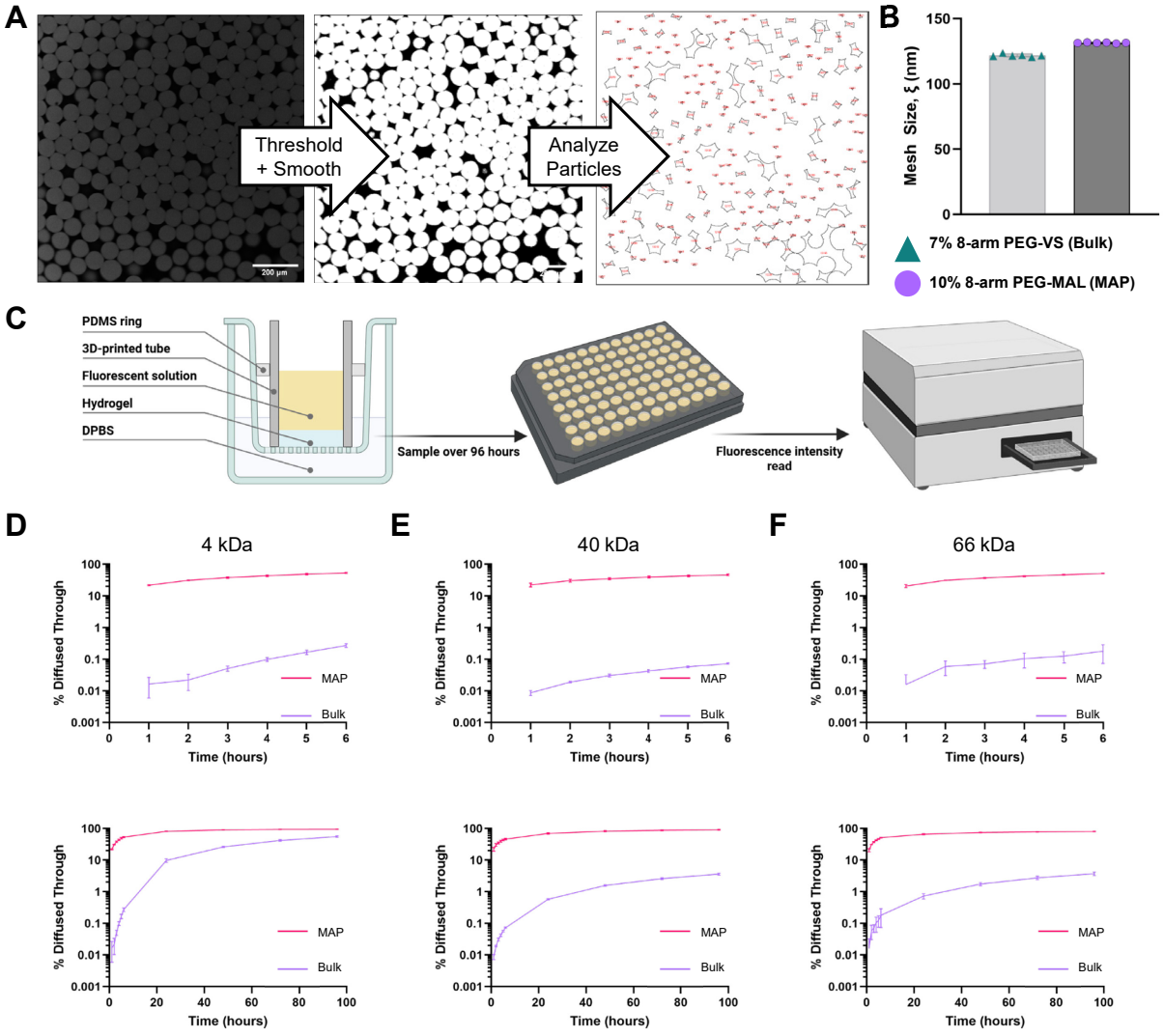
Mean and standard deviation for follicle densities across each of the three analyzed tissue pieces for Donors A–D. Follicle density is expressed as number of follicles per mm^3.

	Donor A			Donor B			Donor C			Donor D		
Tissue	**1**	**2**	**3**	**1**	**2**	**3**	**1**	**2**	**3**	**1**	**2**	**3**
Mean	9	115	35	11	22	7	1	1	7	5	16	1
StDev	9	58	26	6	14	8	2	2	7	5	13	2

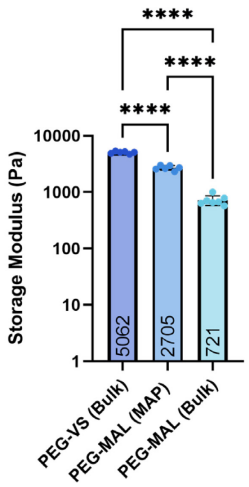


Appendix Figure A.1 Intra-Donor Follicle Density Heterogeneity. Follicle densities across each of the three analyzed tissue pieces for Donors A–D. Each data point represents the follicle density within one z-stack substack (9-10 substacks per tissue piece), error bars are mean ± standard deviation per tissue piece. Data analyzed by Kruskal-Wallis test with Dunn's multiple comparisons test, $p < 0.05$, significant differences indicated as *$p \leq 0.05$, **$p \leq 0.01$, ***$p \leq 0.001$.

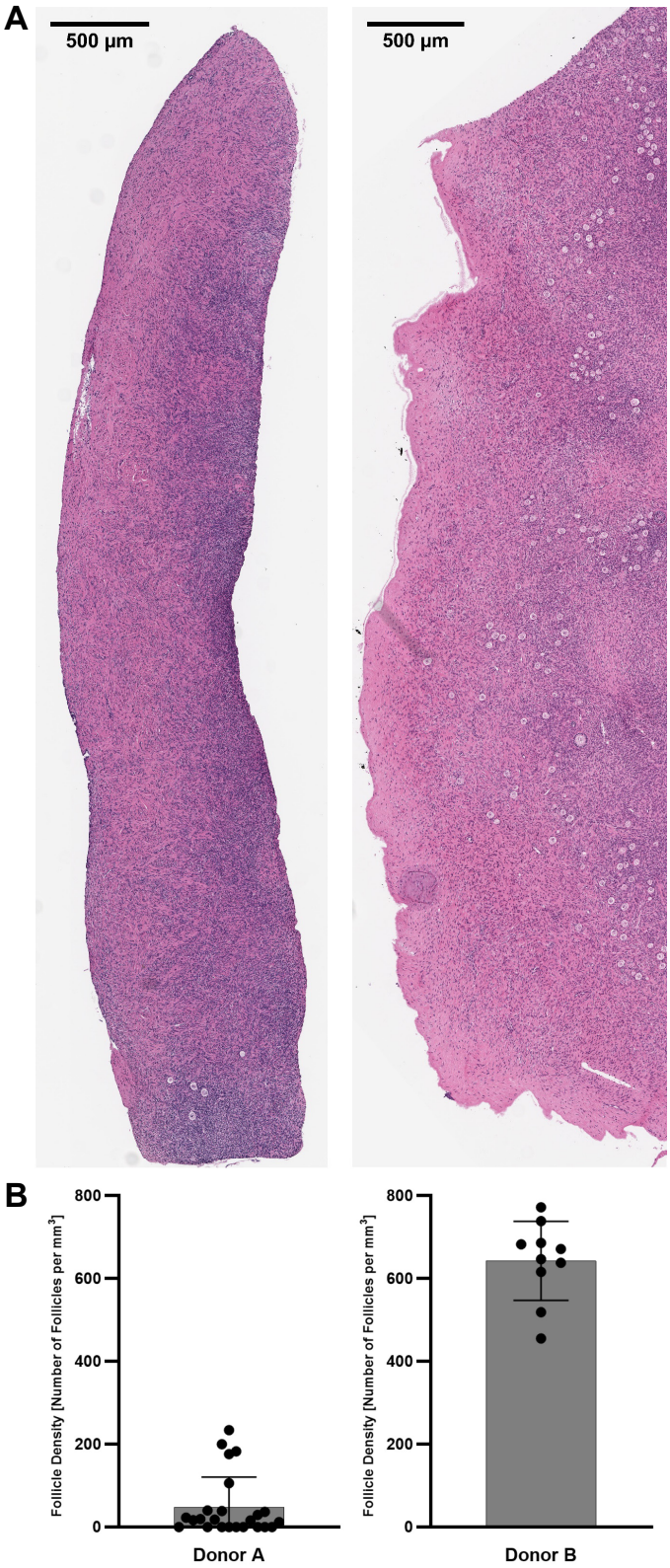
Appendix B: Chapter 3 Supplemental Materials



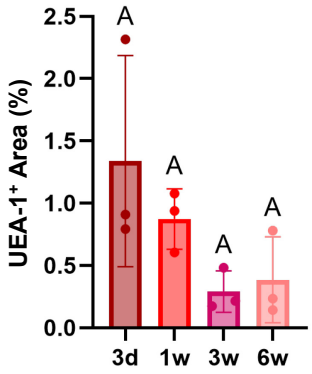
Appendix Figure B.1 Characterization of MAP Hydrogel Porosity, Mesh Size, and Diffusion. (A) Workflow illustrating porosity quantification from confocal images using FIJI (ImageJ). **(B)** Nanoporous bulk hydrogel mesh sizes for MAP hydrogel and bulk hydrogel formulations (n = 6 per condition) were estimated from swelling ratios. **(C)** Illustration of experimental methods used to determine the diffusion of molecules through bulk and MAP hydrogels. Short- and long-term diffusion of 4 kDa FITC-DEX **(D)**, 40 kDa FITC-DEX **(E)**, and 66 kDa Alexa Fluor 488-BSA **(F)** through MAP (pink) and bulk (purple hydrogels) (n = 3 per hydrogel type). Short-term measurements were conducted hourly for 6 hours while long-term measurements were conducted every 24 hours over 96 hours.



Appendix Figure B.2 Hydrogel Storage Moduli. Storage modulus of PEG-VS bulk hydrogel, PEG-MAL MAP hydrogel, and bulk hydrogel fabricated using the PEG-MAL microgel formulation. A minimum of n = 6 hydrogels were tested per condition, error bars are mean ± standard deviation per group. Data analyzed by one-way ANOVA with Tukey's multiple comparisons test, $p < 0.05$, significant differences indicated as ****$p \leq 0.0001$.



Appendix Figure B.3 Human Donor Ovarian Cortex Characterization. (A) Representative hematoxylin and eosin (H&E) staining of fresh fixed ovarian cortex from donors A and B, with corresponding estimated follicle densities **(B)**. Error bars are mean ± standard deviation per group.



Appendix Figure B.4 Human Vasculature Regression within Bulk Hydrogel-Encapsulated Tissue. Percent area of implanted, bulk hydrogel-encapsulated human ovarian tissue cubes that stained positively for human vasculature. Data represent individual grafts from distinct mouse hosts (n = 3 per time point), error bars are mean ± standard deviation per group. Data analyzed by one-way ANOVA with Tukey's multiple comparisons test, $p < 0.05$, different letters indicate statistical significance.

Appendix C: MAP Hydrogel Formulation Development

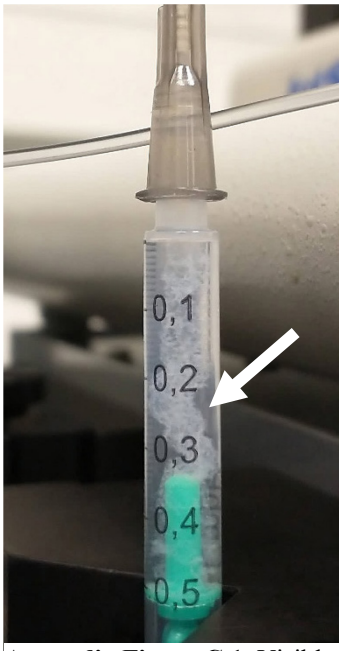
When I undertook the development of a microporous annealed particle (MAP) hydrogel for human ovarian tissue encapsulation and transplantation, the initial objective was to adapt the Shikanov Lab's established poly(ethylene) glycol (PEG)-based hydrogel formulation for compatibility with microfluidic droplet generation. The laboratory's baseline formulation consisted of 5% 8-arm PEG-vinyl sulfone (PEG-VS) crosslinked with the trifunctional plasmin-sensitive crosslinking peptide YKNS at a 1:1 stoichiometric ratio of VS to thiol (SH) groups between PEG-VS and YKNS. Both PEG-VS and YKNS were prepared in HEPES buffer (pH 7.4). Under these conditions, gelation occurred within approximately 5 minutes and produced hydrogels with swelling ratios of ~28. This formulation was well-suited for ovarian tissue and follicle encapsulation due to its rapid gelation kinetics and enzymatically degradable crosslinking chemistry. However, these rapid gelation kinetics were incompatible with microfluidic droplet generation, which required precursor solutions to remain liquid and minimally viscous for hours rather than minutes.

The studies summarized in **Appendix Table C.1–11** reflect a non-linear hydrogel formulation optimization process conducted simultaneously across three criteria: (1) achieving multi-hour gelation windows to permit microfluidic processing, (2) maintaining swelling ratios comparable to the laboratory's baseline PEG-VS hydrogel, and (3) identifying microgel annealing strategies capable of producing a MAP hydrogel within 5-10 minutes to accommodate live tissue encapsulation. While hydrogel formulation development was performed in parallel

with evaluation of multiple microfluidic droplet generation platforms (Appendix E), all platforms required microgel precursor solutions to remain sufficiently liquid to prevent premature gelation during droplet formation.

C.1 Delaying Hydrogel Gelation

Initial efforts focused on modifying the established PEG-VS/YKNS chemistry by reducing HEPES buffer pH (**Appendix Table C.1**), as thiol-vinyl sulfone Michael-type addition is pH dependent. As expected, gelation at pH 7-7.4 occurred within minutes, consistent with the laboratory baseline. Lowering the pH progressively delayed gel formation, with some conditions remaining liquid overnight. These experiments confirmed that reaction kinetics could be slowed; however, achieving multi-hour working windows required substantial pH reduction, raising concerns regarding polymer network integrity and mechanical performance.



Appendix Figure C.1. Visible disulfide bond formation (white arrow) within syringe containing YKNS solution being delivered to microfluidic device.

To evaluate the impact of reduced pH on polymer network structure, swelling ratios were measured (**Appendix Table C.5**). Encouragingly, HEPES buffer at pH 6.5, which produced extended gelation timeframes, did not substantially increase swelling relative to the laboratory benchmark (~28). However, as microfluidic device testing progressed, it became apparent that acidic HEPES buffer alone was insufficient to prevent disulfide bond formation in YKNS solutions (**Appendix Figure C.1**). To mitigate this, YKNS preparation was transitioned to TCEP-containing solutions (**Appendix Table C.6**), which effectively stabilized YKNS and contributed to delayed gelation. Nonetheless, the incorporation of TCEP resulted in notable

hydrogel swelling unless PEG-VS was returned to a more neutral-to-basic HEPES buffer environment.

C.2 Development of Annealing Strategies for PEG-VS

While gelation and swelling optimization were ongoing, microgel annealing strategies were simultaneously explored with PEG-VS microgels (**Appendix Table C.9–11**). In contrast to microgel generation, which necessitated multi-hour precursor stability, annealing of microgels needed to proceed within 5-10 minutes to minimize time that encapsulated tissue remained outside of media.

Multiple ultraviolet (UV)-mediated photopolymerization strategies were evaluated as detailed in **Appendix Table C.9**. Although certain conditions produced macroscopic gel formation, these were attributed to bulk hydrogel polymerization of added PEG-VS rather than true microgel annealing. Peptide-mediated annealing using additional YKNS (**Appendix Table C.10**) similarly failed to anneal microgels to one another. Strategies involving thrombin, fibrinogen, and factor XIII (FXIII) were also explored (**Appendix Table C.11**). While previously established FXIII-mediated strategies successfully annealed microgels, these required incubation periods of 30 minutes or longer, exceeding the biologically acceptable 5-10 minute window. Thrombin/fibrinogen strategies produced macroscopic gels; however, these were dominated by fibrin polymerization instead of microgel annealing.

Importantly, PEG-VS microgels were intentionally fabricated with excess VS groups in order to preserve reactive functionality for annealing. Despite this, none of the evaluated strategies achieved rapid PEG-VS microgel annealing compatible with live tissue encapsulation. These limitations motivated exploration of an alternative polymer functional group.

C.3 Transition to PEG-MAL

PEG-maleimide (PEG-MAL) was thus introduced as an alternative to PEG-VS, as maleimide groups are more reactive than vinyl sulfone groups, offering the potential for improved kinetic and swelling control as well as microgel annealing. Upon introduction of PEG-MAL, gelation kinetics were systematically re-mapped under both non-reducing and TCEP-stabilized conditions (**Appendix Table C.1–2**). Strong pH dependence was again observed, with highly acidic environments producing multi-hour gelation windows compatible with microfluidic droplet generation. Importantly, swelling characterization of PEG-MAL formulations (**Appendix Table C.7**) demonstrated that delayed gelation at low pH did not necessarily result in excessive swelling relative to the laboratory benchmark.

Subsequent incorporation of RGD functionalization required additional mapping of gelation kinetics and swelling (**Appendix Table C.3, Appendix Table C.8**). Efficient RGD conjugation to PEG-MAL required neutral pH to facilitate maleimide-thiol coupling. Accordingly, PEG-MAL and RGD were first reacted under neutral conditions, after which the solution was acidified prior to the addition of YKNS in order to delay gelation. Collectively, PEG-MAL provided the tunability required to achieve multi-hour precursor stability for microfluidic droplet generation while maintaining acceptable swelling behavior and permitting microgel annealing (**Appendix Table C.9**). For these reasons, PEG-MAL was ultimately selected as the microgel chemistry used for the MAP hydrogels described in Chapter 3.

C.4 Crosslinking Requirements for In Vivo Bulk Controls

In parallel with microgel development, bulk hydrogel formulations were evaluated as controls for in vivo experiments (**Appendix Table C.4**). While microgel fabrication required multi-hour precursor stability, bulk hydrogel encapsulation required complete gelation within 5-

10 minutes to minimize tissue exposure outside of media, similar to the annealing requirement. Although PEG-MAL formulations offered desirable control over gelation kinetics for microfluidic droplet generation, they were not compatible with the rapid gelation and physiological pH conditions required for bulk tissue encapsulation. Conditions that delayed gelation sufficiently for microfluidics relied on acidic environments, which were not compatible with tissue. Conversely, PEG-MAL formulations prepared under neutral conditions formed viscous solutions and gels much faster than the required 5-10 minute window. As a result, PEG-VS chemistry was retained for the bulk in vivo control hydrogels, as described in Chapter 3.

Appendix Table C.1 Gelation Studies Modulating HEPES Buffer pH for both PEG and YKNS Suspensions

Polymer	Polymer %	Polymer Func	Xlinker	Polymer:Xlinker Functional Group Ratio	HEPES pH	Xlinker Solution	t_1	t_2	Notes
8-arm PEG-VS	5%	--	YKNS	1:1 VS:SH	4	HEPES (pH 4)	--	--	remained liquid after overnight incubation at 37°C
8-arm PEG-VS	5%	--	YKNS	1:1 VS:SH	4.5	HEPES (pH 4.5)	--	--	remained liquid after overnight incubation at 37°C
8-arm PEG-VS	5%	--	YKNS	1:1 VS:SH	5	HEPES (pH 5)	--	--	viscous after overnight incubation at 37°C
8-arm PEG-VS	5%	--	YKNS	1:1 VS:SH	5.5	HEPES (pH 5.5)	--	--	formed gel after overnight incubation at 37°C
8-arm PEG-VS	5%	--	YKNS	1:1 VS:SH	6	HEPES (pH 6)	--	--	formed gel after overnight incubation at 37°C
8-arm PEG-VS	5%	--	YKNS	1:1 VS:SH	6.5	HEPES (pH 6.5)	--	--	formed gel after overnight incubation at 37°C
8-arm PEG-VS	5%	--	YKNS	1:1 VS:SH	7	HEPES (pH 7)	7.5 min	8 min	--
8-arm PEG-VS	5%	--	YKNS	1:1 VS:SH	7.4	HEPES (pH 7.4)	4.5 min	5 min	--
4-arm PEG-MAL	5%	--	YKNS	1:1 MAL:SH	7.6	HEPES (pH 7.6)	0 min	0 min	formed gel instantaneously
4-arm PEG-MAL	5%	--	YKNS	16:7 MAL:SH	7.6	HEPES (pH 7.6)	0 min	0 min	formed gel instantaneously
4-arm PEG-MAL	5%	--	YKNS	16:7 MAL:SH	7.6	HEPES (pH 7.6)	0 min	0 min	formed gel instantaneously
4-arm PEG-MAL	5%	--	YKNS	16:7 MAL:SH	6.5	HEPES (pH 6.5)	0 min	0 min	formed gel instantaneously

Polymer Func: polymer functionalization; Xlinker: crosslinker; t_1: onset of viscous behavior, solution sticks to pipette tip; t_2: onset of gel behavior, solution cannot be aspirated into pipette tip. HEPES buffer: 50 mM HEPES, 154 mM NaCl.

Appendix Table C.2 Gelation Studying Modulating HEPES Buffer pH for PEG Suspension and TCEP Concentration for YKNS Suspension

Polymer	Polymer %	Polymer Func	Xlinker	Polymer:Xlinker Functional Group Ratio	HEPES pH	Xlinker Solution	t_1	t_2	Notes
4-arm PEG-MAL	10%	--	YKNS	16:7 MAL:SH	1.5	2.5 mM TCEP in MilliQ	~2 hr	~2 hr	--
4-arm PEG-MAL	10%	--	YKNS	16:7 MAL:SH	3	2.5 mM TCEP in MilliQ	6 min	8 min	--
4-arm PEG-MAL	10%	--	YKNS	16:7 MAL:SH	3.5	2.5 mM TCEP in MilliQ	5 min	7.5 min	--
4-arm PEG-MAL	10%	--	YKNS	16:7 MAL:SH	4	2.5 mM TCEP in MilliQ	4 min	7 min	--
4-arm PEG-MAL	10%	--	YKNS	16:7 MAL:SH	4.5	2.5 mM TCEP in MilliQ	3 min	4.5 min	--
4-arm PEG-MAL	10%	--	YKNS	16:7 MAL:SH	5	2.5 mM TCEP in MilliQ	3 min	4.5 min	--
4-arm PEG-MAL	10%	--	YKNS	16:7 MAL:SH	5.5	2.5 mM TCEP in MilliQ	3 min	4 min	--
4-arm PEG-MAL	10%	--	YKNS	16:7 MAL:SH	6	2.5 mM TCEP in MilliQ	2.5 min	3 min	--
4-arm PEG-MAL	10%	--	YKNS	16:7 MAL:SH	1.5	5 mM TCEP in MilliQ	~1.5 hr	~1.5 hr	--
4-arm PEG-MAL	10%	--	YKNS	16:7 MAL:SH	3	5 mM TCEP in MilliQ	11.5 min	13.5 min	--
4-arm PEG-MAL	10%	--	YKNS	16:7 MAL:SH	3.5	5 mM TCEP in MilliQ	6.5 min	8.5 min	--
4-arm PEG-MAL	10%	--	YKNS	16:7 MAL:SH	4	5 mM TCEP in MilliQ	5 min	6 min	--
4-arm PEG-MAL	10%	--	YKNS	16:7 MAL:SH	4.5	5 mM TCEP in MilliQ	4.5 min	6.5 min	--
4-arm PEG-MAL	10%	--	YKNS	16:7 MAL:SH	5	5 mM TCEP in MilliQ	3.5 min	4 min	--
4-arm PEG-MAL	10%	--	YKNS	16:7 MAL:SH	5.5	5 mM TCEP in MilliQ	3 min	4 min	--
4-arm PEG-MAL	10%	--	YKNS	16:7 MAL:SH	6	5 mM TCEP in MilliQ	2.5 min	3 min	--
8-arm PEG-MAL	10%	--	YKNS	16:7 MAL:SH	1	5 mM TCEP in MilliQ	3 hr 12 min	3 hr 35 min	--
8-arm PEG-MAL	10%	--	YKNS	16:7 MAL:SH	1.5	5 mM TCEP in MilliQ	1 hr 30 min	1 hr 45 min	--
8-arm PEG-MAL	10%	--	YKNS	16:7 MAL:SH	1.78	5 mM TCEP in MilliQ	1 hr 20 min	1 hr 35 min	--
8-arm PEG-MAL	10%	--	YKNS	16:7 MAL:SH	2	5 mM TCEP in MilliQ	43 min	54 min	--
8-arm PEG-MAL	10%	--	YKNS	16:7 MAL:SH	2.5	5 mM TCEP in MilliQ	19 min	24 min	--
8-arm PEG-MAL	10%	--	YKNS	16:7 MAL:SH	3	5 mM TCEP in MilliQ	8 min	9.5 min	--

Polymer Func: polymer functionalization; Xlinker: crosslinker; t_1: onset of viscous behavior, solution sticks to pipette tip; t_2: onset of gel behavior, solution cannot be aspirated into pipette tip. HEPES buffer: 50 mM HEPES, 154 mM NaCl.

Appendix Table C.3 Gelation Studies Modulating RGD Functionalization Concentration
For all conditions, 1N HCl was added to the RGD-functionalized PEG solution to reduce the pH to 1.5 prior to adding the YKNS crosslinker solution.

Polymer	Polymer %	Polymer Func	Xlinker	Polymer:Xlinker Functional Group Ratio	HEPES pH	Xlinker Solution	t_1	t_2	Notes
8-arm PEG-MAL	10%	0.25 mM RGD	YKNS	16:7 MAL:SH	7.4	5 mM TCEP in MilliQ	4 hr 11 min	4 hr 28 min	--
8-arm PEG-MAL	10%	0.50 mM RGD	YKNS	16:7 MAL:SH	7.4	5 mM TCEP in MilliQ	4 hr 52 min	5 hr 18 min	--
8-arm PEG-MAL	10%	0.75 mM RGD	YKNS	16:7 MAL:SH	7.4	5 mM TCEP in MilliQ	5 hr 12 min	5 hr 48 min	--
8-arm PEG-MAL	10%	1.00 mM RGD	YKNS	16:7 MAL:SH	7.4	5 mM TCEP in MilliQ	4 hr 59 min	5 hr 22 min	--

Polymer Func: polymer functionalization; Xlinker: crosslinker; t_1: onset of viscous behavior, solution sticks to pipette tip; t_2: onset of gel behavior, solution cannot be aspirated into pipette tip. HEPES buffer: 50 mM HEPES, 154 mM NaCl.

Appendix Table C.4 Gelation Studies for In Vivo Bulk Hydrogel Control

Polymer	Polymer %	Polymer Func	Xlinker	Polymer:Xlinker Functional Group Ratio	HEPES pH	Xlinker Solution	t_1	t_2	Notes
4-arm PEG-MAL	1%	1.00 mM RGD	YKNS	16:7 MAL:SH	7.4	HEPES (pH 7.4)	--	--	remained liquid by 1.5 hr
4-arm PEG-MAL	2%	1.00 mM RGD	YKNS	16:7 MAL:SH	7.4	HEPES (pH 7.4)	0 min	0 min	formed viscous solution instantaneously
4-arm PEG-MAL	3%	1.00 mM RGD	YKNS	16:7 MAL:SH	7.4	HEPES (pH 7.4)	0 min	0 min	formed gel instantaneously
4-arm PEG-MAL	5%	1.00 mM RGD	YKNS	16:7 MAL:SH	7.4	HEPES (pH 7.4)	0 min	0 min	formed gel instantaneously
8-arm PEG-MAL	1%	1.00 mM RGD	YKNS	16:7 MAL:SH	7.4	HEPES (pH 7.4)	--	--	remained liquid by 1.5 hr
8-arm PEG-MAL	2%	1.00 mM RGD	YKNS	16:7 MAL:SH	7.4	HEPES (pH 7.4)	0 min	0 min	formed viscous solution instantaneously
8-arm PEG-MAL	3%	1.00 mM RGD	YKNS	16:7 MAL:SH	7.4	HEPES (pH 7.4)	0 min	0 min	formed gel instantaneously
8-arm PEG-MAL	5%	1.00 mM RGD	YKNS	16:7 MAL:SH	7.4	HEPES (pH 7.4)	0 min	0 min	formed gel instantaneously
4-arm PEG-MAL	3%	1.00 mM RGD	YKNS	16:7 MAL:SH	7.8	5 mM TCEP in MilliQ	0 min	0 min	formed gel instantaneously
8-arm PEG-MAL	3%	1.00 mM RGD	YKNS	16:7 MAL:SH	7.8	5 mM TCEP in MilliQ	0 min	0 min	formed gel instantaneously
4-arm PEG-MAL	3%	1.00 mM RGD	VPMS	1:1 MAL:SH	7.4	HEPES (pH 7.4)	0 min	0 min	formed viscous solution instantaneously
4-arm PEG-MAL	5%	1.00 mM RGD	VPMS	1:1 MAL:SH	7.4	HEPES (pH 7.4)	0 min	0 min	formed viscous solution instantaneously
8-arm PEG-MAL	3%	1.00 mM RGD	VPMS	1:1 MAL:SH	7.4	HEPES (pH 7.4)	0 min	0 min	formed viscous solution instantaneously
8-arm PEG-MAL	5%	1.00 mM RGD	VPMS	1:1 MAL:SH	7.4	HEPES (pH 7.4)	0 min	0 min	formed viscous solution instantaneously
8-arm PEG-MAL	5%	1.00 mM RGD	VPMS	16:7 MAL:SH	7.4	HEPES (pH 7.4)	0 min	0 min	formed viscous solution instantaneously
8-arm PEG-VS	5%	1.00 mM RGD	YKNS	1:1 VS:SH	7.4	HEPES (pH 7.4)	--	30 min	--

8-arm PEG-VS	7%	1.00 mM RGD	YKNS	1:1 VS:SH	7.4	HEPES (pH 7.4)	--	30 min	--
8-arm PEG-VS	10%	1.00 mM RGD	YKNS	1:1 VS:SH	7.4	HEPES (pH 7.4)	--	30 min	--
8-arm PEG-VS	5%	1.00 mM RGD	YKNS	1:1 VS:SH	7.8	HEPES (pH 7.8)	--	18 min	formed gel-like product, difficult to manually handle
8-arm PEG-VS	5%	1.00 mM RGD	YKNS	1:1 VS:SH	7.8	HEPES (pH 7.8)	4 min	5 min	formed gel-like product, difficult to manually handle*
8-arm PEG-VS	7%	1.00 mM RGD	YKNS	1:1 VS:SH	7.8	HEPES (pH 7.8)	--	19 min	formed gel-like product, difficult to manually handle
8-arm PEG-VS	7%	1.00 mM RGD	YKNS	1:1 VS:SH	7.8	HEPES (pH 7.8)	4 min	5 min	formed gel-like product, difficult to manually handle*
8-arm PEG-VS	5%	0.75 mM RGD	YKNS	1:1 VS:SH	7.6	HEPES (pH 7.6)	5 min	13 min	formed gel-like product, difficult to manually handle
8-arm PEG-VS	7%	0.75mM RGD	YKNS	1:1 VS:SH	7.6	HEPES (pH 7.6)	5 min	10 min	--

Polymer Func: polymer functionalization; Xlinker: crosslinker; t_1: onset of viscous behavior, solution sticks to pipette tip; t_2: onset of gel behavior, solution cannot be aspirated into pipette tip. HEPES buffer: 50 mM HEPES, 154 mM NaCl.

*Gel allowed to crosslink on a 37ºC heating stage.

Appendix Table C.5 Swelling Ratios of PEG-VS Hydrogels as a Function of HEPES Buffer pH

Polymer	Polymer %	Polymer Func	Xlinker	Polymer:Xlinker Functional Group Ratio	HEPES pH	Xlinker Solution	Swelling Ratio t_1 (Mean± SD)	Swelling Ratio t_2 (Mean± SD)
8-arm PEG-VS	5%	--	YKNS	1:1 VS:SH	6	HEPES (pH 6)	47 ± 2	--
8-arm PEG-VS	5%	--	YKNS	1:1 VS:SH	6.5	HEPES (pH 6.5)	27 ± 1	--
8-arm PEG-VS	5%	--	YKNS	1:1 VS:SH	7.4	HEPES (pH 7.4)	28 ± 2	--

Polymer Func: polymer functionalization; Xlinker: crosslinker; t_1: swelling ratio of gels formed by immediately mixing component solutions upon suspending PEG and YKNS into respective solutions; t_2: swelling ratio of gels formed by mixing component solutions 90 minutes after suspending PEG and YKNS into respective solutions. HEPES buffer: 50 mM HEPES, 154 mM NaCl.

Appendix Table C.6 Swelling Ratios of PEG-VS Hydrogels as a Function of HEPES Buffer pH and TCEP Concentration

Polymer	Polymer %	Polymer Func	Xlinker	Polymer:Xlinker Functional Group Ratio	HEPES pH	Xlinker Solution	Swelling Ratio t_1 (Mean± SD)	Swelling Ratio t_2 (Mean± SD)
8-arm PEG-VS	5%	--	YKNS	1:1 VS:SH	7.4	5 mM TCEP in Milli-Q	77 ± 13	69 ± 9
8-arm PEG-VS	5%	--	YKNS	1:1 VS:SH	7.6	5 mM TCEP in Milli-Q	53 ± 4	62 ± 3
8-arm PEG-VS	5%	--	YKNS	1:1 VS:SH	7.7	5 mM TCEP in Milli-Q	50 ± 5*	46 ± 6*
8-arm PEG-VS	5%	--	YKNS	1:1 VS:SH	7.6	2.5 mM TCEP in Milli-Q	34 ± 3	32 ± 2
8-arm PEG-VS	5%	--	YKNS	1:1 VS:SH	7.6	3.5 mM TCEP in Milli-Q	55 ± 4	48 ± 4

Polymer Func: polymer functionalization; Xlinker: crosslinker; t_1: swelling ratio of gels formed by immediately mixing component solutions upon suspending PEG and YKNS into respective solutions; t_2: swelling ratio of gels formed by mixing component solutions 90 minutes after suspending PEG and YKNS into respective solutions. HEPES buffer: 50 mM HEPES, 154 mM NaCl.

*Gel formed too quickly to be used in microfluidic device for droplet generation.

Appendix Table C.7 Swelling Ratios of PEG-MAL Hydrogels as a Function of HEPS Buffer pH

Polymer	Polymer %	Polymer Func	Xlinker	Polymer:Xlinker Functional Group Ratio	HEPES pH	Xlinker Solution	Swelling Ratio t_1 (Mean± SD)	Swelling Ratio t_2 (Mean± SD)
8-arm PEG-MAL	10%	--	YKNS	16:7 MAL:SH	1	5 mM TCEP in Milli-Q	25 ± 2	--
8-arm PEG-MAL	10%	--	YKNS	16:7 MAL:SH	1.5	5 mM TCEP in Milli-Q	27 ± 3	--

Polymer Func: polymer functionalization; Xlinker: crosslinker; t_1: swelling ratio of gels formed by immediately mixing component solutions upon suspending PEG and YKNS into respective solutions; t_2: swelling ratio of gels formed by mixing component solutions 90 minutes after suspending PEG and YKNS into respective solutions. HEPES buffer: 50 mM HEPES, 154 mM NaCl.

Appendix Table C.8 Swelling Ratios of PEG-MAL Hydrogels as a Function of RGD Functionalization Concentration
For all conditions, 1N HCl was added to the RGD-functionalized PEG solution to reduce the pH to 1.5 prior to adding the YKNS crosslinker solution.

Polymer	Polymer %	Polymer Func	Xlinker	Polymer:Xlinker Functional Group Ratio	HEPES pH	Xlinker Solution	Swelling Ratio t_1 (Mean± SD)	Swelling Ratio t_2 (Mean± SD)
8-arm PEG-MAL	10%	0.25 mM RGD	YKNS	16:7 MAL:SH	7.4	5 mM TCEP in Milli-Q	28 ± 2	--
8-arm PEG-MAL	10%	0.50 mM RGD	YKNS	16:7 MAL:SH	7.4	5 mM TCEP in Milli-Q	35 ± 3	--
8-arm PEG-MAL	10%	0.75 mM RGD	YKNS	16:7 MAL:SH	7.4	5 mM TCEP in Milli-Q	38 ± 3	--
8-arm PEG-MAL	10%	1.00 mM RGD	YKNS	16:7 MAL:SH	7.4	5 mM TCEP in Milli-Q	32 ± 3	--

Polymer Func: polymer functionalization; Xlinker: crosslinker; t_1: swelling ratio of gels formed by immediately mixing component solutions upon suspending PEG, RGD, and YKNS into respective solutions; t_2: swelling ratio of gels formed by mixing component solutions 90 minutes after suspending PEG, RGD, and YKNS into respective solutions. HEPES buffer: 50 mM HEPES, 154 mM NaCl.

Appendix Table C.9 Ultraviolet (UV)-Mediated Annealing Strategies

Polymer	Polymer %	Xlinker	Polymer:Xlinker Functional Group Ratio	UV Solution	Microgel:UV Solution Volume Ratio	Microgel Isolation Method	UV Exposure Time	Outcome
8-arm PEG-VS	5%	YKNS	1:1 VS:SH	0.4% Irgacure, 0.1% NVP	1:4	Centrifuge microgel-UV solution, 500 xg, 3 min	6, 12, 18 min	No
8-arm PEG-VS	5%	YKNS	1:1 VS:SH	0.4% Irgacure, 0.1% NVP	1:199	Centrifuge microgels, 5000 xg, 5 min; Centrifuge microgel-UV solution, 3000 xg, 5 min	6, 12 min	No
8-arm PEG-VS	5%	YKNS	1:1 VS:SH	0.4% Irgacure, 0.1% NVP	1:199, 1:49, 1:39, 1:19	--	6 min	No
8-arm PEG-VS	5%	YKNS	1:1 VS:SH	600 mg/mL Irgacure in NVP	1:1	Vacuum chamber drying	6 min	No
8-arm PEG-VS	5%	YKNS	1:0.8 VS:SH	600 mg/mL Irgacure in NVP	1:1	Vacuum chamber drying	6 min	No
8-arm PEG-VS	5%	YKNS	1:0.8 VS:SH	A: 600 mg/mL Irgacure in NVP; B: 0.4% Irgacure, 0.1% NVP, 1% 8-arm PEG-VS	8:1:1 (microgel:A:B)	--	6 min	No
8-arm PEG-VS	5%	YKNS	1:0.8 VS:SH	A: 600 mg/mL Irgacure in NVP; B: 0.4% Irgacure, 0.1% NVP, 5% 8-arm PEG-VS	8:1:1 (microgel:A:B)	--	6 min	Yes*
8-arm PEG-VS	5%	YKNS	1:0.8 VS:SH	A: 600 mg/mL Irgacure in NVP; B: 0.4% Irgacure, 0.1% NVP, 20% 8-arm PEG-VS	8:1:1 (microgel:A:B)	--	6 min	Yes*
8-arm PEG-VS	5%	YKNS	1:0.8 VS:SH	A: 600 mg/mL Irgacure in NVP; B: 0.4% Irgacure, 0.1% NVP, 50% 8-arm PEG-VS	8:1:1 (microgel:A:B)	--	6 min	Yes*
8-arm PEG-VS	5%	YKNS	1:0.8 VS:SH	A: 600 mg/mL Irgacure in NVP; B: 0.4% Irgacure, 0.1% NVP, 1% 4-arm PEG-VS	8:1:1 (microgel:A:B)	--	6 min	No
8-arm PEG-VS	5%	YKNS	1:0.8 VS:SH	A: 600 mg/mL Irgacure in NVP; B: 0.4% Irgacure, 0.1% NVP, 5% 4-arm PEG-VS	8:1:1 (microgel:A:B)	--	6 min	No
8-arm PEG-VS	5%	YKNS	1:0.8 VS:SH	A: 600 mg/mL Irgacure in NVP; B: 0.4% Irgacure, 0.1% NVP, 20% 4-arm PEG-VS	8:1:1 (microgel:A:B)	--	6 min	Yes*
8-arm PEG-VS	5%	YKNS	1:0.8 VS:SH	A: 600 mg/mL Irgacure in NVP; B: 0.4% Irgacure, 0.1% NVP, 50% 4-arm PEG-VS	8:1:1 (microgel:A:B)	--	6 min	Yes*

8-arm PEG-VS	5%	YKNS	1:0.8 VS:SH	600 mg/mL Irgacure in NVP	99:1	Vacuum chamber drying	6 min	No
8-arm PEG-VS	5%	YKNS	1:0.8 VS:SH	600 mg/mL Irgacure in NVP	9:1	Vacuum chamber drying	6 min	No
4-arm PEG-MAL	10%	YKNS	16:7 MAL:SH	600 mg/mL Irgacure in NVP	9:1	Centrifuge microgels, 10 000 xg, 8 min	3 min	Yes
8-arm PEG-VS	10%	YKNS	1:0.6 VS:SH	600 mg/mL Irgacure in NVP	9:1	Centrifuge microgels, 10 000 xg, 8 min	3 min	No
8-arm PEG-VS	10%	YKNS	1:0.6 VS:SH	600 mg/mL Irgacure in NVP	9:1	Centrifuge microgels, 18 000 xg, 5 min	3 min	No
4-arm PEG-MAL	10%	YKNS	16:7 MAL:SH	600 mg/mL Irgacure in NVP	9:1	Centrifuge microgels, 18 000 xg, 5 min	3 min	Yes

Xlinker: crosslinker; NVP: 1-Vinyl-2-pyrrolidinone. UV Exposure: $\lambda = 365$ nm, 1090 $\mu W/cm^2$. Outcome of "No" indicates no microgel annealing occurred.

*Although a gel formed, it was mostly a bulk hydrogel due to the addition of PEG into UV solution B.

Appendix Table C.10 Peptide-Mediated Annealing Strategies

Polymer	Polymer %	Xlinker	Polymer:Xlinker Functional Group Ratio	Peptide Solution	Microgel:Peptide Solution Volume Ratio	Microgel Isolation Method	Outcome
8-arm PEG-VS	5%	YKNS	1:0.8 VS:SH	YKNS (6.74 mM)	1:2	Centrifuge microgels, 3000 xg	No
8-arm PEG-VS	5%	YKNS	1:0.8 VS:SH	YKNS (6.74 mM)	1:1	Centrifuge microgels, 3000 xg, followed by vacuum chamber drying	No
8-arm PEG-VS	5%	YKNS	1:0.8 VS:SH	A: YKNS (5.33 mM)*; B: 1% 8-arm PEG-VS	8:1:1 (microgel:A:B)	--	No
8-arm PEG-VS	5%	YKNS	1:0.8 VS:SH	A: YKNS (5.33 mM)*; B: 5% 8-arm PEG-VS	8:1:1 (microgel:A:B)	--	No
8-arm PEG-VS	5%	YKNS	1:0.8 VS:SH	A: YKNS (5.33 mM)*; B: 20% 8-arm PEG-VS	8:1:1 (microgel:A:B)	--	No
8-arm PEG-VS	5%	YKNS	1:0.8 VS:SH	A: YKNS (5.33 mM)*; B: 50% 8-arm PEG-VS	8:1:1 (microgel:A:B)	--	No
8-arm PEG-MAL	10%	YKNS	16:7 MAL:SH	YKNS (146 mM)**	31:1	Centrifuge microgels, 18 000 xg, 5 min	No
8-arm PEG-MAL	10%	YKNS	16:7 MAL:SH	YKNS***	--	Centrifuge microgels, 18 000 xg, 5 min	No

Xlinker: crosslinker. Outcome of "No" indicates no microgel annealing occurred.

*YKNS molarity theoretically results in 1:1 VS:SH ratio with leftover VS groups on PEG microgels.
**YKNS molarity theoretically results in 1:1 MAL:SH ratio with leftover MAL groups on PEG microgels.
***Microgels added directly to lyophilized YKNS aliquot at a resulting theoretical 1:1 MAL:SH ratio with leftover MAL groups on PEG microgels.

Appendix Table C.11 Thrombin-. Fibrinogen-. and Factor XIII-Mediated Annealing Strategies

Polymer	Polymer %	Polymer Func	Xlinker	Polymer:Xlinker Functional Group Ratio	Solution 1	Solution 2	Solution Volume Ratio	Microgel Isolation Method	Outcome
8-arm PEG-VS	5%	250 uM K peptide, 250 uM Q peptide	YKNS	1:0.8 VS:SH	Thrombin (2 U/mL) in microgels	Fibrinogen (10 mg/mL) in microgels	1:1	--	Yes*
8-arm PEG-VS	5%	250 uM K peptide, 250 uM Q peptide	YKNS	1:0.8 VS:SH	Thrombin (1 U/mL) in microgels	--	--	--	No
8-arm PEG-VS	5%	250 uM K peptide, 250 uM Q peptide	YKNS	1:0.8 VS:SH	Thrombin (2 U/mL) in microgels	--	--	--	No
8-arm PEG-VS	5%	250 uM K peptide, 250 uM Q peptide	YKNS	1:0.8 VS:SH	Thrombin (5 U/mL) in microgels	--	--	--	No
8-arm PEG-VS	5%	250 uM K peptide, 250 uM Q peptide	YKNS	1:0.8 VS:SH	Thrombin (2 U/mL) in microgels	Fibrinogen (10 mg/mL) in microgels	1:1	--	Yes*
8-arm PEG-VS	5%	250 uM K peptide, 250 uM Q peptide	YKNS	1:0.8 VS:SH	Thrombin (2 U/mL) in microgels	Fibrinogen (5 mg/mL) in microgels	1:1	--	Yes*
8-arm PEG-VS	5%	250 uM K peptide, 250 uM Q peptide	YKNS	1:0.8 VS:SH	Thrombin (2 U/mL) in microgels	Fibrinogen (2 mg/mL) in microgels	1:1	--	Yes*
8-arm PEG-VS	5%	250 uM K peptide, 250 uM Q peptide	YKNS	1:0.8 VS:SH	Thrombin (4 U/mL) in microgels	Fibrinogen (2 mg/mL) in microgels	1:1	--	Yes*
8-arm PEG-VS	5%	250 uM K peptide, 250 uM Q peptide	YKNS	1:0.8 VS:SH	Thrombin (4 U/mL) in microgels	Fibrinogen (5 mg/mL) in microgels	1:1	--	Yes*
8-arm PEG-VS	5%	250 uM K peptide, 250 uM Q peptide	YKNS	1:0.8 VS:SH	Thrombin (2 U/mL) in microgels	FXIII (10 U/mL) in microgels	1:1	Centrifuge microgels, 18 000 xg, 5 min	Yes
8-arm PEG-VS	5%	250 uM K peptide, 250 uM Q peptide	YKNS	1:0.8 VS:SH	Thrombin (1 U/mL) and FXIII (5 U/mL) in microgels	--	--	Centrifuge microgels, 18 000 xg, 5 min	Yes
8-arm PEG-VS	5%	250 uM K peptide, 250 uM Q peptide	YKNS	1:0.8 VS:SH	Thrombin (2 U/mL) and FXIII (5 U/mL) in microgels	--	--	Centrifuge microgels, 18 000 xg, 5 min	Yes
8-arm PEG-VS	5%	500 uM k peptide, or 500 uM Q peptide	YKNS	1:0.8 VS:SH	Thrombin (4 U/mL) and FXIII (10 U/mL) in K microgels	Thrombin (4 U/mL) and FXIII (10 U/mL) in Q microgels	1:1	Centrifuge microgels, 18 000 xg, 5 min	Yes

Polymer Func: polymer functionalization; Xlinker: crosslinker. Outcome of "No" indicates no microgel annealing occurred.

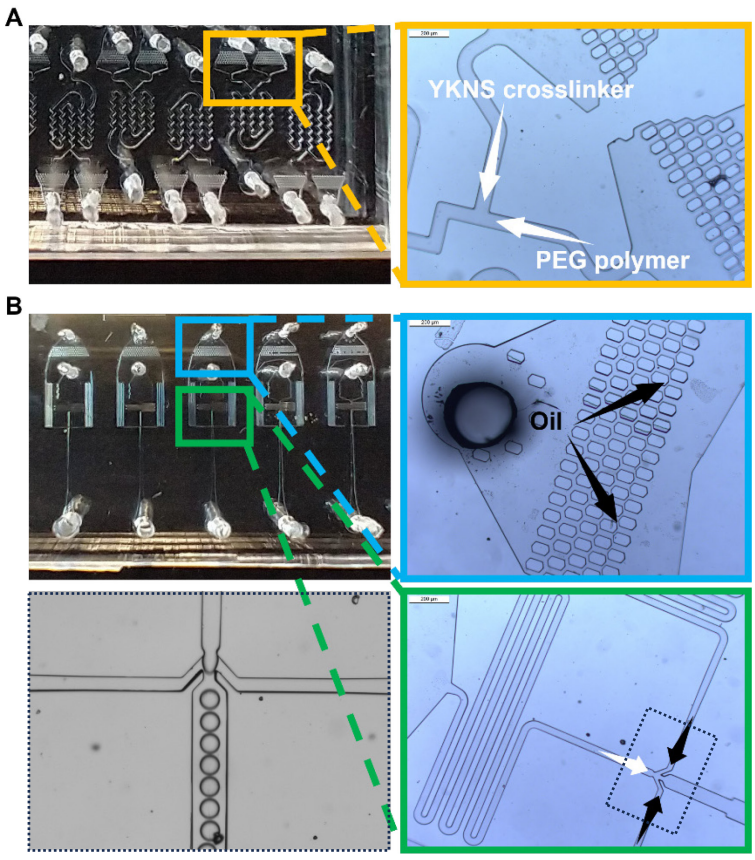
*Although a gel formed, it was mostly a fibrin gel.

Appendix D: Microfluidic Device Screening

Microfluidic droplet generation was evaluated using multiple platforms over the course of hydrogel formulation development. All platforms shared the same objective: high-throughput production of monodisperse microgels.

D.1 Mixing and Droplet Generation Microfluidic Devices

The first platform, provided by the Baker Lab, consisted of two microfluidic devices connected in series with the first device serving as a mixing chip and the second device serving as a downstream flow-focusing droplet generator. To use this platform, PEG and YKNS solutions were loaded into separate syringes and introduced into the mixing device through independent inlets (**Appendix Figure D.1, A**). The mixed precursor solution was then transferred via tubing into the second chip containing a flow-focusing junction where the aqueous hydrogel precursor phase was pinched into droplets by a

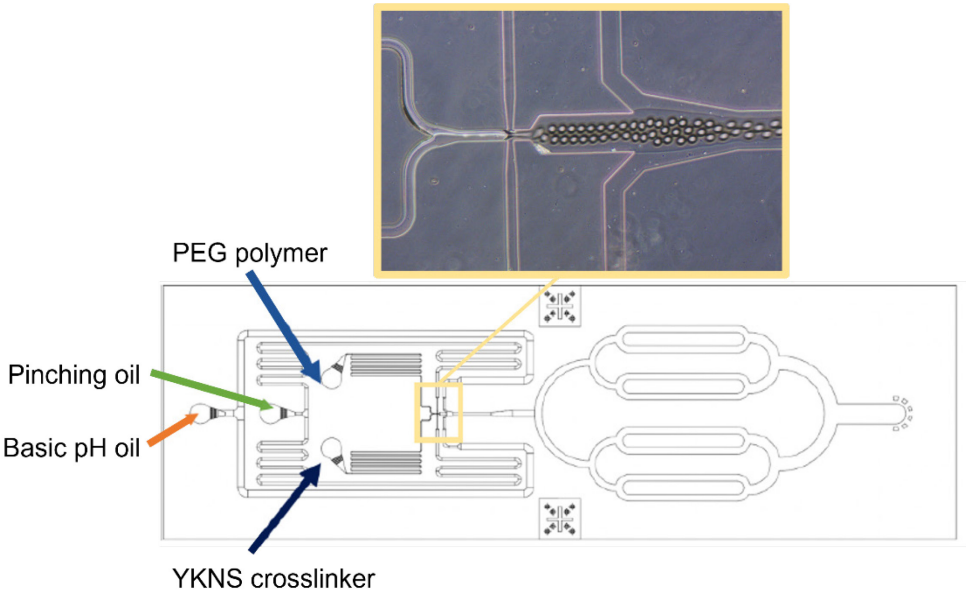


Appendix Figure D.1. Mixing **(A)** and droplet generation **(B)** microfluidic devices. Scale bars = 200 µm.

continuous oil phase (**Appendix Figure D.1, B**). While this platform produced monodisperse microgels, increases in precursor viscosity over time reduced droplet formation stability, limiting the high-throughput production of microgels.

D.2 Integrated Mixing and Droplet Generation Microfluidic Device

The second platform, provided by the Segura Lab, integrated mixing and droplet generation on a single chip (**Appendix Figure D.2**). PEG and YKNS were introduced through separate inlets and combined at a channel intersection immediately upstream of a flow-focusing junction. Following droplet formation, droplets traveled through a slightly basic oil phase intended to modulate droplet pH and crosslinking kinetics. Although this design reduced residence time between mixing and droplet generation, droplet stability remained highly sensitive to flow rates and precursor viscosity. As with the first platform, progressive increases in hydrogel precursor solution viscosity compromised long-term droplet production, limiting reliable high-throughput microgel fabrication.



Appendix Figure D.2. Integrated mixing and droplet generation microfluidic device.

D.3 Step Emulsification Microfluidic Device

As sustained high-throughput droplet generation could not be reliably achieved with flow-focusing configurations, a step emulsification microfluidic device was ultimately selected (see Chapter 3). High-throughput production was essential because encapsulation of whole ovarian tissue pieces required generation of large volumes of microgels to form MAP hydrogel constructs. Step emulsification enabled faster droplet generation and reduced sensitivity to narrow flow rate regimes required for stable droplet formation in flow-focusing systems. Overall, the improved robustness and ease of setup made the step emulsification platform preferable for large-scale microgel fabrication.

Appendix E: Pilot Human Ovarian Tissue Cultures

In collaboration with the Baker Lab, we explored whether resident ovarian endothelial cell outgrowth could be encouraged in vitro as a means to improve vascular integration of transplanted human ovarian tissue. Specifically, we sought to determine whether short-term preculture could promote the outgrowth and formation of ovarian tissue-derived vessels capable of subsequent anastomosis with host vasculature post-transplantation. To assess this, human ovarian tissue cubes were encapsulated in either fibrin-only gels or microgel-fibrin composites and cultured under static or rocking conditions. These pilot studies were conducted as preliminary feasibility experiments.

E.1 Methods and Materials Summary

Cryopreserved human ovarian cortex was thawed and processed into ~ 1x1x1 mm tissue cubes as described in Chapter 3. Tissue cubes were encapsulated into one of three gel conditions: (1) fibrin-only, (2) microgel-fibrin composite, or (3) functionalized microgel-fibrin composite. Across all conditions, fibrin gels were prepared using 5 mg/mL fibrinogen and 1 U/mL thrombin. Microgels were composed of dextran-vinyl sulfone (DEX-VS) crosslinked with dithiol PEG. For the functionalized condition, 10% of the microgel population consisted of DEX-VS microgels functionalized with methacrylated heparin (HepMA). Tissue cubes were encapsulated at one tissue cube per 20 µL of gel. Encapsulated tissues were then cultured within PDMS gaskets placed in 12-well plates, with two gels per well and 1 mL of culture medium per well. Culture medium was prepared as described by Machlin et al.[115], supplemented with 100 ng/mL VEGF-

165 and 100 µg/mL Primocin. Cultures were maintained at 37°C and 5% CO_2 under either static or rocking conditions. Fifty percent of the culture medium was replaced every 48 hours. Tissue constructs were fixed at either 3 or 7 days and then processed for immunofluorescence imaging.

E.2 Fibrin and Microgel-Fibrin Culture: Brightfield Observations

Brightfield imaging demonstrated cellular outgrowth from human ovarian tissue as early as day 3 in both fibrin-only and microgel-fibrin constructs (**Appendix Figure E.1, A–B**). Consistent with the known heterogeneity of human ovarian tissue, this initial day 3 outgrowth was not uniform across all tissue surfaces. By day 7, however, additional regions of the tissues exhibited cellular outgrowth into the surrounding scaffold. Fibrin degradation was evident over time and appeared more pronounced under rocking conditions. This degradation likely also occurred in the microgel-containing constructs but was less readily visualized due to the presence of microgels. In microgel-fibrin constructs, cellular outgrowth appeared to follow paths defined by microgel organization. In contrast, fibrin-only gels showed less organized outgrowth which occasionally followed along degrading fibrin edges.

E.3 Fibrin Culture: Confocal Observations

Confocal imaging of fibrin-only constructs (**Appendix Figure E.2**) stained for F-actin and CD31 revealed that the majority of outgrowth was only F-actin positive. CD31 staining was limited and primarily localized to the tissue rather than the outgrowth. In static cultures, isolated $CD31^+$ staining was observed in tissue-derived outgrowth. Across both brightfield and confocal images, rocking did not appear to promote overall outgrowth or endothelial cell participation.

E.4 Microgel-Fibrin Culture: Confocal Observations

In microgel-fibrin constructs, confocal imaging (**Appendix Figure E.3**) confirmed that cellular outgrowth aligned along microgel-defined channels. Similar to the fibrin-only condition,

most outgrowth was only F-actin positive. CD31 staining remained limited and confined to the tissue except in the day 3 static condition, where $CD31^+$ outgrowth was observed wrapping around a microgel. By day 7, CD31 was still present within the tissue but was less apparent.

E.5 Heparin-Functionalized Microgels: Brightfield Observations

To enhance angiogenic signaling, a subset of microgels was functionalized with heparin. In brightfield imaging (**Appendix Figure E.4**), cellular outgrowth was again observed on day 3 and continued to increase by day 7. Interestingly, culture under rocking appeared to produce a dense cloud of cellular outgrowth proximal to the tissue.

E.6 Heparin-Functionalized Microgels: Confocal Observations

Confocal imaging of the functionalized constructs (**Appendix Figure E.5**) revealed more consistent $CD31^+$ staining under static culture compared to previous culture conditions. In the day 3 static condition, $CD31^+$ cells were observed wrapping around microgels. By day 7, $CD31^+$ staining was observed around the microgels not only near the tissue periphery but also further into the scaffold. In rocking conditions, $CD31^+$ staining was minimal and confined to the tissue.

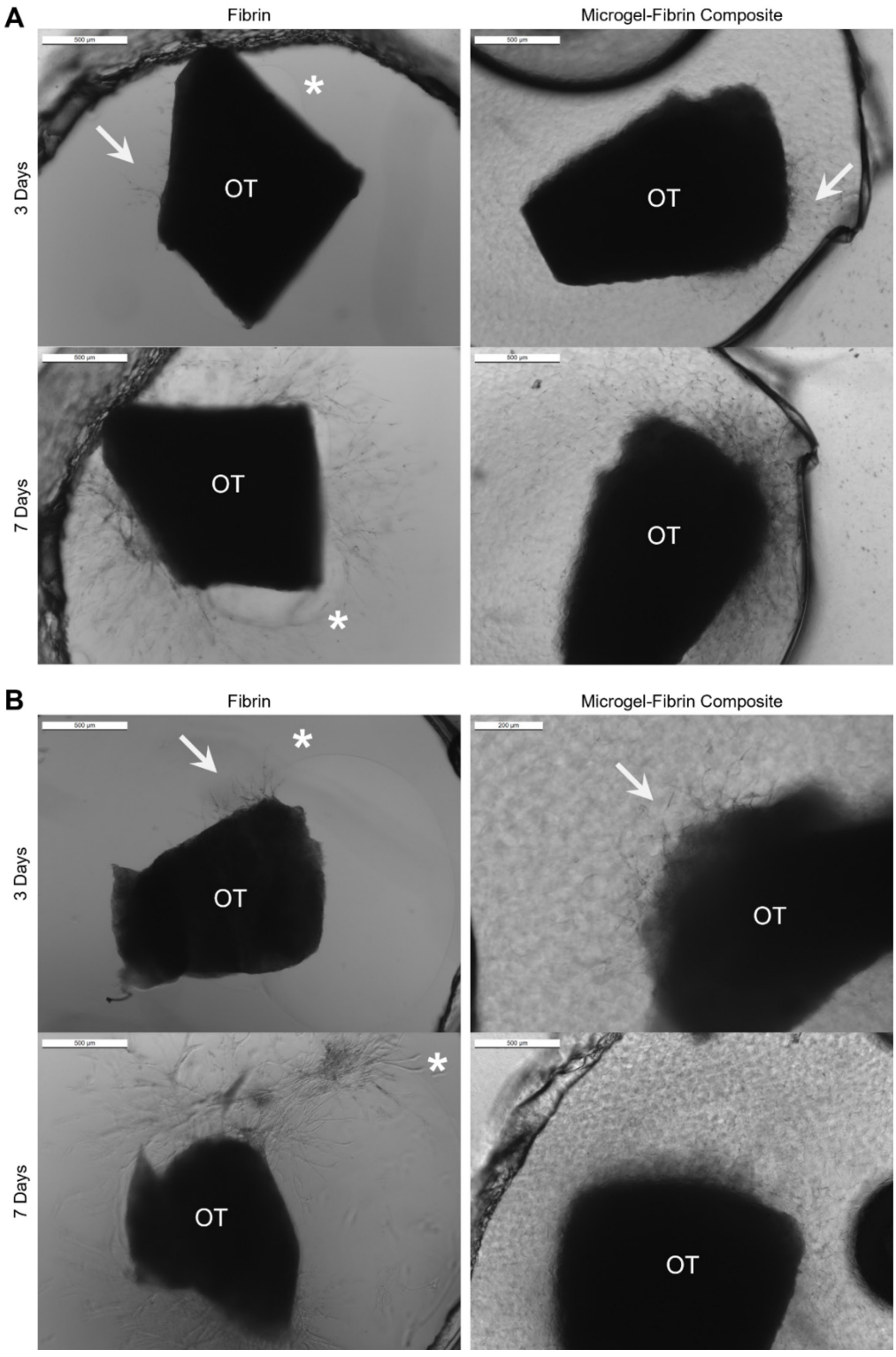
E.7 Overall Interpretation and Limitations

Across all conditions, outgrowth appeared to be dominated by F-actin positive cells, consistent with stromal or fibroblast-like migration. Endothelial cell outgrowth, as assessed by CD31 staining, was present but limited and variable. In fibrin-only and non-functionalized microgel-fibrin constructs, CD31 staining was more apparent on day 3 and less evident on 7, raising the possibility of vascular regression, similar to the phenomenon described in Chapter 3. In contrast, static cultures containing heparin-functionalized microgels demonstrated more sustained CD31 staining through day 7, suggesting that this combination may present a promising direction for further optimization. While we had hypothesized that rocking would

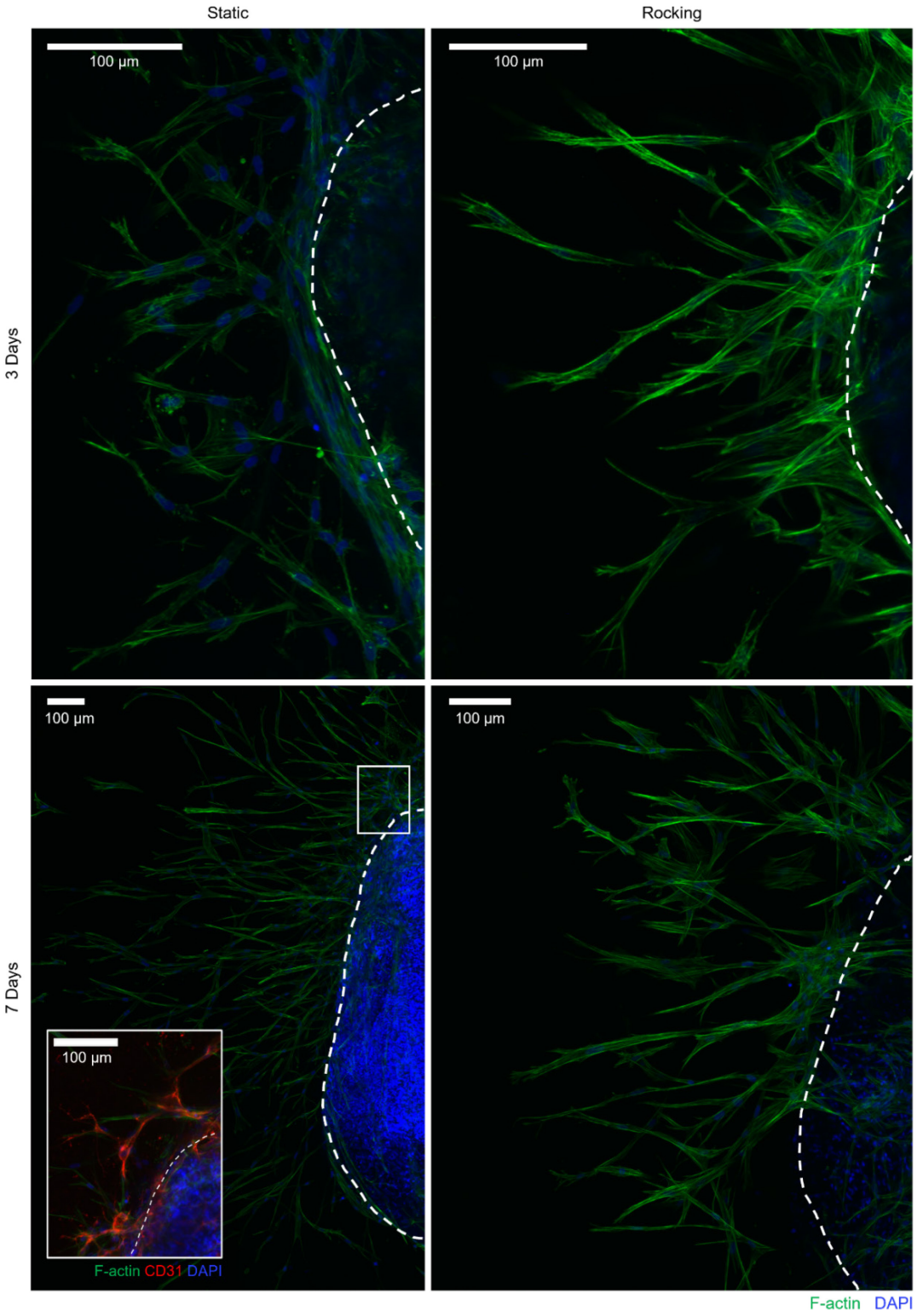
support the formation of mature vessel networks, rocking did not appear to consistently promote cellular outgrowth or vascular network formation. Instead, in this culture system, rocking introduced bulk media movement without defined perfusion channels and it is possible that such agitation disrupted local concentration gradients of tissue-secreted factors necessary for directed migration and endothelial extension.

Although $CD31^+$ outgrowth was observed, especially in the functionalized microgel condition, the overall magnitude of endothelial cell extension was insufficient to generate robust vascular networks within the evaluated timeframe. Given concerns regarding prolonged preculture and the potential for necrotic core formation, early time points such as day 3 represent a key target for future work.

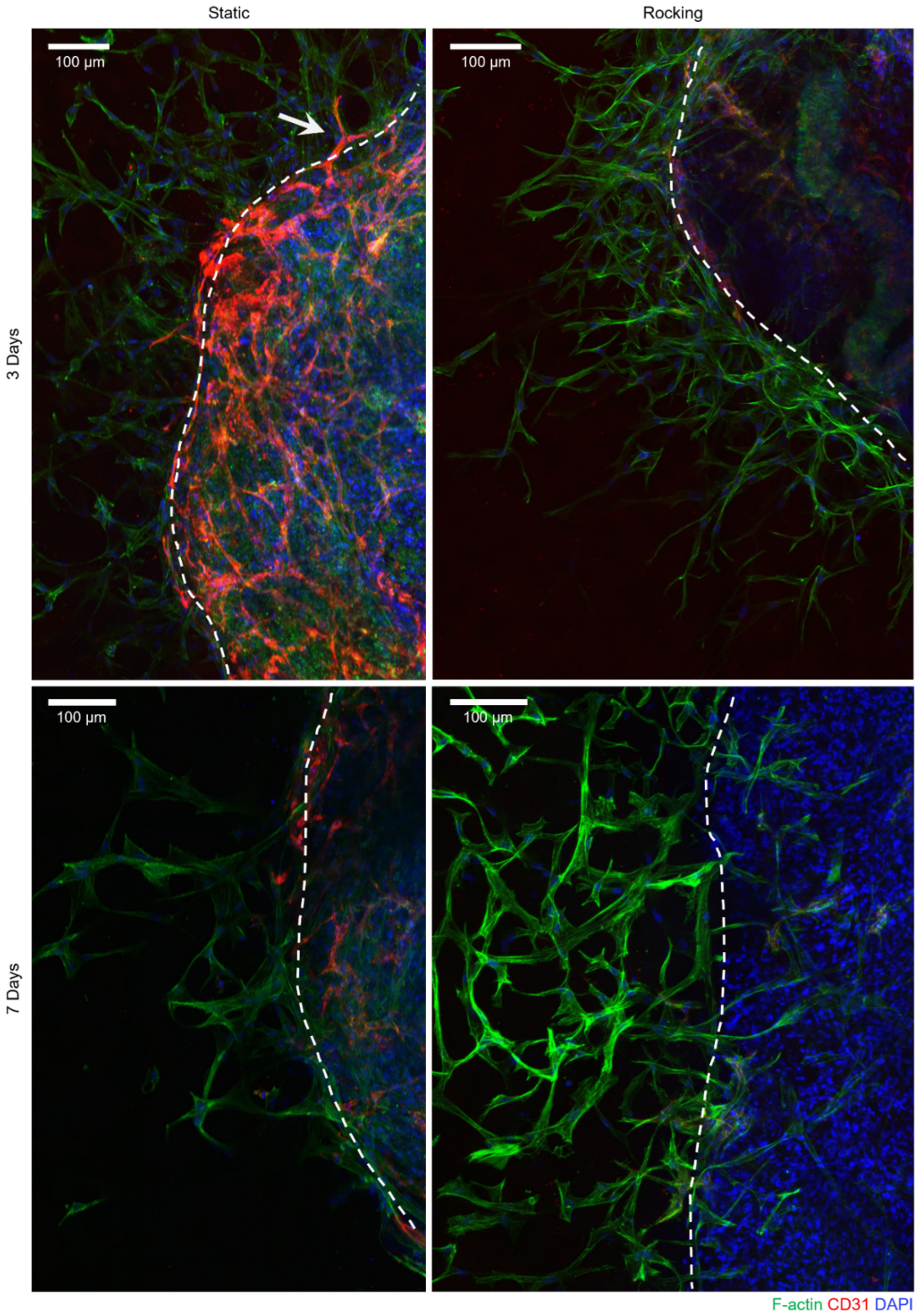
Overall, these studies were preliminary and qualitative in nature. Human ovarian tissue is inherently heterogeneous and larger sample sizes will be required to determine whether the observed trends are reproducible across donors and tissue fragments. Additionally, staining protocols, imaging parameters, and quantitative metrics of cellular outgrowth and endothelial extension will need to be standardized to enable robust comparisons across conditions. Systematic evaluation of post-implantation vascular dynamics and graft survival will be necessary to determine whether this preculture approach improves the balance between rapid revascularization and long-term vascular stability following human ovarian tissue transplantation.



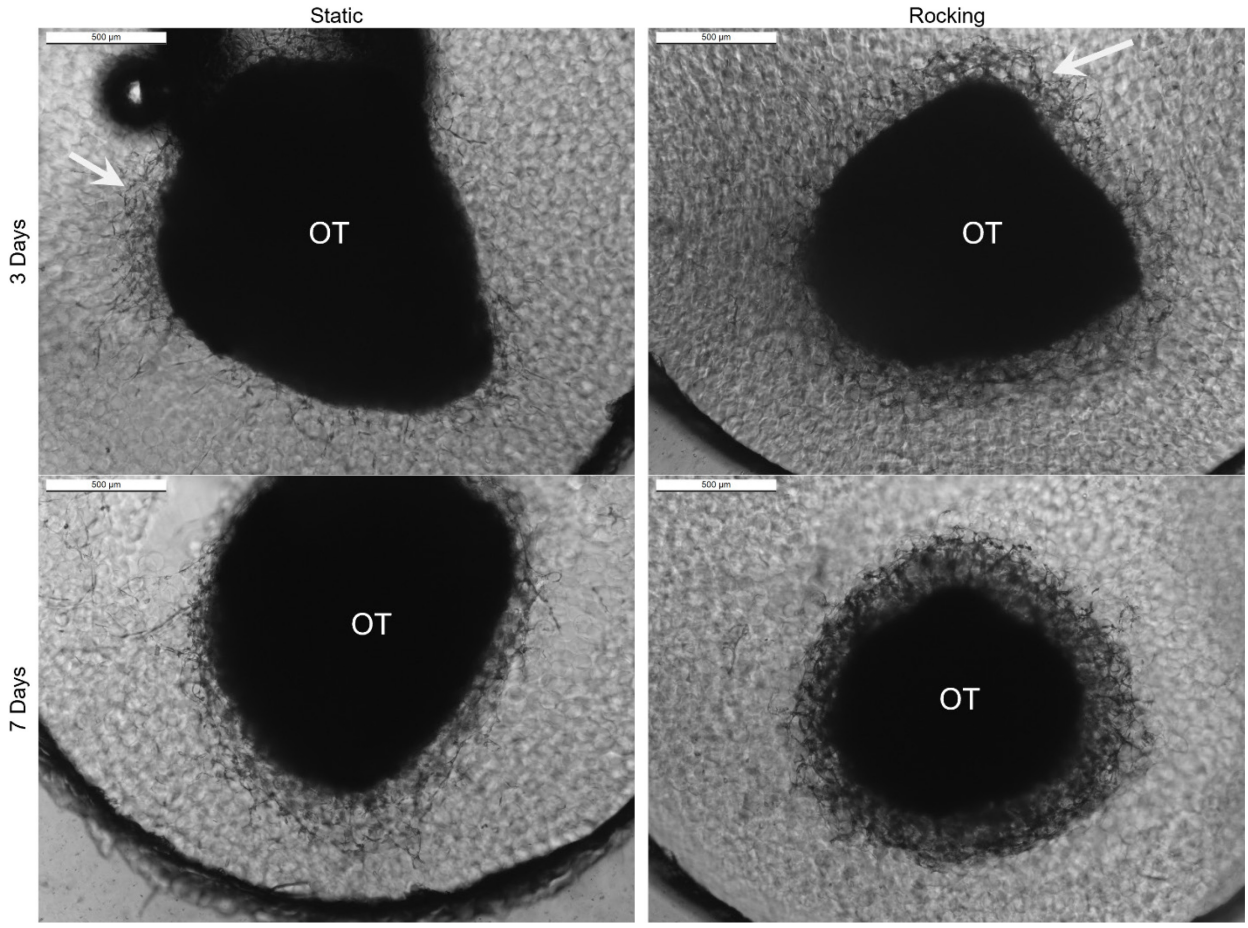
Appendix Figure E.1 Brightfield images of human ovarian tissue encapsulated in fibrin-only gels or microgel-fibrin composites and cultured under static **(A)** or rocking **(B)** conditions for 3 and 7 days. Cellular outgrowth from tissue fragments is visible as early as Day 3 (white arrows) in both scaffold conditions. Fibrin degradation (asterisks) is more apparent in rocking cultures. Scale bars = 500 µm for all images except Day 3 microgel-fibrin rocking condition (200 µm). OT: ovarian tissue.



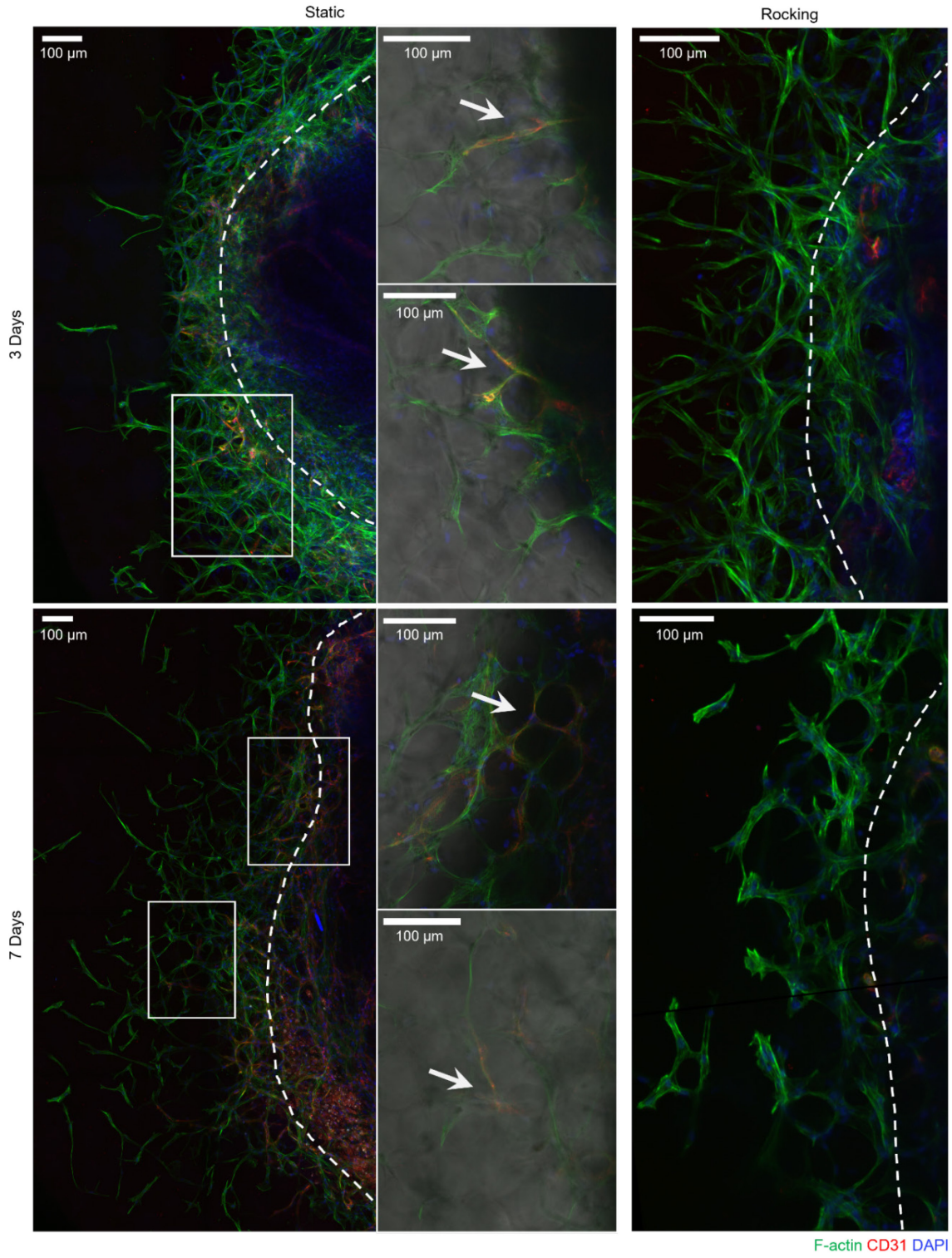
Appendix Figure E.2. Confocal images of human ovarian tissue encapsulated in fibrin-only gels and cultured under static or rocking conditions for 3 and 7 days. Samples were stained for F-actin and CD31 to assess overall and endothelial cell outgrowth. Due to limitations in staining consistency during these pilot studies, the low magnification images display F-actin and DAPI only. CD31 staining is shown for the inset in the Day 7 static condition. Dashed white lines delineate the edge of the ovarian tissue. Scale bars = 100 µm.



Appendix Figure E.3. Confocal images of human ovarian tissue encapsulated in microgel-fibrin composites and cultured under static or rocking conditions for 3 and 7 days. Samples were stained for F-actin and CD31. $CD31^{+}$ outgrowth wrapping around a microgel (arrow) was observed in the Day 3 static condition. Dashed white lines delineate the edge of the ovarian tissue. Scale bars = 100 µm



Appendix Figure E.4. Brightfield images of human ovarian tissue encapsulated heparin-functionalized microgel-fibrin composites and cultured under static or rocking conditions for 3 and 7 days. Cellular outgrowth from tissue fragments is visible at day 3 (white arrows) in both static and rocking conditions. Scale bars = 500 um. OT: ovarian tissue.



Appendix Figure E.5. Confocal images of human ovarian tissue encapsulated in heparin-functionalized microgel-fibrin composites and cultured under static or rocking conditions for 3 and 7 days. Samples were stained for F-actin and CD31. Static cultures demonstrate more consistent $CD31^{+}$ outgrowth compared to rocking conditions. High-magnification images for the Day 3 and Day 7 static conditions include the transmitted light channel (light gray) to better visualize microgel structure and $CD31^{+}$ staining (white arrows). Dashed white lines delineate the edge of the ovarian tissue. Scale bars = 100 µm

Bibliography

1. Siegel, R. L., Kratzer, T. B., Wagle, N. S., Sung, H. & Jemal, A. Cancer statistics, 2026. *CA Cancer J. Clin.* **76**, e70043 (2026).
2. Jefford, M., Nekhlyudov, L., Smith, A. L., Chan, R. J., Lai-Kwon, J. & Hart, N. H. Survivorship Care for People Affected by Advanced or Metastatic Cancer: Building on the Recent Multinational Association of Supportive Care in Cancer-ASCO Standards and Practice Recommendations. *American Society of Clinical Oncology Educational Book* **45**, e471752 (2025).
3. Filippi, F., Meazza, C., Paffoni, A., Raspagliesi, F., Terenziani, M. & Somigliana, E. Egg Freezing in Childhood and Young Adult Cancer Survivors. *Pediatrics* **138**, e20160291 (2016).
4. Cattoni, A., Parissone, F., Porcari, I., Molinari, S., Masera, N., Franchi, M., Cesaro, S., Gaudino, R., Passoni, P. & Balduzzi, A. Hormonal replacement therapy in adolescents and young women with chemo- or radio-induced premature ovarian insufficiency: Practical recommendations. *Blood Rev.* **45**, 100730 (2021).
5. Pollie, M. P., Martin, C. E., Rush, M. A., Carlson, C., Ricci, J., Trego, M., Mattei, P., Senapati, S., Ginsberg, J. P. & Gracia, C. R. Characterizing Patients Who Underwent Ovarian Tissue Cryopreservation at a Large Academic Center in the United States. *F. S. Rep.* https://doi.org/https://doi.org/10.1016/j.xfre.2025.09.006 (2025) doi:https://doi.org/10.1016/j.xfre.2025.09.006.
6. ESHRE, ASRM, CREWHIRL, IMS Guideline Group on POI, Panay, N., Anderson, R. A., Bennie, A., Cedars, M., Davies, M., Ee, C., Gravholt, C. H., Kalantaridou, S., Kallen, A., Kim, K. Q., Misrahi, M., Mousa, A., Nappi, R. E., Rocca, W. A., Ruan, X., Teede, H., Vermeulen, N., Vogt, E. & Vincent, A. J. Evidence-based guideline: Premature Ovarian Insufficiency. *Fertil. Steril.* **123**, 221–236 (2025).
7. Agarwal, S., Alzahrani, F. A. & Ahmed, A. Hormone Replacement Therapy: Would it be Possible to Replicate a Functional Ovary? *Int. J. Mol. Sci.* **19**, 3160 (2018).

8. Dolmans, M.-M. & Manavella, D. D. Recent advances in fertility preservation. *Journal of Obstetrics and Gynaecology Research* **45**, 266–279 (2019).
9. Mercier, A., Johnson, J. & Kallen, A. N. Prospective solutions to ovarian reserve damage during the ovarian tissue cryopreservation and transplantation procedure. *Fertil. Steril.* **122**, 565–573 (2024).
10. Fabbri, R., Vicenti, R., Magnani, V., Paradisi, R., Lima, M., De Meis, L., Rossi, S., Raimondo, D., Casadio, P., Venturoli, S., Maffi, M. & Seracchioli, R. Ovarian tissue cryopreservation and transplantation: 20 years experience in Bologna University. *Front. Endocrinol. (Lausanne).* **Volume 13-2022**, (2022).
11. Oktay, K. & Karlikaya, G. Ovarian Function after Transplantation of Frozen, Banked Autologous Ovarian Tissue. *New England Journal of Medicine* **342**, 1919–1919 (2000).
12. Khattak, H., Malhas, R., Craciunas, L., Afifi, Y., Amorim, C. A., Fishel, S., Silber, S., Gook, D., Demeestere, I., Bystrova, O., Lisyanskaya, A., Manikhas, G., Lotz, L., Dittrich, R., Colmorn, L. B., Macklon, K. T., Hjorth, I. M. D., Kristensen, S. G., Gallos, I. & Coomarasamy, A. Fresh and cryopreserved ovarian tissue transplantation for preserving reproductive and endocrine function: a systematic review and individual patient data meta-analysis. *Hum. Reprod. Update* **28**, 400–416 (2022).
13. Dolmans, M. M., von Wolff, M., Poirot, C., Diaz-Garcia, C., Cacciottola, L., Boissel, N., Liebenthron, J., Pellicer, A., Donnez, J. & Andersen, C. Y. Transplantation of cryopreserved ovarian tissue in a series of 285 women: a review of five leading European centers. *Fertil. Steril.* **115**, 1102–1115 (2021).
14. Pacheco, F. & Oktay, K. Current Success and Efficiency of Autologous Ovarian Transplantation: A Meta-Analysis. *Reproductive Sciences* **24**, 1111–1120 (2017).
15. Knuus, K., Nguyen, M., Hannula, M., Hassan, J., Otala, M., Tuuri, T., Lundin, K., Lahtinen, A., Damdimopoulou, P., Hyttinen, J. & Jahnukainen, K. Micro-CT and machine learning: a high-throughput alternative to histology for follicle reserve assessment in cryopreserved ovarian tissue. *J. Ovarian Res.* **19**, 15 (2025).
16. Baird, D. T., Webb, R., Campbell, B. K., Harkness, L. M. & Gosden, R. G. Long-Term Ovarian Function in Sheep after Ovariectomy and Transplantation of Autografts Stored at −196 C**This work was supported by Medical Research Council Program Grant 8929853. *Endocrinology* **140**, 462–471 (1999).

17. Nisolle, M., Casanas-Roux, F., Qu, J., Motta, P. & Donnez, J. Histologic and ultrastructural evaluation of fresh and frozen-thawed human ovarian xenografts in nude mice. *Fertil. Steril.* **74**, 122–129 (2000).
18. Van Eyck, A. S., Jordan, B. F., Gallez, B., Heilier, J. F., Van Langendonckt, A. & Donnez, J. Electron paramagnetic resonance as a tool to evaluate human ovarian tissue reoxygenation after xenografting. *Fertil. Steril.* **92**, 374–381 (2009).
19. Cacciottola, L., Manavella, D. D., Amorim, C. A., Donnez, J. & Dolmans, M. M. In vivo characterization of metabolic activity and oxidative stress in grafted human ovarian tissue using microdialysis. *Fertil. Steril.* **110**, 534-544.e3 (2018).
20. Donfack, N. J., Alves, K. A., Araújo, V. R., Cordova, A., Figueiredo, J. R., Smitz, J. & Rodrigues, A. P. R. Expectations and limitations of ovarian tissue transplantation. *Zygote* **25**, 391–403 (2017).
21. Cacciottola, L., Donnez, J. & Dolmans, M.-M. Ovarian tissue damage after grafting: systematic review of strategies to improve follicle outcomes. *Reprod. Biomed. Online* **43**, 351–369 (2021).
22. So, W., Dong, R., Lee, D., Abazarikia, A., Hackfort, B. T., Cupp, A. S. & Kim, S.-Y. Primordial Follicle Survival and Changes in Ovarian Vasculature May Be Independently Regulated During Chemotherapy. *Endocrinology* **166**, bqaf059 (2025).
23. Cowled, P. & Fitridge, R. Pathophysiology of Reperfusion Injury. in *Mechanisms of Vascular Disease: A Reference Book for Vascular Specialists* (eds. Fitridge, R. & Thompson, M.) 331–350 (The University of Adelaide, Barr Smith Press, Adelaide, 2011).
24. Gadek, L. M., Joswiak, C. & Laronda, M. M. Thawing fertility: a view of ovarian tissue cryopreservation processes and review of ovarian transplant research. *Fertil. Steril.* **122**, 574–585 (2024).
25. Sönmezer, M. & Özkavukcu, S. Chapter 14 - Surgical Approach to Orthotopic Ovarian Tissue Transplantation. in *Principles and Practice of Ovarian Tissue Cryopreservation and Transplantation* (ed. Oktay, K.) 143–156 (Elsevier, 2022). doi:https://doi.org/10.1016/B978-0-12-823344-3.00001-7.
26. Abir, R., Stav, D., Taieb, Y., Gabbay-Benziv, R., Kirshner, M., Ben-Haroush, A., Freud, E., Ash, S., Yaniv, I., Herman-Edelstein, M., Fisch, B. & Shufaro, Y. Novel extra cellular-

like matrices to improve human ovarian grafting. *J. Assist. Reprod. Genet.* **37**, 2105–2117 (2020).

27. Magen, R., Shufaro, Y., Daykan, Y., Oron, G., Tararashkina, E., Levenberg, S., Anuka, E., Ben-Haroush, A., Fisch, B. & Abir, R. Use of Simvastatin, Fibrin Clots, and Their Combination to Improve Human Ovarian Tissue Grafting for Fertility Restoration After Anti-Cancer Therapy. *Front. Oncol.* **10**, (2021).
28. Tanaka, A., Nakamura, H., Tabata, Y., Fujimori, Y., Kumasawa, K. & Kimura, T. Effect of sustained release of basic fibroblast growth factor using biodegradable gelatin hydrogels on frozen-thawed human ovarian tissue in a xenograft model. *Journal of Obstetrics and Gynaecology Research* **44**, 1947–1955 (2018).
29. Xia, Xi, Yin, Tailang, Yan, Jie, Yan, Liying, Jin, Chao, Lu, Cuilin, Wang, Tianren, Zhu, Xiaohui, Zhi, Xu, Wang, Jijun, Tian, Lei, Liu, Jing, Li, Rong & Qiao, Jie. Mesenchymal Stem Cells Enhance Angiogenesis and Follicle Survival in Human Cryopreserved Ovarian Cortex Transplantation. *Cell Transplant.* **24**, 1999–2010 (2015).
30. Cheng, J., Ruan, X., Li, Y., Du, J., Jin, F., Gu, M., Zhou, Q., Xu, X., Yang, Y., Wang, H. & Mueck, A. O. Effects of hypoxia-preconditioned HucMSCs on neovascularization and follicle survival in frozen/thawed human ovarian cortex transplanted to immunodeficient mice. *Stem Cell Res. Ther.* **13**, 474 (2022).
31. Manavella, D. D., Cacciottola, L., Pommé, S., Desmet, C. M., Jordan, B. F., Donnez, J., Amorim, C. A. & Dolmans, M. M. Two-step transplantation with adipose tissue-derived stem cells increases follicle survival by enhancing vascularization in xenografted frozen–thawed human ovarian tissue. *Human Reproduction* **33**, 1107–1116 (2018).
32. Manavella, D. D., Cacciottola, L., Payen, V. L., Amorim, C. A., Donnez, J. & Dolmans, M. M. Adipose tissue-derived stem cells boost vascularization in grafted ovarian tissue by growth factor secretion and differentiation into endothelial cell lineages. *Mol. Hum. Reprod.* **25**, 184–193 (2019).
33. Cacciottola, L., Nguyen, T. Y. T., Amorim, C. A., Donnez, J. & Dolmans, M.-M. Modulating hypoxia and oxidative stress in human xenografts using adipose tissue-derived stem cells. *F. S. Sci.* **2**, 141–152 (2021).
34. Cacciottola, L., Nguyen, T. Y. T., Chiti, M. C., Camboni, A., Amorim, C. A., Donnez, J. & Dolmans, M. M. Long-term advantages of ovarian reserve maintenance and follicle

development using adipose tissue-derived stem cells in ovarian tissue transplantation. *J. Clin. Med.* **9**, 1–18 (2020).

35. Man, L., Park, L., Bodine, R., Ginsberg, M., Zaninovic, N., Man, O. A., Schattman, G., Rosenwaks, Z. & James, D. Engineered endothelium provides angiogenic and paracrine stimulus to grafted human ovarian tissue. *Sci. Rep.* **7**, 8203 (2017).
36. Oktay, K., Marin, L., Bedoschi, G., Pacheco, F., Sugishita, Y., Kawahara, T., Taylan, E., Acosta, C. & Bang, H. Ovarian transplantation with robotic surgery and a neovascularizing human extracellular matrix scaffold: a case series in comparison to meta-analytic data. *Fertil. Steril.* **117**, 181–192 (2022).
37. Qazi, T. H. & Burdick, J. A. Granular hydrogels for endogenous tissue repair. *Biomaterials and Biosystems* **1**, 100008 (2021).
38. Griffin, D. R., Weaver, W. M., Scumpia, P. O., Di Carlo, D. & Segura, T. Accelerated wound healing by injectable microporous gel scaffolds assembled from annealed building blocks. *Nat. Mater.* **14**, 737–744 (2015).
39. Kedzierski, A., Kheirabadi, S., Jaberi, A., Ataie, Z., Mojazza, C. L., Williamson, M. L., Hjaltason, A. M., Risbud, A., Xiang, Y. & Sheikhi, A. Engineering the Hierarchical Porosity of Granular Hydrogel Scaffolds Using Porous Microgels to Improve Cell Recruitment and Tissue Integration. *Adv. Funct. Mater.* **35**, 2417704 (2025).
40. Ataie, Z., Horchler, S., Jaberi, A., Koduru, S. V, El-Mallah, J. C., Sun, M., Kheirabadi, S., Kedzierski, A., Risbud, A., Silva, A. R. A. E., Ravnic, D. J. & Sheikhi, A. Accelerating Patterned Vascularization Using Granular Hydrogel Scaffolds and Surgical Micropuncture. *Small* **20**, 2307928 (2024).
41. Pruett, L. J., Jenkins, C. H., Singh, N. S., Catallo, K. J. & Griffin, D. R. Heparin Microislands in Microporous Annealed Particle Scaffolds for Accelerated Diabetic Wound Healing. *Adv. Funct. Mater.* **31**, 2104337 (2021).
42. Anderson, A. R., Caston, E. L. P., Riley, L., Nguyen, L., Ntekoumes, D., Gerecht, S. & Segura, T. Engineering the Microstructure and Spatial Bioactivity of MAP Scaffolds Instructs Vasculogenesis In Vitro and Modifies Vessel Formation In Vivo. *Adv. Funct. Mater.* **35**, 2400567 (2025).
43. Folts, L., Martinez, A. S. & McKey, J. Tissue clearing and imaging approaches for in toto analysis of the reproductive system†. *Biol. Reprod.* **110**, 1041–1054 (2024).

44. Kinnear, H. M., Tomaszewski, C. E., Chang, A. L., Moravek, M. B., Xu, M., Padmanabhan, V. & Shikanov, A. The ovarian stroma as a new frontier. *Reproduction* **160**, R25–R39 (2020).
45. Jones, A. S. K., Hannum, D. F., Machlin, J. H., Tan, A., Ma, Q., Ulrich, N. D., Shen, Y., Ciarelli, M., Padmanabhan, V., Marsh, E. E., Hammoud, S., Li, J. Z. & Shikanov, A. Cellular atlas of the human ovary using morphologically guided spatial transcriptomics and single-cell sequencing. *Sci. Adv.* **10**, eadm7506 (2024).
46. Wu, M., Tang, W., Chen, Y., Xue, L., Dai, J., Li, Y., Zhu, X., Wu, C., Xiong, J., Zhang, J., Wu, T., Zhou, S., Chen, D., Sun, C., Yu, J., Li, H., Guo, Y., Huang, Y., Zhu, Q., Wei, S., Zhou, Z., Wu, M., Li, Y., Xiang, T., Qiao, H. & Wang, S. Spatiotemporal transcriptomic changes of human ovarian aging and the regulatory role of FOXP1. *Nat. Aging* **4**, 527–545 (2024).
47. Zhang, M., Guo, F., Zhang, Q., Hu, Q., Sun, D., Ma, Y., Li, Y., Guo, M., Ding, H., Guo, Y., Yang, B., Li, S., Sun, N., Zheng, Y. & Li, W. Spatial Transcriptomic Characteristics of the Aging Human Ovary. *Aging Cell* **25**, e70288 (2026).
48. Faire, M., Skillern, A., Arora, R., Nguyen, D. H., Wang, J., Chamberlain, C., German, M. S., Fung, J. C. & Laird, D. J. Follicle dynamics and global organization in the intact mouse ovary. *Dev. Biol.* **403**, 69–79 (2015).
49. Svingen, T., François, M., Wilhelm, D. & Koopman, P. Three-Dimensional Imaging of Prox1-EGFP Transgenic Mouse Gonads Reveals Divergent Modes of Lymphangiogenesis in the Testis and Ovary. *PLoS One* **7**, e52620- (2012).
50. Feng, Y., Cui, P., Lu, X., Hsueh, B., Möller Billig, F., Zarnescu Yanez, L., Tomer, R., Boerboom, D., Carmeliet, P., Deisseroth, K. & Hsueh, A. J. W. CLARITY reveals dynamics of ovarian follicular architecture and vasculature in three-dimensions. *Sci. Rep.* **7**, 44810 (2017).
51. Oren, R., Fellus-Alyagor, L., Addadi, Y., Bochner, F., Gutman, H., Blumenreich, S., Dafni, H., Dekel, N., Neeman, M. & Lazar, S. Whole Organ Blood and Lymphatic Vessels Imaging (WOBLI). *Sci. Rep.* **8**, 1412 (2018).
52. McKey, J., Cameron, L. A., Lewis, D., Batchvarov, I. S. & Capel, B. Combined iDISCO and CUBIC tissue clearing and lightsheet microscopy for in toto analysis of the adult mouse ovary†. *Biol. Reprod.* **102**, 1080–1089 (2020).

53. Xu, X., Mu, L., Li, L., Liang, J., Zhang, S., Jia, L., Yang, X., Dai, Y., Zhang, J., Wang, Y., Niu, S., Xia, G., Yang, Y., Zhang, Y., Cao, Y. & Zhang, H. Imaging and tracing the pattern of adult ovarian angiogenesis implies a strategy against female reproductive aging. *Sci. Adv.* **8**, eabi8683 (2026).
54. Mu, L., Wang, G., Yang, X., Liang, J., Tong, H., Li, L., Geng, K., Bo, Y., Hu, X., Yang, R., Xu, X., Zhang, Y. & Zhang, H. Physiological premature aging of ovarian blood vessels leads to decline in fertility in middle-aged mice. *Nat. Commun.* **16**, 72 (2025).
55. Kagami, K., Shinmyo, Y., Ono, M., Kawasaki, H. & Fujiwara, H. Three-dimensional evaluation of murine ovarian follicles using a modified CUBIC tissue clearing method. *Reproductive Biology and Endocrinology* **16**, 72 (2018).
56. Brunette, M. A., Kinnear, H. M., Hashim, P. H., Flanagan, C. L., Day, J. R., Cascalho, M., Padmanabhan, V. & Shikanov, A. Human Ovarian Follicles Xenografted in Immunoisolating Capsules Survive Long Term Implantation in Mice. *Front. Endocrinol. (Lausanne).* **Volume 13-2022**, (2022).
57. Ouni, E., Nedbal, V., Da Pian, M., Cao, H., Haas, K. T., Peaucelle, A., Van Kerk, O., Herinckx, G., Marbaix, E., Dolmans, M.-M., Tuuri, T., Otala, M., Amorim, C. A. & Vertommen, D. Proteome-wide and matrisome-specific atlas of the human ovary computes fertility biomarker candidates and open the way for precision oncofertility. *Matrix Biology* **109**, 91–120 (2022).
58. Gaylord, E. A., Foecke, M. H., Samuel, R. M., Soygur, B., Detweiler, A. M., McIntyre, T. I., Dorman, L. C., Borja, M., Laird, A. E., Arjyal, R., Du, J., Gardner, J. M., Neff, N., Fattahi, F. & Laird, D. J. Comparative analysis of human and mouse ovaries across age. *Science (1979).* **390**, eadx0659 (2026).
59. Harrison, A. S., Bjarkadottir, B. D., Kuscu, N., Davies, J., Lane, S. & Williams, S. A. Three-dimensional visualisation of human ovarian follicles using a whole-mount immunolabelling and optical tissue clearing method. *Reproduction and Fertility* **6**, e250096 (2025).
60. Fan, Y., Flanagan, C. L., Brunette, M. A., Jones, A. S., Baker, B. M., Silber, S. J. & Shikanov, A. Fresh and cryopreserved ovarian tissue from deceased young donors yields viable follicles. *F. S. Sci.* **2**, 248–258 (2021).

61. Brunette, M. A., Rionda, M. A., Sinko, D., Machlin, J. H., Blevins, G. M., Leo, M., Tan, A., Ray, B., Cascalho, M., Padmanabhan, V. & Shikanov, A. Restoration of ovarian endocrine function with encapsulated immune-isolated human ovarian xenograft in ovariectomized mice. *Sci. Adv.* **12**, eadx6348 (2026).
62. Matsumoto, K., Mitani, T. T., Horiguchi, S. A., Kaneshiro, J., Murakami, T. C., Mano, T., Fujishima, H., Konno, A., Watanabe, T. M., Hirai, H. & Ueda, H. R. Advanced CUBIC tissue clearing for whole-organ cell profiling. *Nat. Protoc.* **14**, 3506–3537 (2019).
63. Schindelin, J., Arganda-Carreras, I., Frise, E., Kaynig, V., Longair, M., Pietzsch, T., Preibisch, S., Rueden, C., Saalfeld, S., Schmid, B., Tinevez, J.-Y., White, D. J., Hartenstein, V., Eliceiri, K., Tomancak, P. & Cardona, A. Fiji: an open-source platform for biological-image analysis. *Nat. Methods* **9**, 676–682 (2012).
64. Machlin, J. H., Hannum, D. F., Jones, A. S. K., Schissel, T., Potocsky, K., Marsh, E. E., Hammoud, S., Padmanabhan, V., Li, J. Z. & Shikanov, A. Single-cell analysis comparing early-stage oocytes from fresh and slow-frozen/thawed human ovarian cortex reveals minimal impact of cryopreservation on the oocyte transcriptome. *Human Reproduction* **40**, 683–694 (2025).
65. Yano Maher, J. C., Zelinski, M. B., Oktay, K. H., Duncan, F. E., Segars, J. H., Lujan, M. E., Lou, H., Yun, B. H., Hanfling, S. N., Schwartz, L. E., Laronda, M. M., Halvorson, L. M., O'Neill, K. E. & Gomez-Lobo, V. Classification system of human ovarian follicle morphology: recommendations of the National Institute of Child Health and Human Development - sponsored ovarian nomenclature workshop. *Fertil. Steril.* **123**, 761–778 (2025).
66. Susaki, E. A., Tainaka, K., Perrin, D., Kishino, F., Tawara, T., Watanabe, T. M., Yokoyama, C., Onoe, H., Eguchi, M., Yamaguchi, S., Abe, T., Kiyonari, H., Shimizu, Y., Miyawaki, A., Yokota, H. & Ueda, H. R. Whole-Brain Imaging with Single-Cell Resolution Using Chemical Cocktails and Computational Analysis. *Cell* **157**, 726–739 (2014).
67. Cacciottola, L., Courtoy, G. E., Nguyen, T. Y. T., Hossay, C., Donnez, J. & Dolmans, M.-M. Adipose tissue–derived stem cells protect the primordial follicle pool from both direct follicle death and abnormal activation after ovarian tissue transplantation. *J. Assist. Reprod. Genet.* **38**, 151–161 (2021).

68. Riley, L., Schirmer, L. & Segura, T. Granular hydrogels: emergent properties of jammed hydrogel microparticles and their applications in tissue repair and regeneration. *Curr. Opin. Biotechnol.* **60**, 1–8 (2019).
69. Pruett, L., Koehn, H., Martz, T., Churnin, I., Ferrante, S., Salopek, L., Cottler, P., Griffin, D. R. & Daniero, J. J. Development of a microporous annealed particle hydrogel for long-term vocal fold augmentation. *Laryngoscope* **130**, 2432–2441 (2020).
70. Qazi, T. H., Wu, J., Muir, V. G., Weintraub, S., Gullbrand, S. E., Lee, D., Issadore, D. & Burdick, J. A. Anisotropic Rod-Shaped Particles Influence Injectable Granular Hydrogel Properties and Cell Invasion. *Advanced Materials* **34**, 2109194 (2022).
71. Wilson, K. L., Joseph, N. I., Onweller, L. A., Anderson, A. R., Darling, N. J., David-Bercholz, J. & Segura, T. SDF-1 Bound Heparin Nanoparticles Recruit Progenitor Cells for Their Differentiation and Promotion of Angiogenesis after Stroke. *Adv. Healthc. Mater.* **13**, 2302081 (2024).
72. Jaberi, A., Kedzierski, A., Kheirabadi, S., Tagay, Y., Ataie, Z., Zavari, S., Naghashnejad, M., Waldron, O., Adhikari, D., Lester, G., Gallagher, C., Borhan, A., Ravnic, D., Tabdanov, E. & Sheikhi, A. Engineering Microgel Packing to Tailor the Physical and Biological Properties of Gelatin Methacryloyl Granular Hydrogel Scaffolds. *Adv. Healthc. Mater.* **13**, 2402489 (2024).
73. Shen, A. Y., Rozen, W. M., Polyakov, A., Stern, K. & Rozen, G. Applying plastic surgery principles to ovarian tissue transplantation. *Gland Surg.* **10**, 2266–2274 (2021).
74. Dumont, C. M., Carlson, M. A., Munsell, M. K., Ciciriello, A. J., Strnadova, K., Park, J., Cummings, B. J., Anderson, A. J. & Shea, L. D. Aligned hydrogel tubes guide regeneration following spinal cord injury. *Acta Biomater.* **86**, 312–322 (2019).
75. de Rutte, J. M., Koh, J. & Di Carlo, D. Scalable High-Throughput Production of Modular Microgels for In Situ Assembly of Microporous Tissue Scaffolds. *Adv. Funct. Mater.* **29**, 1900071 (2019).
76. Qazi, T. H., Muir, V. G. & Burdick, J. A. Methods to Characterize Granular Hydrogel Rheological Properties, Porosity, and Cell Invasion. *ACS Biomater. Sci. Eng.* **8**, 1427–1442 (2022).
77. Riley, L., Wei, G., Bao, Y., Cheng, P., Wilson, K. L., Liu, Y., Gong, Y. & Segura, T. Void Volume Fraction of Granular Scaffolds. *Small* **19**, 2303466 (2023).

78. Lust, S. T., Hoogland, D., Norman, M. D. A., Kerins, C., Omar, J., Jowett, G. M., Yu, T. T. L., Yan, Z., Xu, J. Z., Marciano, D., da Silva, R. M. P., Dreiss, C. A., Lamata, P., Shipley, R. J. & Gentleman, E. Selectively Cross-Linked Tetra-PEG Hydrogels Provide Control over Mechanical Strength with Minimal Impact on Diffusivity. *ACS Biomater. Sci. Eng.* **7**, 4293–4304 (2021).
79. Merrill, E. W., Dennison, K. A. & Sung, C. Partitioning and diffusion of solutes in hydrogels of poly(ethylene oxide). *Biomaterials* **14**, 1117–1126 (1993).
80. Raeber, G. P., Lutolf, M. P. & Hubbell, J. A. Molecularly Engineered PEG Hydrogels: A Novel Model System for Proteolytically Mediated Cell Migration. *Biophys. J.* **89**, 1374–1388 (2005).
81. Callewaert, B., Gsell, W., Himmelreich, U. & Jones, E. A. V. Q-VAT: Quantitative Vascular Analysis Tool. *Front. Cardiovasc. Med.* **Volume 10-2023**, (2023).
82. Li, X., Chen, X. & Guo, H. Plasminogen activator inhibitor 1 is a novel predictor in human serum/follicular fluid for diminished ovarian reserve. *BMC Womens Health* **25**, 210 (2025).
83. Constantin, C., Matvienko, D., László, C., Scabia, V., Battista, L., Binz, P.-A., Bruce, S. J. & Brisken, C. Mimicking women's endocrine milieu in mice for women's health-related studies. *npj Women's Health* **3**, 13 (2025).
84. Van Eyck, A.-S., Bouzin, C., Feron, O., Romeu, L., Van Langendonckt, A., Donnez, J. & Dolmans, M.-M. Both host and graft vessels contribute to revascularization of xenografted human ovarian tissue in a murine model. *Fertil. Steril.* **93**, 1676–1685 (2010).
85. Lacroix, R., Sabatier, F., Mialhe, A., Basire, A., Pannell, R., Borghi, H., Robert, S., Lamy, E., Plawinski, L., Camoin-Jau, L., Gurewich, V., Angles-Cano, E. & Dignat-George, F. Activation of plasminogen into plasmin at the surface of endothelial microparticles: a mechanism that modulates angiogenic properties of endothelial progenitor cells in vitro. *Blood* **110**, 2432–2439 (2007).
86. Griffin, D. R., Archang, M. M., Kuan, C.-H., Weaver, W. M., Weinstein, J. S., Feng, A. C., Ruccia, A., Sideris, E., Ragkousis, V., Koh, J., Plikus, M. V, Di Carlo, D., Segura, T. & Scumpia, P. O. Activating an adaptive immune response from a hydrogel scaffold imparts regenerative wound healing. *Nat. Mater.* **20**, 560–569 (2021).

87. Liu, Y., Suarez-Arnedo, A., Shetty, S., Wu, Y., Schneider, M., Collier, J. H. & Segura, T. A Balance between Pro-Inflammatory and Pro-Reparative Macrophages is Observed in Regenerative D-MAPS. *Advanced Science* **10**, 2204882 (2023).
88. Liu, Y., Suarez-Arnedo, A., Riley, L., Miley, T., Xia, J. & Segura, T. Spatial Confinement Modulates Macrophage Response in Microporous Annealed Particle (MAP) Scaffolds. *Adv. Healthc. Mater.* **12**, 2300823 (2023).
89. Liu, Y., Suarez-Arnedo, A., Caston, E. L. P., Riley, L., Schneider, M. & Segura, T. Exploring the Role of Spatial Confinement in Immune Cell Recruitment and Regeneration of Skin Wounds. *Advanced Materials* **35**, 2304049 (2023).
90. Rodriguez Ayala, A., Christ, G. & Griffin, D. Cell-scale porosity minimizes foreign body reaction and promotes innervated myofiber formation after volumetric muscle loss. *NPJ Regen. Med.* **10**, 12 (2025).
91. Nicklow, E., Pruett, L. J., Singh, N., Daniero, J. J. & Griffin, D. R. Exploration of biomaterial-tissue integration in heterogeneous microporous annealed particle scaffolds in subcutaneous implants over 12 months. *Acta Biomater.* **196**, 183–197 (2025).
92. Campos-Junior, P. H. A., Alves, T. J. M., Dias, M. T., Assunçao, C. M., Munk, M., Mattos, M. S., Kraemer, L. R., Almeida, B. G., Russo, R. C., Barcelos, L., Camargo, L. S. A. & Viana, J. H. M. Ovarian Grafts 10 Days after Xenotransplantation: Folliculogenesis and Recovery of Viable Oocytes. *PLoS One* **11**, e0158109- (2016).
93. Wang, G., Zhang, S., Lu, H. & Mu, Y. Therapeutic Angiogenesis for Ovarian Transplantation through Ultrasound-Targeted Microbubble Destruction. *Ultrasound Med. Biol.* **47**, 1868–1880 (2021).
94. Vieira, A. R. S., Sousa, F. C. de, Barros, C. H. S. C., Santana, M. J., Alves, B. G. & Teixeira, D. Í. A. Color Doppler Ultrasonographic Examination of Ovarian Grafts in Goats. *Vet. Sci.* **11**, 580 (2024).
95. Isachenko, V., Mallmann, P., Petrunkina, A. M., Rahimi, G., Nawroth, F., Hancke, K., Felberbaum, R., Genze, F., Damjanoski, I. & Isachenko, E. Comparison of In Vitro- and Chorioallantoic Membrane (CAM)-Culture Systems for Cryopreserved Medulla-Contained Human Ovarian Tissue. *PLoS One* **7**, e32549- (2012).

96. Mueller, A., Lehner, J., Hancke, K., Janni, W. & Bundschu, K. Fertility preservation: improved neovascularization and follicle viability in cryopreserved bovine ovarian cortex transplants by remaining medulla tissue. *F. S. Sci.* **3**, 340–348 (2022).
97. Kristensen, S. G., Olesen, H. Ø., Zeuthen, M. C., Pors, S. E., Andersen, C. Y. & Mamsen, L. S. Revascularization of human ovarian grafts is equally efficient from both sides of the cortex tissue. *Reprod. Biomed. Online* **44**, 991–994 (2022).
98. Cheng, J., Gu, M., Ruan, X., Du, J., Jin, F. & Mueck, A. O. Revascularization of human ovarian grafts is not equally efficient from both sides of the ovarian cortex tissue. *Maturitas* **173**, 100 (2023).
99. Feng, Y., Li, Q., Wu, D., Niu, Y., Yang, C., Dong, L. & Wang, C. A macrophage-activating, injectable hydrogel to sequester endogenous growth factors for in situ angiogenesis. *Biomaterials* **134**, 128–142 (2017).
100. Pruett, L. J., Jenkins, C. H., Singh, N. S., Catallo, K. J. & Griffin, D. R. Heparin Microislands in Microporous Annealed Particle Scaffolds for Accelerated Diabetic Wound Healing. *Adv. Funct. Mater.* **31**, 2104337 (2021).
101. Tomaszewski, C. E., DiLillo, K. M., Baker, B. M., Arnold, K. B. & Shikanov, A. Sequestered cell-secreted extracellular matrix proteins improve murine folliculogenesis and oocyte maturation for fertility preservation. *Acta Biomater.* **132**, 313–324 (2021).
102. Jiang, Bin, Waller, Thomas M, Larson, Jeffery C, Appel, Alyssa A & Brey, Eric M. Fibrin-Loaded Porous Poly(Ethylene Glycol) Hydrogels as Scaffold Materials for Vascularized Tissue Formation. *Tissue Eng. Part A* **19**, 224–234 (2013).
103. Deng, Z., Tovani, C. B., Bianco, S., Comandini, G., Elghajiji, A., Aleemardani, M., Moscalu, R., Zappia, J., Fernandes, B., Annett, O., Hammond, C. L., Wong, J., Adams, D. J., Scarpa, F., Whitehouse, M. R., Seddon, A. M. & Armstrong, J. P. K. Coagulative Granular Hydrogels with an Enzyme Catalyzed Fibrin Network for Endogenous Tissue Regeneration. *Adv. Healthc. Mater.* **n/a**, e04146 (2025).
104. Chen, S., Han, X., Cao, Y., Yi, W., Zhu, Y., Ding, X., Li, K., Shen, J., Cui, W. & Bai, D. Spatiotemporalized Hydrogel Microspheres Promote Vascularized Osteogenesis via Ultrasound Oxygen Delivery. *Adv. Funct. Mater.* **34**, 2308205 (2024).

105. Guan, Y., Niu, H., Liu, Z., Dang, Y., Shen, J., Zayed, M., Ma, L. & Guan, J. Sustained oxygenation accelerates diabetic wound healing by promoting epithelialization and angiogenesis and decreasing inflammation. *Sci. Adv.* **7**, eabj0153 (2025).
106. Phelps, E. A., Landázuri, N., Thulé, P. M., Taylor, W. R. & García, A. J. Bioartificial matrices for therapeutic vascularization. *Proceedings of the National Academy of Sciences* **107**, 3323–3328 (2010).
107. Sun, G., Shen, Y.-I., Kusuma, S., Fox-Talbot, K., Steenbergen, C. J. & Gerecht, S. Functional neovascularization of biodegradable dextran hydrogels with multiple angiogenic growth factors. *Biomaterials* **32**, 95–106 (2011).
108. Donnez, J., Dolmans, M. M., Demylle, D., Jadoul, P., Pirard, C., Squifflet, J., Martinez-Madrid, B. & Van Langendonckt, A. Livebirth after orthotopic transplantation of cryopreserved ovarian tissue. *The Lancet* **364**, 1405–1410 (2004).
109. Demeestere, I., Simon, P., Buxant, F., Robin, V., Fernandez, S. A., Centner, J., Delbaere, A. & Englert, Y. Ovarian function and spontaneous pregnancy after combined heterotopic and orthotopic cryopreserved ovarian tissue transplantation in a patient previously treated with bone marrow transplantation: Case Report. *Human Reproduction* **21**, 2010–2014 (2006).
110. Roux, C., Amiot, C., Agnani, G., Aubard, Y., Rohrlich, P.-S. & Piver, P. Live birth after ovarian tissue autograft in a patient with sickle cell disease treated by allogeneic bone marrow transplantation. *Fertil. Steril.* **93**, 2413.e15-2413.e19 (2010).
111. Revelli, A., Marchino, G., Dolfin, E., Molinari, E., Delle Piane, L., Salvagno, F. & Benedetto, C. Live birth after orthotopic grafting of autologous cryopreserved ovarian tissue and spontaneous conception in Italy. *Fertil. Steril.* **99**, 227–230 (2013).
112. Chu, Y., Zhang, J., Wang, L., Xie, J., Chen, J., Hu, X., Zhou, J., Mao, R., Yan, M. & Yue, J. The mechanism and protective strategies of follicle injury after ovarian tissue cryopreservation and thawed transplantation: a review. *J. Ovarian Res.* **18**, 217 (2025).
113. Roness, H. & Meirow, D. FERTILITY PRESERVATION: Follicle reserve loss in ovarian tissue transplantation. *Reproduction* **158**, F35–F44 (2019).
114. Widener, A. E., Roberts, A. & Phelps, E. A. Granular Hydrogels for Harnessing the Immune Response. *Adv. Healthc. Mater.* **13**, 2303005 (2024).

115. Machlin, J. H., Potocsky, K., Kruger, R. E., Spence, J., Padmanabhan, V. & Shikanov, A. Dynamics of YAP localization and transcript activity in human oocytes and granulosa cells across early-stage folliculogenesis: an exploratory investigation. *J. Assist. Reprod. Genet.* **42**, 4221–4236 (2025).